Design, Optimization, and Applications of Few-Cycle Ti:Sapphire Lasers

by

Li-Jin Chen

B.S., Electrical Engineering, National Taiwan University, 2003
M.S., Electro-Optical Engineering, National Taiwan University, 2005

Submitted to the Department of Electrical Engineering and Computer Science
in partial fulfillment of the requirements for the degree of

Doctor of Philosophy in Electrical Engineering

at the

MASSACHUSETTS INSTITUTE OF TECHNOLOGY

February 2012

Author.....
Department of Electrical Engineering and Computer Science
December 2 , 2011

Certified by.....
Franz X. Kärtner
Professor of Electrical Engineering
Thesis Supervisor

Accepted by.....
Leslie A. Kolodziejski
Professor of Electrical Engineering
Chairman, Department Committee on Graduate Theses

THIS PAGE IS INTENTIONALLY LEFT BLANK

Design, Optimization, and Applications of Few-Cycle Ti:Sapphire Lasers

by

Li-Jin Chen

Submitted to the Department of Electrical Engineering and Computer Science
on December 1, 2012,
in partial fulfillment of the requirements for the degree of
Doctor of Philosophy in Electrical Engineering and Computer Science

Abstract

Ti:Sapphire mode-locked lasers are a unique technology that enables a wide variety of applications. Owing to the ultrabroadband nature of the Ti:sapphire crystal and the invention of precisely engineered dispersion-compensating mirrors (DCMs), these lasers are now capable of generating stable pulse trains directly with octave-spanning spectrum, few-cycle pulse duration, and a desired repetition rate from a compact system. This paves the way to a new world of emerging applications ranging from the search of exoplanets, high-harmonic generation, to precision measurement.

Qualitatively, the key to the stable mode-locking of Ti:Sapphire lasers lies in the balance of various spatial and temporal nonlinear effects such as self-amplitude modulation(SAM), self-phase modulation(SPM), saturable absorption, self-focusing, gain-filtering, gain-guiding, and so on. However, since much shorter pulses and much higher intracavity intensities are often reached inside the laser gain medium, the spatiotemporal dynamics in such lasers are even more complicated as non-negligible multi-photon processes also come into play. Due to the strong coupling between these effects, performing a reliable analysis and optimization become extremely challenging.

In this thesis we study the spatiotemporal dynamics of pulse evolution in the few-cycle regime and provide guidelines for designing and optimizing these lasers for repetition rate ranging from 85 MHz to 2 GHz. The essential background reviews as well as key concepts in KLM lasers will be given together with a demonstration of octave-spanning Ti:sapphire lasers with record-high repetition rate. A numerical model for simulating the full spatiotemporal dynamics is introduced. For an efficient numerical calculation, GPU accelerated computing techniques are adopted. With this model, many unique features that are observed from the experiments can be simulated for the first time. A novel type of output coupler called gain-matched output coupler is introduced which can greatly reduce the nonlinearity required for ultra-broadband mode-locking. Already at pump power levels close to the cw lasing threshold it is possible to initiate robust mode-locking and generate <8 fs output pulses from Ti:sapphire lasers with excellent beam quality operating in the center of its stability range. Moreover, the development of visible astro-combs based on few-cycle Ti:sapphire lasers will be discussed. This application is enabled by two promising technologies (broadband zero-GDD mirror sets and Cherenkov radiation in the few-cycle regime) which are developed to increase the repetition rate and

spectral coverage of the laser systems operated in the few-cycle regime. Fiber-optic Cherenkov radiation in the few-cycle regime excited by sub-10fs Ti:sapphire pulses is studied. Through a dispersion-engineered PCF driven by a few-cycle pulse, the nonlinearity can produce highly efficient broadband frequency up-conversion to the visible wavelength range. Finally, we propose and demonstrate a new approach for broadband dispersion-free optical cavities using a zero-GDD mirror set; With the first zero-GDD mirror pair, the construction of a ~40 GHz filtering cavity with 100 nm bandwidth for a green astro-comb (480-580 nm) was demonstrated. Finally, the thesis is concluded by discussing the practical issues related to the construction of a easy-to-operate, long-term stable few-cycle Ti:sapphire laser.

Thesis Supervisor: Franz X. Kärtner

Title: Professor of Electrical Engineering and Computer Science

Acknowledgements

First of all, I would like to thank my advisor Prof. Franz Kärtner for the guidance and support during my PhD life. He is a great mentor, friend, and research supervisor. He not only gives me a lot of freedom in research but also loves to share his deep physical insight as well as life experience with us, which makes my entire PhD life joyful. I also would like to thank Prof. Erich Ippen and Prof. Leslie Kolodziejski who continuously give me valuable comments over the past few years since the OAWG project (the first research project I was working on at MIT) to my thesis defense.

Working at MIT is nothing but a great fun. As an international student who has to travel to the other end of the Earth and start a whole new life in a foreign country, I feel so lucky to have the company of all OQE group members for these years. Everyone is always friendly and helpful whenever I was bothered by any problem in my research or daily life. I especially thank Dr. Andrew Benedick for leading me into the field of few-cycle Ti:sapphire lasers. It is my great pleasure to work with such a creative and diligent man who always takes a positive attitude when facing challenges. I thank Dr. Jonathan Birge for passing his precious knowledge in coating design to me. I thank Dr. Guoqing Chang for being such a wonderful colleague and friend for these years. I enjoy having all kinds of discussion with Dr. Chang that simply makes my time in lab really enjoyable. I also thank the astro-comb team at Harvard University for giving me the opportunity to participate one of the coolest projects that the astronomers are working on. I also want to thank all members in Republic of China (Taiwan) student association and

especially those in our OQE group (Tsung-Han Tsai, Chien-Jen Lai, Hsiang-Chieh Lee, Hung-Wen Chen, Shu-Wei Huang, and Jonathan Liu). Even if I am standing on the other end of the Earth, this place feels like home to me with their company. I wish them best luck for their future research and life.

Finally and most importantly, I wish to express my highest personal gratitude to my wife Huei-Yuan Hsiao, my parents Chen-Chin Chen and Yen-Fong Kao, and my elder brother Jia-Fu Chen. They always give me the greatest support for everything I want to do and ask for no return. Without their love and care, I could not finish my PhD and this thesis. This thesis is dedicated to them.

Curriculum Vitae

Education

MIT, Ph.D. in Electrical Engineering and Computer Science, Feb 2012

National Taiwan University, M.S. in Electro-Optical Engineering, June 2005

National Taiwan University, B.S. in Electrical Engineering, June 2003

Patents

1. C.-K. Sun, ***L.-J. Chen***, H.-W. Chen, "Plastic Waveguide for Terahertz Wave," US Patent 7,409,132.
2. F. X. Kärtner, ***L.-J. Chen***, "Mode-locking with reduced nonlinearity using gain-matching output couplers", MIT Case NO. 14156; US patent pending.
3. F. X. Kärtner, ***L.-J. Chen***, G. Q. Chang "Broadband Dispersion-Free Optical Filter Cavities Based on Dielectric Mirrors with Complementary Dispersion", MIT Case NO. 14229; US patent pending.

Refereed Journal Publications

1. ***L.-J. Chen***, C.-J. Lai, and F. X. Kärtner, "Spatiotemporal model for few-cycle Ti:sapphire lasers," Manuscript in preparation.
2. S.-W. Huang, G. Cirmi, J. Moses, K.-H. Hong, S. Bhardwaj, J. R. Birge, ***L.-J. Chen***, E. Li, B. Eggleton, G. Cerullo, and F. X. Kärtner, "Scalable High-Energy Sub-Cycle Waveform Synthesis for Strong-Field Physics," Nature Photonics 5, 475–479, 2011.
3. G. Q. Chang, ***L.-J. Chen***, and F. X. Kärtner, "Fiber-Optic Cherenkov radiation in the Few-Cycle Regime," Opt. Express 19, 6635-6647, 2011.
4. ***L.-J. Chen***, G. Q. Chang, J. R. Birge, and F. X. Kärtner, "High-Finesse Dispersion-Free Cavities for Broadband Filtration of Laser Comb Lines," Opt. Express 18, 23204-23211, 2010.
5. ***L.-J. Chen***, M. Y. Sander, F. X. Kärtner, "Kerr-lens Mode-locking with Minimum Nonlinearity Using Gain-Matching Output Couplers", Opt. Lett. 35, 2916-2918, 2010.
6. G. Q. Chang, ***L.-J. Chen***, and F. X. Kärtner, "Highly Efficient Cherenkov Radiation in Photonic Crystal Fibers for Broadband Visible Wavelength Generation," Opt. Lett. 35(14), 2361-2363, 2010.
7. H.–W. Chen, T. Sosnowski, C.–H. Liu, ***L.-J. Chen***, J. Birge, A. Galvanauskas, F. X. Kärtner, and G. Q. Chang, "Chirally-coupled-core Yb-fiber laser delivering 80-fs pulses with diffraction-limited beam quality warranted by a high-dispersion-mirror based compressor," Opt. Express 18, 24699, 2010.
8. C.–H. Li, A. Glenday, A. Benedick, G. Q. Chang, ***L.-J. Chen***, C. Cramer, P. Fendel, G. Furesz, F. X. Kärtner, S. Korzennik, D. F. Phillips, D. Sasselov, A. Szentgyorgyi, R. L. Walsworth, "In-situ determination of astro-comb calibration lines to better than 10 cm/s," Opt. Express 18, 13239-13249, 2010.
9. A. J. Benedick, G. Q. Chang, J. R. Birge, ***L.-J. Chen***, A. Glenday, C. H. Li, D. F. Phillips, A. Szentgyorgyi, S. Korzennik, G. Furesz, R. L. Walsworth, and F. X. Kärtner, "Visible wavelength astro-comb," Opt. Express 18, 19175-19184, 2010.

10. E. L. Falcão-Filho, C.-J. Lai, K.-H. Hong, V.-M. Gkortsas, S.-W. Huang, ***L.-J. Chen***, and Franz X. Kärtner, "Scaling of high-order harmonic efficiencies with visible wavelength drivers: a route to efficient EUV sources," Appl. Phys. Lett. 97, 061107, 2010
11. ***L.-J. Chen***, A. J. Benedick, J. R. Birge, M. Y. Sander, and F. X. Kärtner, "Octave-spanning, dual-output 2.166 GHz Ti:sapphire laser," Opt. Express 16, 20699-20705, 2008.
12. H.-W. Chen, Y.-T. Li, J.-L. Kuo, J.-Y. Lu, ***L.-J. Chen***, C.-L. Pan, and C.-K. Sun, "Investigation on Spectral Loss Characteristics of Subwavelength THz Fibers," Opt. Lett 32(9), 1017-1019, 2007.
13. ***L.-J. Chen***, H.-W. Chen, T.-F. Kao, J.-Y. Lu, and C.-K. Sun, "Low-loss Subwavelength Plastic Fiber for Terahertz Waveguiding," Opt. Lett. 31(3), 308-310, 2006.
14. ***L.-J. Chen***, T.-F. Kao, J.-Y. Lu, and C.-K. Sun, "A Simple Terahertz Spectrometer Based on a Low-Reflectivity Fabry-Perot Interferometer Using Fourier Transform Spectroscopy," Opt. Express 14, 3840-3846, 2006.
15. J.-Y. Lu, ***L.-J. Chen***, C.-K. Sun and et. al., "Terahertz microchip for illicit drug detection," IEEE Photon. Technol. Lett. 18(21), 2254-2256, 2006.
16. T.-F. Kao, H.-H. Chang, ***L.-J. Chen***, J.-Y. Lu, A.-S. Liu, Y.-C. Yu, R.-B. Wu, W.-S. Liu, J.-I. Chyi, and C.-K. Sun, "Frequency Tunability of Terahertz Photonic Transmitters," Appl. Phys. Lett. 88, 093501, 2006.
17. J.-Y. Lu, H.-H. Chang, ***L.-J. Chen***, M.-C. Tien, and C.-K. Sun, "Optoelectronic-Based High-Efficiency Quasi-CW Terahertz Imaging," IEEE Photon. Technol. Lett. 17(11), 2406-2408, 2005.
18. M.-C. Tien, H.-H. Chang, J.-Y. Lu, ***L.-J. Chen***, S.-Y. Chen, R.-B. Wu, W.-S. Liu, J.-I. Chyi, and C.-K. Sun, "Device Saturation Behavior of Submillimeter-wave Membrane Photonic Transmitters," IEEE Photon. Technol. Lett. 16(3), 873-875, 2004.
19. S.-P. Tai, M.-C. Chan, T.-H. Tsai, S.-H. Guol, ***L.-J. Chen***, and C.-K. Sun, "Two-photon Fluorescence Microscope with a Hollow-core Photonic Crystal Fiber," Opt. Express 12(25), 6122-6128, 2004.

Refereed Conference Proceedings (*) Invited

1. (*) ***L.-J. Chen***, G. Q. Chang, and F. X. Kärtner, "Highly efficient, broadband Cherenkov radiation in photonic crystal fibers," paper CTuT3, CLEO/QELS, San Jose, CA, USA, 2010.
2. ***L.-J. Chen***, C.-J. Lai, and F. X. Kärtner, "The Role of Plasma Formation in Mode-locking of Few-cycle Ti:sapphire Lasers: A Spatiotemporal Model," paper CWR5, CLEO: Science & Innovations, Baltimore, 2011.
3. ***L.-J. Chen***, C.-J. Lai, and F. X. Kärtner, "Spatiotemporal Model of Passively Mode-locked Few-cycle Ti:sapphire Lasers: The Role of Plasma Formation," paper HThC3, High-Intensity Lasers and High-Field Phenomena (HILAS), Istanbul, Turkey, 2011
4. ***L.-J. Chen***, G. Q. Chang, C.–H. Li, A. G. Glenday, A. J. Benedick, D. F. Phillips, R. L. Walsworth, and F. X. Kärtner, "High-finesse dispersion-free cavities for broadband filtration of laser comb lines," paper TuF1, 17th international conference on Ultrafast Phenomena, Snowmass village, CO, USA; Ultrafast Phenomena XVII, Oxford University Press, 2010.

5. ***L.-J. Chen***, M. Y. Sander, and F. X. Kärtner, "Mode-locking with minimum nonlinearity using inverse-gain output couplers," paper CThI7, CLEO/QELS, San Jose, 2010
6. ***L.-J. Chen***, G. Q. Chang, J. R. Birge, and F. X. Kärtner, "Complementary chirped-mirror pair for broadband dispersion-free cavities," paper FB5, Optical Interference Coatings, Tucson, AZ, USA, 2010.
7. ***L.-J. Chen***, A. J. Benedick, J. R. Birge, M. Y. Sander, F. X. Kartner, "2GHz octave-spanning Ti:sapphire Laser with non-intrusive carrier-envelope phase stabilization", paper WZ1, IEEE Lasers and Electro-Optics Society (LEOS), Newport Beach, CA, USA, 2008.
8. ***L.-J. Chen***, H.-W. Chen, T.-F. Kao, J.-Y. Lu, and C.-K. Sun, "Low-loss Subwavelength THz Plastic Fibers," paper CMS1, CLEO/QELS, Long Beach, CA, USA, 2006.
9. ***L.-J. Chen***, T.-F. Kao, H.-H. Chang, J.-Y. Lu, and C.-K. Sun, "Terahertz Fourier Transform Spectrometer Based on a Low-Reflectivity Fabry-Perot Interferometer," paper QTuI2, CLEO/QELS, Baltimore, MD, USA, 2005.
10. (*) M. Y. Sander, ***L.-J. Chen***, and F. X. Kärtner, "Spatial and Temporal Modeling of Few-Cycle Ti:Sapphire Lasers", URSI GASS 2011, Istanbul, Turkey.
11. (*) G. Q. Chang, ***L.-J. Chen***, and F. X. Kärtner, "Fiber-optic Cherenkov radiation excited by few-cycle pulses," paper 7937-57, SPIE Photonics West, San Francisco, CA, USA. 2011.
12. (*) Chi-Kunag Sun, ***L.-J. Chen***, H.-W. Chen, and J.-Y. Lu, "Subwavelength Plastic Fiber for Terahertz Wave Guiding," Optics East/ Conference on Terahertz Physics, Devices, and Systems, Boston, MA, paper 6373-12; Proceedings of SPIE 6373, 63730F, 2006.
13. (*) J.-Y. Lu, H.-W. Chen, ***L.-J. Chen***, and C.-K. Sun, "Sub-Wavelength THz Plastic Fibers," in Proceeding of Terahertz and Gigahertz Electronics and Photonics VI, Photonics West, paper 6472-7, San Jose, CA, USA; Proceedings of SPIE 6472, 647208, 2007.
14. (*) E. P. Ippen, A. J. Benedick, J. R. Birge, H. Byun, ***L.-J. Chen***, G. Q. Chang, D. Chao, J. Morse, A. Motamedi, M. Sander, G. Petrich, L. Kolodziejski, and F. Kärtner, "Optical arbitrary waveform generation," paper JThC4, CLEO/QELS, San Jose, 2010
15. (*) C.-H. Li, A. J. Benedick, C. E. Cramer, G. Q. Chang, ***L.-J. Chen***, P. Fendel, G. Furesz, A. G. Glenday, F. X. Kärtner, D. F. Phillips, D. Sasselov, A. Szentgyorgy, R. L. Walsworth, "Laser frequency combs for precision astrophysical spectroscopy," paper EG4.3, CLEO Europe/EQEC, Munich, Germany, 2009.
16. (*) C.-H. Li, A. J. Benedick, C. E. Cramer, G. Q. Chang, ***L.-J. Chen***, P. Fendel, G. Furesz, A. G. Glenday, F. X. Kärtner, D. F. Phillips, D. Sasselov, A. Szentgyorgyi, and R. L. Walsworth, "Femtosecond Laser Frequency Comb for Precision Astrophysical Spectroscopy," paper CMII1, CLEO/QELS, San Jose, CA, USA, 2009.
17. G. Q. Chang, ***L.-J. Chen***, and F. X. Kärtner, "Fiber-Optic Cherenkov radiation in the Few-Cycle Regime", paper CWR2, CLEO: Science & Innovations, Baltimore, 2011.
18. J.-Y. Lu, ***L.-J. Chen***, T.-F. Kao, H.-H. Chang, C.-K. Sun, A.-S. Liu, Y.-C. Yu, R.-B. Wu, W.-S. Liu, and J.-I. Chyi, "Terahertz Biochip for Illicit Drug Detection," paper CMLL7, CLEO/QELS, Long Beach, CA, USA, 2006.

19. J.-Y. Lu, ***L.-J. Chen***, T.-F. Kao, H.-H. Chang, A.-S. Liu, Y.-C. Yu, R.-B. Wu, W.-S. Liu, J.-I. Chyi, C.-L. Pan, M.-C. Tsai, and C.-K. Sun, "THz Biochip Based on Optoelectronic Devices," Optics East/Sensors and Photonics for Applications in Industry, Life Sciences, and Communications, Boston, MA, USA, Optoelectronic Devices: Physics, Fabrication, and Application II, paper 6013-19; Proceedings of SPIE 6013, pp. 60130I-1 – 60130I-8, 2005.
20. T.-F. Kao, ***L.-J. Chen***, H.-H. Chang, J.-Y. Lu, A.-S. Liu, Y.-C. Yu, R.-B. Wu, W.-S. Liu, J.-I. Chyi, and C.-K. Sun, "Broadband-response and Frequency-tunable Terahertz Photonic Transmitters with High Efficiency," paper CTuBB6, CLEO/QELS, Baltimore, MD, USA, 2005.
21. C.-H. Li, G. Q. Chang, ***L.-J. Chen***, D. F. Phillps, F. X. Kärtner, R. L. Walsworth "Lab Demonstration and Characterization of a Green Astro-comb" paper AME5, Advanced Solid-State Photonics (ASSP), Istanbul, Turkey, 2011.
22. H.-W. Chen, J.-Y. Lu, ***L.-J. Chen***, Po-Jui Chiang, Hung-Chun Chang, Yu-Tai Lu, Ci-Ling Pan, and C.-K. Sun, "THz Directional Fiber Coupler," paper CThLL7, CLEO/QELS, Baltimore, MD, USA, 2007.
23. H.-W. Chen, J.-Y. Lu, ***L.-J. Chen***, Y.-T. Lu, C.-L. Pan, and C.-K. Sun, "Spectral Loss Characteristics of Subwavelength THz Fibers," paper CJWA107, CLEO/QELS, Baltimore, MD, USA, 2007.
24. J.-Y. Lu, H.-H. Chang, ***L.-J. Chen***, M.-C. Tien, and C.-K. Sun, "Terahertz-Wave Molecular Imaging Based on a Compact High-Efficiency Photonic Transmitter," The 3rd Annual Meeting of the Society for Molecular Imaging, St. Louis, MO, USA, 2004.
25. J.-Y. Lu, H.-H. Chang, ***L.-J. Chen***, M.-C. Tien, and C.-K. Sun, "Quasi-CW THz-Imaging Based on a High-Efficiency Tunable Photonic Transmitter," paper CMG1, CLEO/QELS, San Francisco, CA, USA, 2004.
26. H.–W. Chen, T. Sosnowski, C.–H. Liu, L.–J Chen, J. R. Birge, A. Galvanauskas, F. X. Kärtner, and G. Q. Chang, "High-energy chirally-coupled-core Yb-fiber laser with high dispersion mirror compressor to achieve 1W-level, sub-100fs pulses with diffraction-limited beam quality," paper ATuC5, Advanced Solid-State Photonics (ASSP), Istanbul, Turkey, 2011.
27. S.-W. Huang, G. Cirmi, K.-H. Hong, J. Moses, J. R. Birge, S. Bhardwaj, V.-M. Gkortsas, A. J. Benedick, ***L.-J. Chen***, E. Li, B. Eggleton, G. Cerullo, and F. X. Kärtner, "Scalable High-Energy Sub-Cycle Waveform Synthesis for Strong-Field Physics," paper JWC4, Advanced Solid-State Photonics (ASSP), Istanbul, Turkey, 2011.
28. G. Q. Chang, H. –W. Chen, T. Sosnowski, C. –H. Liu, L.–J Chen, J. Birge, A. Galvanauskas, and F. Kärtner, "High-energy chirally-coupled-core Yb-fiber oscillator with high-dispersion-mirror compressor: generation of ~1W, 80-fs pulses with diffraction-limited beam quality," Post-deadline paper PDPC3, OSA annual meeting, Rochester, USA, 2010.
29. C.-H. Li, D. F. Phillips, A. G. Glenday, A. J. Benedick, G. Chang, ***L.-J. Chen***, C. Cramer, G. Furesz, F. X. Kärtner, D. Sasselov, A. Szentgyorgyi and R. L. Walsworth, "Astro-comb calibration of an Echelle Spectrograph", Proc. SPIE 7735, 773540 (2010)
30. A. Szentgyorgyi, A. J. Benedick, G. Q. Chang, H.-W. Chen, ***L.-J. Chen***, G. Furesz, A. Glenday, F. X. Kärtner, S. Korzennik, C.-H. Li, D. Phillips, R. L. Walsworth "Progress Toward Laser Calibration of Ultra-Precise Radial Velocity

Measurements," Conf. on Astronomy of Exoplanets with Precise Radial Velocities, Penn State University, University Park, PA, USA, 2010.

31. A. J. Benedick, G. Q. Chang, H.-W. Chen, ***L.-J. Chen***, G. Furesz, A. Glenday, F. X. Kärtner, S. Korzennik, C.-H. Li, A. Szentgyorgyi, D. Phillips, R. Walsworth, "Astro-comb calibration of the TRES spectrograph at visible wavelengths," Conf. on Astronomy of Exoplanets with Precise Radial Velocities, Penn State University, University Park, PA, USA, 2010.
32. S.-W. Huang, G. Cirmi, J. Moses, K.-H. Hong, A. J. Benedick, ***L.-J. Chen***, E. Li, B. Eggleton, G. Cerullo, and F. X. Kärtner, "Ultrabroadband Optical Parametric Chirped Pulse Amplifier System for Single-Cycle Waveform Synthesis," paper CWA4, CLEO/QELS, San Jose, CA, USA, 2010.
33. E. L. Falcão-Filho, C.-J. Lai, V.-M. Gkortsas, S.-W. Huang, ***L.-J. Chen***, K.-H. Hong, and Franz X. Kärtner, "Scaling of high-order harmonic efficiencies with visible 400-nm and 800-nm driver pulses," paper JThI4, CLEO/QELS, San Jose, 2010.
34. C.-H Li, A. G. Glenday, D. F. Phillips, S. Korzennik, G. Q. Chang, A. Benedick, ***L.-J. Chen***, F. X. Kärtner, D. Sasselov, A. Szentgyorgy, R. Walsworth, "Laboratory demonstration of a green astro-comb," E1. 00049, 41st Annual meeting of the APS division of atomic, molecular and optical physics, Houston, TX, USA, 2010
35. D. F. Phillips, A. G. Glenday, C.-H. Li, C. Cramer, S. Korzennik, G. Q. Chang, ***L.-J. Chen***, A. Benedick, F. X. Kärtner, D. Sasselov, A. Szentgyorgy, R. L. Walsworth, "Calibration of an astrophysical spectrograph with an astro-comb," E1. 00050, 41st Annual meeting of the APS division of atomic, molecular and optical physics, Houston, TX, USA, 2010
36. S.-P. Tai, M.-C. Chan, T.-H. Tsai, S.-H. Guol, ***L.-J. Chen***, and C.-K. Sun, "Two-Photon Fluorescence Microscope with a Hollow Core Photonic Crystal Fiber," Photonics West, paper 5691-19, San Jose, CA, USA; Proceedings of SPIE 5691, 146-153, 2005.
37. C.-K. Sun, M.-C. Tien, H.-H. Chang, J.-Y. Lu, ***L.-J. Chen***, S.-Y. Chen, R.-B. Wu, W.-S. Liu, and J.-I. Chyi, "Conversion Efficiency and Device Behavior of Edge-coupled Membrane Photonic Transmitters," paper TuR4, IEEE Laser and Electro-Optical Society (LEOS), Tucson, AZ, USA, 2003.

THIS PAGE IS INTENTIONALLY LEFT BLANK

Contents

List of Figures

THIS PAGE INTENTIONALLY LEFT BLANK

Chapter 1

Introduction

1.1. Background

Over the past few decades, the advances in ultrafast laser technology have led to a remarkable success in generating few-cycle pulses directly from a laser. First of all, using gain materials capable of emitting very broadband light such as Ti:sapphire and other Chromium-doped crystals has opened the door to few-cycle lasers. However, due to the non-uniform gain and loss profile, laser oscillation normally occurs for just one or a few resonator modes where the saturated gain is close to the loss curve. In order to obtain a short pulse, additional mechanisms must be placed in the laser to overcome the gain filtering effect and maintain the phase coherence of a large number of lasing modes. Such process has been termed *mode locking* whose main goal is to create an environment that favors pulsed operation over continuous-wave operation. Since the mid-1960s, various active [1–6] and passive mode locking [7–13] techniques have been intensively studied. The results have successfully pushed the shortest pulse duration from the sub-nanosecond to sub-picosecond regime. For the two following decades, the world of ultrafast was defined by dye lasers with colliding-pulse mode-locking (CPM) [14], [15] in the

~100fs regime. To date, the dye lasers have been replaced by Ti:sapphire laser and the Kerr-lens mode-locking (KLM) technique [16]. Since the Kerr-nonlinearity provides almost instantaneous response to the pulse intensity, it sets no limit to the shortest pulse that can be generated even with the broadest bandwidth material – Ti:sapphire. Since the first demonstration of the KLM-Ti:sapphire laser in 1991, researchers spent more than one decade to fully explore the power of the Ti:sapphire laser. Nowadays, Ti:sapphire laser has become a commercially available tool for routine generation of sub-two-cycle or even octave-spanning pulses at various repetition rates up to GHz range.

The key to the stable mode-locking of Ti:Sapphire lasers lies in the balance of various spatial and temporal nonlinear effects such as self-amplitude modulation (SAM), self-phase modulation (SPM), saturable absorption, self-focusing, gain-filtering, gain-guiding, and so on. Due to the strong coupling between these effects, performing a reliable analysis and optimization become extremely challenging. Over the past few decades, various spatial or temporal theories have been developed for explaining the physics behind the operation of KLM lasers from different point of view. For example, through the introduction of an intensity dependent lens in the ABCD analysis of the laser cavity, the SAM action can be derived from the spatial variation of the beam width inside the gain crystal (for soft-aperture KLM cavity) or at the plane of a slit (for hard-aperture KLM cavity). In the time and frequency domain picture, the mode-locking dynamics can be explained using the concept of dispersion-managed soliton [17]. Due to the balance of SPM and cavity group delay dispersion (GDD), the pulse does not change its

shape after each round-trip and generate a stable output pulse. These mode-locking dynamics are linked by the optical Kerr effect which leads to self-focusing effect in space and SPM in the time domain. These nonlinear effects are more dramatic in few-cycle lasers due to much higher intracavity pulse intensity. As a result, the spatiotemporal dynamics become more complicated and the physics behind many phenomena in the few-cycle lasers has not been unveiled such as the highly structured beam profile across the entire wavelength range. Currently, the optimization of few-cycle lasers is still relying mostly on the experimental observations. To further improve these few-cycle lasers, a more accurate theory that can deal with the full spatiotemporal mode-locking dynamics of the laser should be employed.

Comparing to the lasers generating longer pulses, few-cycle lasers are more desirable for applications demanding higher intensity and shorter pulse duration. When the pulse duration is down to sub-two-cycle regime, manipulating the shape of the electric field by the carrier-envelope phase control is an important technique in electric-field sensitive applications. The broadband optical spectrum from a few-cycle laser can be used for broadband spectroscopy [18–20] or excitation of multiple fluorescence proteins [21]. For a few-cycle laser with octave-spanning spectrum, it can also be turned into frequency combs when the laser repetition rate and carrier-envelope offset frequency are both stabilized. The most common approach used for detecting carrier-envelope offset frequency is 1f-2f interferometry. This approach needs two successive nonlinear processes including either an intracavity or extracavity spectral broadening for obtaining 1f and 2f

components and the self-referencing involving second-harmonic-generation for producing a carrier-envelope (CE) beat note. The laser repetition rate is usually detected with a photodetector and controlled by changing the cavity length. These stabilization processes turn a laser into an optical flywheel that can transfer the frequency stability from a microwave source to the optical frequencies and provide unparallel fractional frequency stability. Frequency combs are also versatile tools for stable and accurate measurements in frequency metrology, time resolved and frequency-domain spectroscopy [22], optical arbitrary waveform generation (OAWG) [23] and calibration of astronomical spectrographs [24]. To enable more compact and more powerful frequency comb systems, ultra-broadband laser oscillators operating at high repetition rates are highly desired. For frequency metrology and spectroscopy, higher repetition rates correspond to larger mode spacing, higher power per mode, and higher signal-to-noise ratio. In OAWG applications, high repetition rate enables the use of lower resolution spectral dispersers. The well-defined comb lines from a high-repetition-rate frequency comb also serves as an excellent frequency ruler for calibrating an astrophysical spectrograph. By mapping the CCD pixels with the laser comb lines with known frequencies, radial velocity measurements with unprecedented precision ~ 1 cm/s may be achieved. This will enable the determination of the mass of sub-Earth-mass exoplanets by the Doppler shift resulting from the reflex motion of the parent star around the common center of gravity. The Doppler shift sensitivity enabled by the blue astro-comb will make it possible to determine the properties of a broad spectrum of exoplanet systems including their geology as well as the detailed

properties of the stars they orbit. Such astronomical optical spectroscopy (also known as astro-comb [24]) is an essential tool for addressing two of the leading questions in science today: the existence and distribution of life throughout the universe and the dynamics and nature of dark energy. A crucial enabling technology for these investigations is an ultrastable, broadband, high line-density, bright wavelength calibrator that can be deployed flexibly and reliably at ground based observatories. The technology to build such a calibrator can be realized by integrating an octave-spanning mode-locked femtosecond laser with a Fabry-Perot filtering cavity, which produces a set of bright, regularly-spaced emission features in frequency domain. To realize such an exciting application for exploring earth-like planet, the development of broadband filtering cavity and a high-repetition rate frequency comb based on high-performance, easy-to-operate, and long-term stable few-cycle lasers are necessary.

1.2. Overview of the Thesis

This thesis is organized as follows: In chapter 2, the essential background reviews as well as key concepts in KLM lasers will be given. The design guideline as well as the main challenges for practical ultrabroadband Ti:sapphire laser will be discussed. Finally, an octave-spanning Ti:sapphire laser with the world's highest repetition rate will be demonstrated. In chapter 3, a numerical model for simulating the full spatiotemporal dynamics is introduced. The NLSE dominating the nonlinear propagation process of the pulse in the few-cycle regime is derived. To enable efficient numerical calculation, GPU accelerated computing techniques are adopted. With this model, many unique features that are observed from the

experiments can be simulated for the first time. In chapter 4, a novel type of output coupler called gain-matched output coupler is introduced. The gain-matched output coupler can greatly reduce the nonlinearity required for ultra-broadband mode-locking. Already at pump power levels close to the cw lasing threshold it is possible to initiate robust mode-locking and generate <8 fs output pulses from Ti:sapphire lasers with excellent beam quality operating in the center of its stability range. In chapter 5, we study the fiber-optic Cherenkov radiation in the few-cycle regime excited by sub-10fs Ti:sapphire pulses. Through a dispersion-enginnered PCF and a few-cycle pulse, the nonlinearity can produce highly efficient broadband frequency up-conversion to the visible wavelength range. The technique has enabled the constructions of visible astro-combs. In chapter 6 we have proposed and demonstrated a new approach for broadband dispersion-free optical cavities using a zero-GDD mirror set; e.g., to enable laser frequency combs for pulse repetition-rate multiplication and pulse enhancement. With a first zero-GDD mirror pair design, the construction of a ~40 GHz filtering cavity with 100 nm bandwidth for a green astro-comb (480-580 nm) was demonstrated. By proper structure scaling and re-optmization, the spectral coverage of the zero-GDD mirror set can be easily shifted to other wavelengths. We believe this technique can also enable many other frequency-comb-based applications that demand large comb spacing or high peak intensity. Finally, the thesis is concluded by discussing the practical issues related to the construction of a easy-to-operate, long-term stable few-cycle Ti:sapphire laser. Possible routes for further improvements will be suggested.

Chapter 2

Ultrabroadband Ti:Sapphire Lasers

2.1. Introduction

This chapter provides the essential background reviews as well as key concepts in KLM lasers. We also discuss design guidelines and main challenges for an practical ultra-broadband Ti:sapphire laser. As an example, we demonstrate an octave-spanning Ti:sapphire laser with the highest repetition-rate.

2.2. Brief Review of the Laser Basics

LASER, an acronym originally for the process of **L**ight **A**mplification by **S**timulated **E**mission of **R**adiation, is now generally used to represent the light with high degree of spatial and temporal coherence or the device that emits such type of light. Unlike the natural processes such as incandescence (hot body radiation) and luminescence (cold body radiation) that radiate incoherent light, laser only allows the emission of photons from a finite number of resonant modes predefined by the laser cavity. As a result, the laser light exhibits predictable and controllable behavior that can be used to sense, characterize, or even change the properties of materials in its path. This property makes laser a powerful tool for both scientific

and industrial purposes. This section is devoted to a brief review of laser properties as well as presenting the convention used throughout the thesis.

2.2.1. Plane Wave: The General Solution of the Helmholtz Equation

Since lasers emit electromagnetic waves, it is appropriate to start from the well-known Helmholtz wave equation derived from the Maxwell's equations (assuming the medium is nonmagnetic, i.e. $\mu=\mu_0$)

$$\nabla^2\mathbf{E} = \mu_0\varepsilon\frac{\partial^2}{\partial t^2}\mathbf{E} \tag{2.1}$$

The general solution of the equation is a linearly-polarized plane wave propagating along one direction (e.g. z-axis),

$$\mathbf{E}(z,t) = E_0\cos(\omega t - kz + \phi)\hat{\mathbf{n}}, \tag{2.2}$$

where $\hat{\mathbf{n}}$ is a unit vector in the transverse plane whose orientation is the polarization of the wave, ω the angular frequency, and k the propagation constant satisfying the dispersion relation

$$k^2 = \omega^2\mu_0\varepsilon = n^2\omega^2\mu_0\varepsilon_0 = \frac{n^2\omega^2}{c^2}, \tag{2.3}$$

where n is the refractive index of the material and c is the speed of light. In the form of a monochromatic wave, solution (2.2) can be used to compose the light field radiated from an ideal laser. To take the advantage of Fourier analysis, it is usually rewritten using a complex notation

$$\mathbf{E}(z,t) \equiv \hat{\mathbf{n}}\cdot\mathrm{Re}\left[E(z,t)\right] = \hat{\mathbf{n}}\cdot\mathrm{Re}\left[\tilde{E}_0 e^{j(\omega t-kz)}\right] \tag{2.4}$$

where the phase ϕ has been incorporated into the complex scalar $\tilde{E}_0$ and the frequency-domain representation of the complex field can be calculated by Fourier transform defined as:

$$\hat{E}(z,\omega) \equiv \frac{1}{2\pi}\int_{-\infty}^{\infty} E(z,t)e^{-j\omega t}dt \tag{2.5}$$

In this notation, the laser beam intensity *I*, i.e. the magnitude of time-averaged Poynting vector, can be computed as:

$$I = \frac{1}{2}\varepsilon_0 cn\left|\tilde{E}_0\right|^2 \tag{2.6}$$

The results can be extended to circularly and elliptically polarized waves as they are the superposition of two orthogonal linearly-polarized waves in the transverse plane.

2.2.2. Paraxial Approximation and Gaussian Beams

In the cases considered here, the beams are paraxial. In the simplest case where only a monochromatic beam with a finite transverse extent is used, the optical field can be conveniently represented as a superposition of plane waves with an angular frequency ω and a propagation vector close to the direction of energy flow defined as z-axis. Mathematically, it is then useful to write a general solution in the form of

$$E(x,y,z,t) = E_0 u(x,y,z)e^{j(\omega t - kz)} \tag{2.7}$$

The solution $u(x,y,z)$ must obey the Helmholtz wave equation (2.1), resulting in the well known paraxial wave equation (PWE)

$$\nabla_T^2 u - 2jk\frac{\partial u}{\partial z} = 0 \tag{2.8}$$

where ∇_T^2 is the transverse Laplacian and $u(x,y,z)$ is assumed to be slowly varying along the z-axis. The PWE has Gaussian beam solutions. The fundamental Gaussian beam u_{00} is written as

$$u_{00}(x, y, z) \sim e^{-(x^2+y^2)/w^2(z)} e^{-jk(x^2+y^2)/2R(z)} e^{j\phi(z)} \tag{2.9}$$

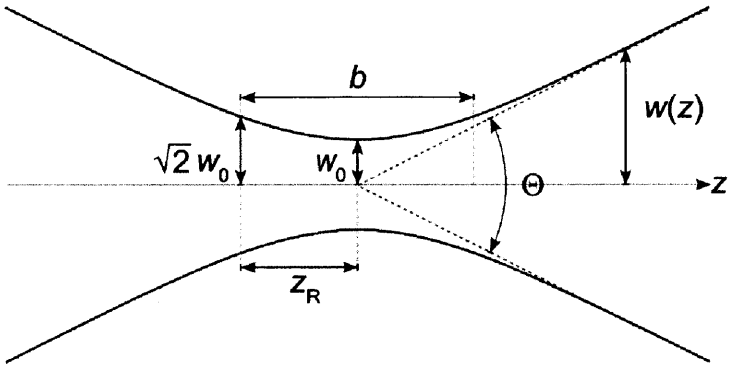

Figure 2.1 Diagram of a fundamental Gaussian beam.

The important parameters of a Gaussian beam can be summarized as follows (see Figure 2.1):

$$w_0 = \sqrt{\frac{z_R \lambda}{n\pi}} \tag{2.10}$$

$$w(z) = w_0 \sqrt{1 + \left(\frac{z}{z_R}\right)^2} \tag{2.11}$$

$$\frac{1}{R(z)} = \frac{z}{z^2 + z_R^2} \tag{2.12}$$

$$\phi(z) = \tan^{-1} \frac{z}{z_R} \tag{2.13}$$

where λ is the wavelength of the light, z the relative position along the propagation axis, $2z_R$ the confocal parameter (known as depth of focus) defining the region where the beam radius $w(z)$ is less than $\sqrt{2}$ times of the beam waist radius w_0, $R(z)$ the radius of curvature of the phase front, and $\phi(z)$ the Gouy phase shift. These features are related to a complex beam parameter q given by

$$q = z + jz_R . \tag{2.14}$$

In Gaussian beam propagation, the q parameter is very useful for describing the beam evolution through an optical system composed of lenses, mirrors, tilted plates and even a laser cavity formed by a number of optical components. The effect of an optical system on a Gaussian beam can be determined by a bilinear transformation of q using the ABCD matrix approaches:

$$q_{out} = \frac{Aq_{in} + B}{Cq_{in} + D} \tag{2.15}$$

The generalized ABCD matrices describing propagation, refraction, and reflection of Gaussian beams are shown in Table 2.1.

Element	Sagittal M^S	Tangential M^T
Propagation in a medium with constant n $M_A(d)$	$\begin{pmatrix} 1 & d \\ 0 & 1 \end{pmatrix}$	

Refraction at a curved interface $M_B(\theta_i, n_r, R)$	$\begin{pmatrix} 1 & 0 \\ \dfrac{\cos\theta_i - \sqrt{n_r^2 - \sin^2\theta_i}}{R \cdot n_r} & 1/n_r \end{pmatrix}$	$\begin{pmatrix} \dfrac{\sqrt{n_r^2 - \sin^2\theta_i}}{n_r \cos\theta_i} & 0 \\ \dfrac{\cos\theta_i - \sqrt{n_r^2 - \sin^2\theta_i}}{R \cdot \cos\theta_i \sqrt{n_r^2 - \sin^2\theta_i}} & \dfrac{\cos\theta_i}{\sqrt{n_r^2 - \sin^2\theta_i}} \end{pmatrix}$
Reflection at a curved interface $M_C(\theta_I, R)$	$\begin{pmatrix} 1 & 0 \\ -2/R\cos\theta_i & 1 \end{pmatrix}$	$\begin{pmatrix} 1 & 0 \\ -2\cos\theta_i/R & 1 \end{pmatrix}$

Table 2.1 Generalized ABCD matrices for propagation, refraction, and reflection. R is the radius of curvature of the interface, θ_i is the angle of incidence, n_r is the refractive index ratio of the output medium to input medium.

For most optics used in common linear optical systems such as lenses, mirrors, optical windows, and prisms, we can find their ABCD matrix using a combination of these three matrices. For example, the ABCD matrices of a Brewster window of thickness t in the tangential and sagittal plane are given by

$$\mathbf{M}_{\mathbf{BP,T}} = \begin{pmatrix} \dfrac{\sqrt{n_r^2 - \sin^2\theta_{B,21}}}{n_r \cos\theta_{B,21}} & 0 \\ 0 & \dfrac{\cos\theta_{B,21}}{\sqrt{n_r^2 - \sin^2\theta_{B,21}}} \end{pmatrix} \begin{pmatrix} 1 & d \\ 0 & 1 \end{pmatrix} \begin{pmatrix} \dfrac{\sqrt{n_r^2 - \sin^2\theta_{B,12}}}{n_r \cos\theta_{B,12}} & 0 \\ 0 & \dfrac{\cos\theta_{B,12}}{\sqrt{n_r^2 - \sin^2\theta_{B,12}}} \end{pmatrix} \tag{2.16}$$

$$\mathbf{M}_{\mathbf{BP,S}} = \begin{pmatrix} 1 & 0 \\ 0 & n_r \end{pmatrix} \begin{pmatrix} 1 & d \\ 0 & 1 \end{pmatrix} \begin{pmatrix} 1 & 0 \\ 0 & 1/n_r \end{pmatrix} \tag{2.17}$$

where n_r is the refractive index ratio of the plate to free space and d is the path length. $\theta_{B,12}$ and $\theta_{B,21}$ are the Brewster angles in the free space and the plate.

$$\theta_{B,12} = \tan^{-1}(n_r) \tag{2.18}$$

$$\theta_{B,21} = \tan^{-1}(1/n_r) \tag{2.19}$$

$$d = \frac{t}{\cos\theta_{B,12}} \tag{2.20}$$

2.2.3. Optical Resonators

Self-consistent q-parameter

To solve the resonant modes supported by a laser cavity, one can calculate the overall ABCD matrix by multiplying the matrix of each individual component in one round-trip. The ABCD matrix is calculated from an arbitrary plane of interest (i.e. reference plane). For a stable mode, the field must reproduce itself after every round-trip, i.e.

$$q = \frac{Aq + B}{Cq + D} \tag{2.21}$$

With the fact that $AD - BC = 1$, the self-consistent q parameter is then given by

$$q = \frac{A - D}{2C} + j\frac{1}{|C|}\sqrt{1 - \left(\frac{A + D}{2}\right)^2} \tag{2.22}$$

The stability condition is obtained by requiring that q must have nonzero imaginary part, i.e.

$$-2 \le (A + D) \le 2 \tag{2.23}$$

Longitudinal Modes

Once the q parameter on a reference plane is found, the structure and the round-trip Gouy phase shift of the resonator mode across the entire cavity can be obtained. The round-trip Gouy phase is required to analyze the frequency of the longitudinal

modes using the resonance condition given by (assuming the resonator is made of ideal mirrors that introduce no phase change in reflection)

$$\frac{2\pi f_p}{c} L_{eff} + \Delta\phi_{Gouy} = 2p\pi \tag{2.24}$$

$$L_{eff}(f_p) = \int_0^L n(z, f_p) z dz \tag{2.25}$$

where f_p is the frequency of the p-th longitudinal mode. L_{eff} denotes the effective cavity length assuming the light is propagating in vacuum, which is calculated from L (the real round-trip length of the cavity) and n (the refractive index of the medium along the axis of propagation z). After rearranging (2.24), we can find

$$f_p = \frac{c}{L_{eff}}(p - \frac{\Delta\phi_{Gouy}}{2\pi}) \tag{2.26}$$

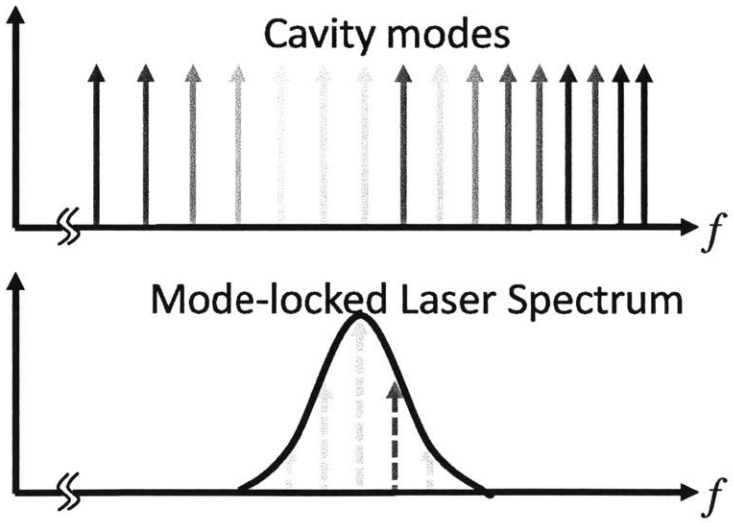

Figure 2.2 Longitudinal modes (fundamental) of a laser cavity without dispersion compensation. Only a narrow bandwidth can be used to support mode-locking.

For a stable pulse train generated from a mode-locked laser, its spectrum consists of many equally-spaced spectral lines. However, it should be noted that L_{eff}

is not constant since practical laser cavities are always filled with dispersive media. As a result, the frequency spacing between adjacent modes changes across the wavelength. For the wavelength range covered by typical few-cycle Ti:sapphire lasers (600 – 1100nm), L_{eff} becomes larger for shorter wavelengths if intracavity dispersion compensating component is absent, leading to a more dense mode spacing as shown in Figure 2.2. In such a dispersive cavity, the change in frequency spacing is only negligible within a very narrow bandwidth, which limits the pulse duration of the laser. In few-cycle laser mode-locking, the dispersion due to intracavity materials needs to be compensated to create equally-spaced longitudinal modes over the entire gain bandwidth of the laser crystal, as shown in Figure 2.3. However, it was very challenging to precisely control the high-order cavity dispersion until the invention of double-chirped mirror (DCM) pairs. In section 2.3, the recent progress and design guidelines for DCMs will be discussed.

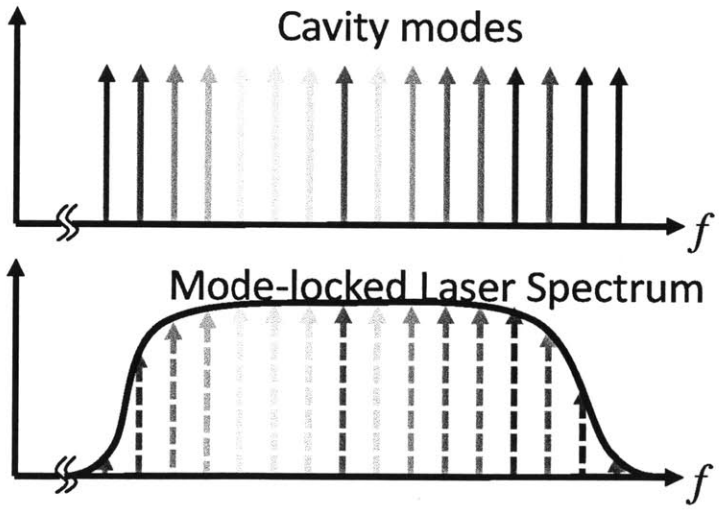

Figure 2.3 Longitudinal modes (fundamental) of an ideal laser cavity without dispersion. The ultrabroadband mode-locked laser can be supported in this case.

Transverse modes

Although the fundamental Gaussian beam is the most important spatial mode in ultrafast lasers, the existence of higher-order transverse modes cannot be ignored for understanding the solid-state mode-locking dynamics in the few-cycle regime. As discussed in many papers [25], [26], mode-locking of ultra-broadband lasers is usually accompanied by a wavelength-dependent beam profile. Fortunately, these highly structured modes can be decomposed into a superposition of Gaussian modes from a complete orthogonal basis set such as Hermite-Gaussian and Laguerre-Gaussian modes. Hermite-Gaussians are often chosen to describe laser mode from an optical system that is not radially symmetric but rather has a distinction between vertical (sagittal) and horizontal (tangential) axes. In KLM Ti:sapphire laser cavities, the q-parameter in the two axes might not be identical due to the presence of tilted curved mirrors and Brewster plates. The resulting high-order transverse modes are calculated by treating the two axes separately, as shown in (2.27) and (2.28).

$$u_{mn}(x,y,z) = u_m(x,z)u_n(y,z) \tag{2.27}$$

$$\begin{cases} u_m(x,z) \sim \dfrac{1}{\sqrt{w_x(z)}} H_m\left(\dfrac{\sqrt{2}x}{w_x(z)}\right) e^{-\frac{x^2}{w_x^2(z)}} e^{-j\frac{kx^2}{2R_x(z)}} e^{j(m+\frac{1}{2})\phi_x(z)} \\ u_n(y,z) \sim \dfrac{1}{\sqrt{w_y(z)}} H_m\left(\dfrac{\sqrt{2}y}{w_y(z)}\right) e^{-\frac{y^2}{w_y^2(z)}} e^{-j\frac{ky^2}{2R_y(z)}} e^{j(n+\frac{1}{2})\phi_y(z)} \end{cases} \tag{2.28}$$

$H_\upsilon(\xi)$ are Hermite polynomials with a nonnegative integer index [27]. The corresponding frequency of the high-order transverse mode is calculated by replacing the term $\Delta\phi_{Gouy}$ in (2.26) with [28]

$$\Delta\phi_{Gouy}(m,n) = m\Delta\phi_x + n\Delta\phi_y + \frac{\Delta\phi_x + \Delta\phi_y}{2} \tag{2.29}$$

The last term in (2.29) is the total Gouy phase change in one round-trip for the fundamental mode. Typically, the fundamental mode sees more gain than the higher-order modes since it overlaps better with the pump laser. As a result, the laser will have a stronger tendency to mode-lock in the fundamental mode. The excitation of high-order modes is usually observed in the KLM Ti:sapphire lasers operated in the few-cycle regime. The reason is that the beam is always tightly focused inside the crystal with a strong Kerr-nonlinearity which induces coupling between longitudinal and transverse modes. For the wavelengths where the crystal provides nearly no gain (e.g. above 1100 and below 600nm), these excited high-order modes could dominate the beam profile depending on the cavity loss and overall dispersion. More details will be discussed in Chapter 3.

When performing spatiotemporal simulations, we often assume that the cavity is radially symmetric in order to speed up the simulation even though this is not always justified in reality. In this case, using Laguerre-Gaussians as the basic set is preferred. The mode field with a radial index p and azimuthal index l is given by

$$u_{pl}(r,\phi,z) \sim \frac{1}{w(z)}\left(\frac{\sqrt{2}r}{w(z)}\right)^{|l|} L_p^{|l|}\left(\frac{2r^2}{w^2(z)}\right) e^{-\frac{r^2}{w^2(z)}} e^{-j\frac{kr^2}{2R(z)}} e^{j(2p+|l|+1)\phi(z)} \tag{2.30}$$

where $L_p^{|l|}$ are the generalized Laguerre polynomials. The corresponding frequency is then given by

$$\Delta\phi_{Gouy}(p,l) = (2p + |l| + 1)\Delta\phi \tag{2.31}$$

Linear Cavity vs. Ring Cavity

There are two main types of cavity configurations for solid-state lasers: ring cavities and linear cavities. The schematics of a ring cavity and a linear cavity are shown in Figure 2.5 and Figure 2.4, respectively.

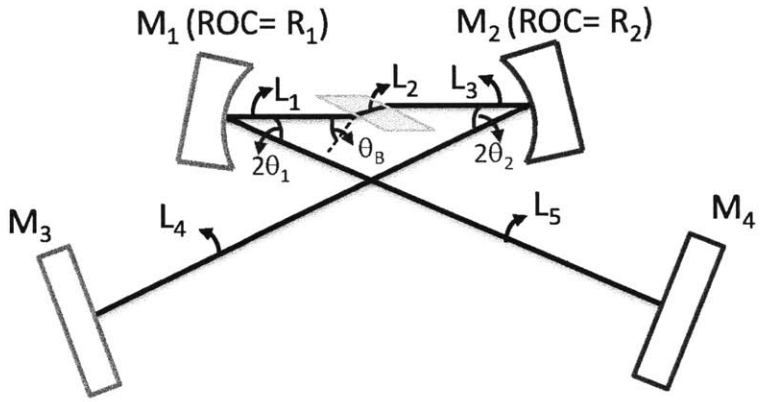

Figure 2.4 Schematic of the typical linear resonator used for KLM lasers.

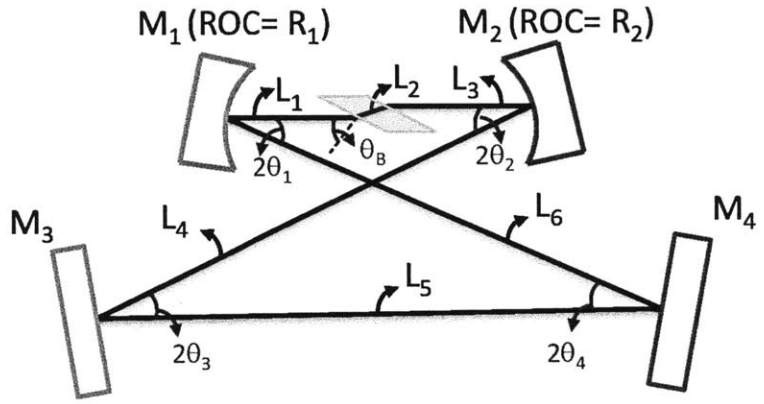

Figure 2.5 Schematic of the typical ring resonator used for KLM lasers.

The main difference between the two setups is that the circulating beam hits every component once in the ring cavity but twice in the linear cavity (except for

the end mirrors) per round-trip. Therefore, the cavity round-trip time of a linear cavity will be roughly twice longer compared to a ring cavity with similar footprint. As a result, ring cavities are often chosen in high-repetition-rate lasers. During the cavity alignment, there are many practical issues related to the maximization of mode-locking strength. As an example, in order to minimize the surface-reflection loss, the gain crystal needs to be placed at Brewster's angle, which might lead to astigmatism between sagittal and tangential planes. In order to compensate for astigmatism, two curved mirrors must be tilted at some angle. Another important issue in optimizing KLM mode-locked lasers is to place the beam focus at the correct position inside the crystal. The issue has been intensively studied for both cavities. In most cases the analysis was performed with an unfolded equivalent system approach (see Figure 2.7 and Figure 2.6) and the cavity astigmatism was compensated by tilting the curved mirror by [29], [30]:

$$\theta_a = \pi - \cos^{-1}\left(\frac{l_B^{\,2}}{Rn^3}\left[n^2 - 1 - \sqrt{n^4 - 2n^2 + 1 + \frac{R^2 n^6}{l_B^{\,2}}}\right]\right) \tag{2.32}$$

where l_B is the path length inside the Brewster plate and R is the radius of curvature of the curved mirror. In the simplest way, one can choose an identical angle on both curved mirrors M_1 and M_2 and use each one to compensate for half of the path length ($\theta_1 = \theta_2 = \theta_a/2$ with $l_B = L_2/2$). However, it should be noted that using an identical angle is not always necessary. Sometimes, one might need to use different angles to break the cavity symmetry in order to avoid bi-directional mode-locking in the ring cavity laser.

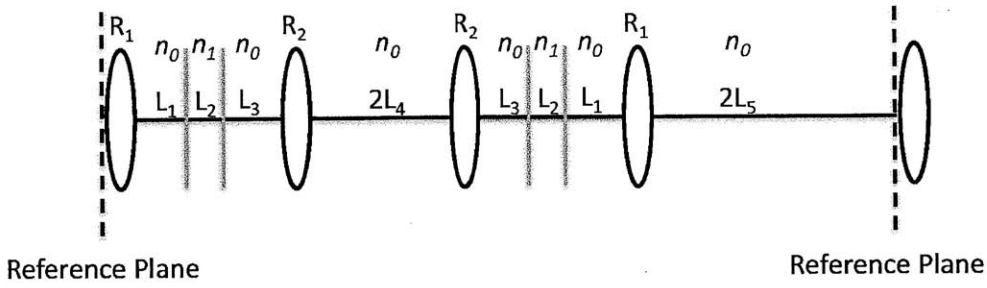

Figure 2.6 Equivalent unfolded system for the linear resonator.

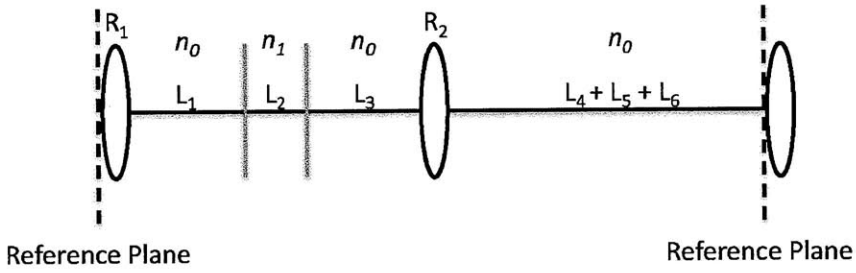

Figure 2.7 Equivalent unfolded system for the ring resonator.

Alignment of laser cavity: Linear resonator

Linear cavity Ti:sapphire lasers operated at a repetition rate of ~80MHz are commonly used in many ultrafast applications. For example, a soft-aperture KLM, 85MHz few-cycle laser is used for demonstrating gain-matched output couplers (Chapter 4) and broadband Cherenkov radiation in the few-cycle regime (Chapter 5). The Kerr-lens sensitivity of the linear laser cavity has been previously studied by modeling Kerr-medium as a nonlinear lens [31]. It is found both theoretically and experimentally that mode-locking can be initiated on the inner edge of the two stability regions in the asymmetric configuration ($L_4 \neq L_5$) or near the center of stability region in the symmetric configuration (($L_4 = L_5$) (see Figure 2.8)

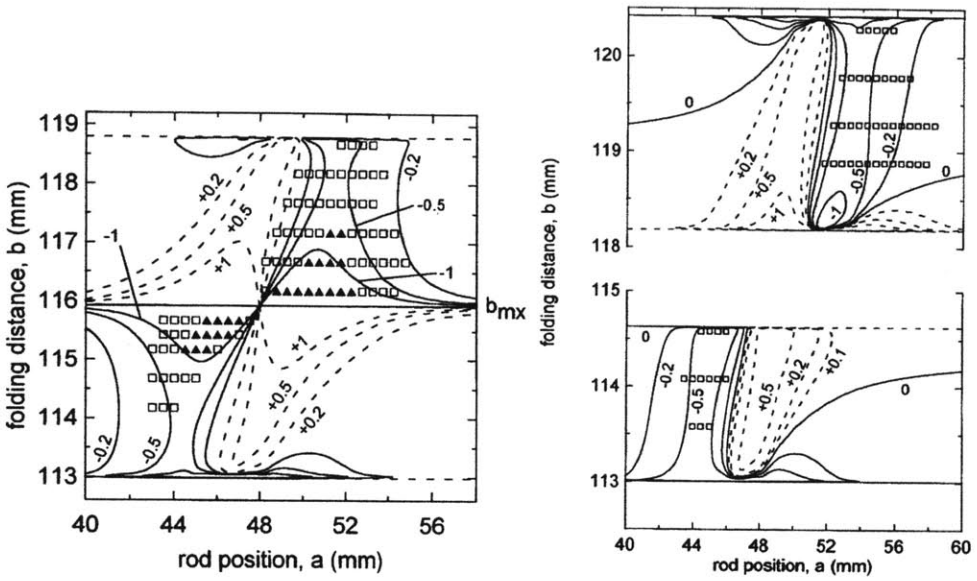

Figure 2.8 Example plots of Kerr-lens sensitivity analysis for symmetric (left) and asymmetric linear cavity (right). Figure adapted from [31] (Fig. 8 and Fig. 10)

The analysis of Kerr-lens sensitivity is usually performed on a specific cavity using sophisticated calculation that gives plots like those shown in Figure 2.8. The plots show a complex parameter dependence and as a result, building KLM mode-locked lasers is still very challenging for most laser users. Even for a simple laser, there are still many parameters that one can adjust. As a result, searching for an optimum operating point in a multi-dimensional space without any guidelines seems to be inefficient if not impossible. In order to provide more useful and general guidelines for the laser operation, the connection between the cavity stability region and the laser geometry will be discussed.

Stability Region

In the stability region, a standing wave can be formed in the cavity. Mathematically, it is judged by whether a self-consistent q-parameter exists or not, using equation (2.23). The stability region is usually given as a function of spacing between two curved mirrors (i.e. $L_1+L_2+L_3$). To simplify the analysis, we assume that the cavity is astigmatism-free. For a symmetric cavity, there is only one stability region which splits into two branches from the center when the symmetry is broken. Figure 2.9 shows that the two regions of stability become further apart as the cavity gets more asymmetric.

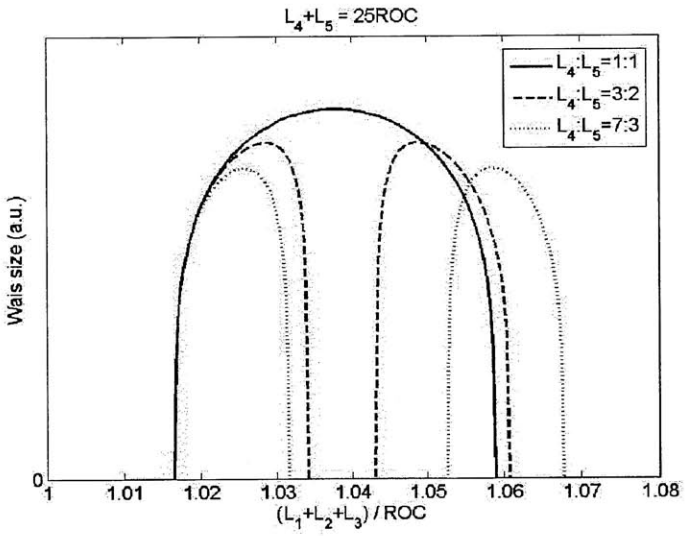

Figure 2.9 Beam waist size inside the crystal vs. asymmetry of the cavity

Understanding the evolution of the cavity mode inside the stability region is the key to successful KLM laser designs. When designing a new laser cavity or modifying an existing cavity operated at a certain repetition rate, it is particularly important to maintain the ratio between the length of collimated arm (L_1+L_2) and the ROC of the

mirrors within a certain range. As shown in Figure 2.10 and Figure 2.11, the ratio has a significant influence on the width of stability region and the beam waist size. The result suggests that increased asymmetry, i.e. a larger arm length ratio, narrows the width of the stability region and decreases the beam waist, which might dramatically shrink the region where the mode-locking can be initiated.

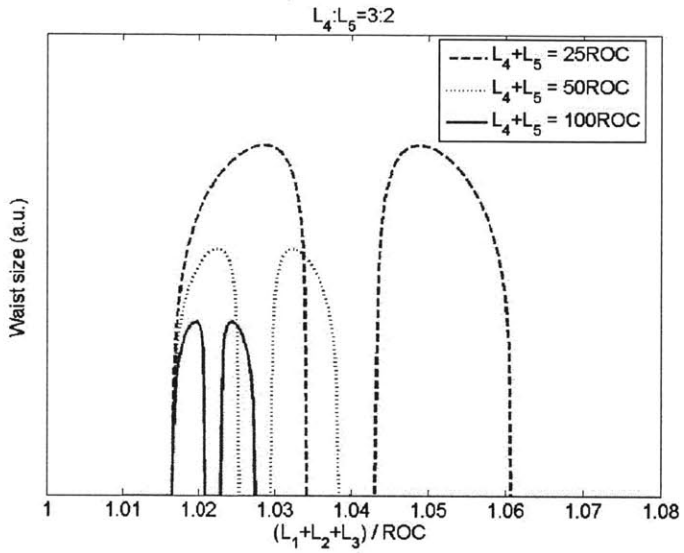

Figure 2.10 Beam waist size inside the crystal vs. total propagation length in the collimated arms

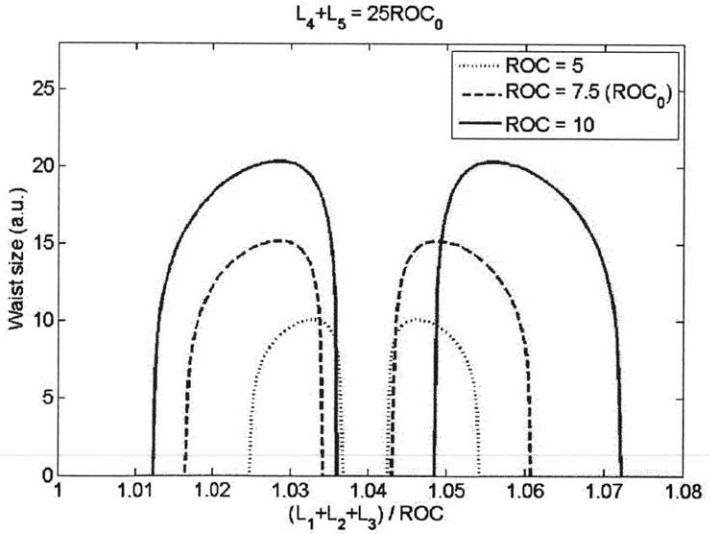

Figure 2.11 Beam waist size inside the crystal vs. total propagation length in the collimated arms

It should be noted that the beam waist size in these figures is calculated from the imaginary part of the q-parameter when the beam enters the crystal. In fact, the beam waist might be somewhere outside depending on the crystal position. Since the Kerr-lens effect depends on the pulse intensity, it is not surprising that it is easier to start the mode-locking when the beam waist is positioned inside the crystal, which corresponds to the high Kerr-sensitivity region shown in Figure 2.8.

Alignment Procedure

In a real laser cavity, astigmatism always exists, and therefore careful alignment must be performed to overlap the high Kerr sensitivity region on both planes. The alignment procedure consists of two steps that can be accomplished separately (refer to Figure 2.4):

(1) Compensate for the astigmatism introduced by the Ti:sapphire crystal (n = 1.76) by adjusting (θ_1, θ_2).

(2) Position the beam waist of the cavity mode at the right position inside the crystal by adjusting (L_1, L_3).

The first step creates a joint overlapping region of stability for sagittal and tangential plane. As mentioned earlier, the choice of (θ_1, θ_2) is not unique. Figure 2.12 shows the calculated compensating angles (θ_1, θ_2) with respect to different position d from the crystal surface near Mirror 1 based on the resonator geometry listed in Table 2.2.

R_1=R_2	L_2	L_4	L_5	θ_B
75 mm	2 mm	212 cm	125 cm	60.4 °

Table 2.2 Linear resonator parameters

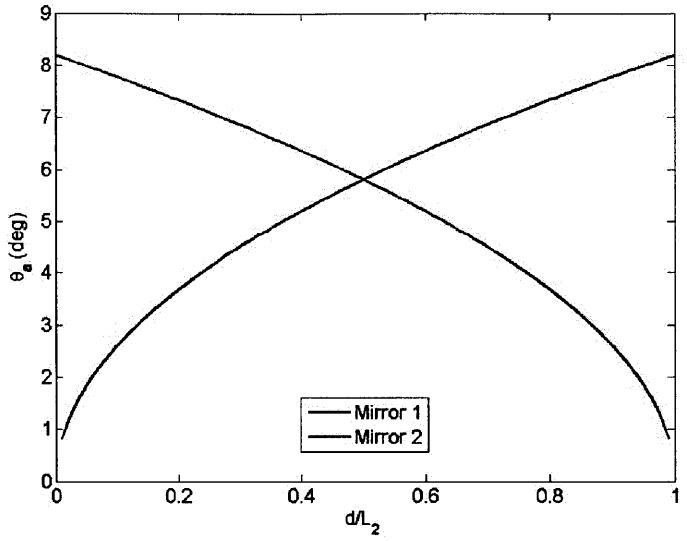

Figure 2.12 Astigmatism compensating angles for two curved mirrors; *d* is the distance from the crystal surface near Mirror 1 to the location of compensation.

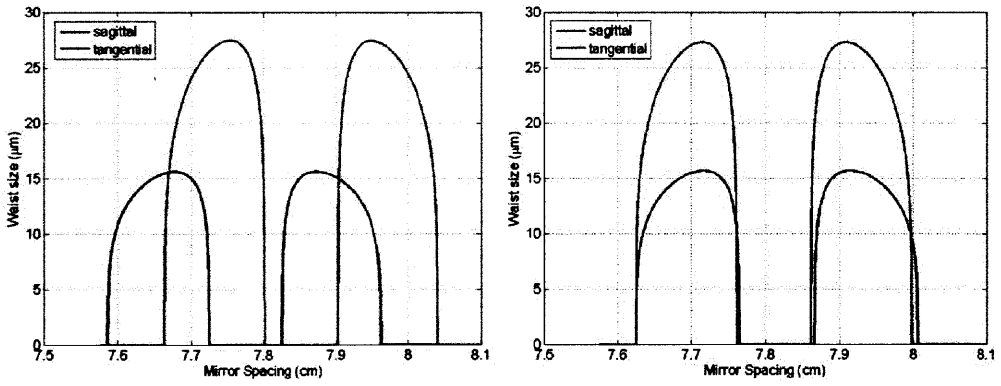

Figure 2.13 Region of stability for the 85MHz linear cavity without (left) and with (right) astigmatism compensation.

Figure 2.13 compares stability region of an uncompensated and a compensated cavity. In the two cases, the curved mirrors are tilted by 0° and 5.8°, respectively. As shown in the plot, the edges of stability region are well-aligned in the compensated cavity, implying that the high Kerr-sensitivity region for the sagittal and tangential planes have a better chance to overlap.

Intuitively, a good operating point should have an astigmatism-free beam inside the crystal, which means the real parts of the q-parameter in two orthogonal planes are the same. In this way, the beam focuses simultaneously in both planes which maximize the Kerr-lens effect. Experimentally, this is done by searching the two-dimensional parameter space created by L_1 and L_3. The searching procedure is usually executed in two alternating steps:

(1) The mirror spacing, defined as $L_1+L_2+L_3$, is adjusted by changing L_3 only, i.e., by moving mirror M_2.

(2) Then, the crystal position is adjusted to change the value of L_1 while keeping the mirror spacing fixed.

The values of L_1 and L_3 required for creating an astigmatism-free beam are shown in Figure 2.14 - Figure 2.16 for d = 0.5, 0.25, and 0.75 L_2, respectively. In principle, the region of stability can be divided into four zones with each marked by different colors. The outer edge of the stability region refers to zone A or D. The inner edge refers to zone B or C, which is also the region where mode-locking can be easily initiated.

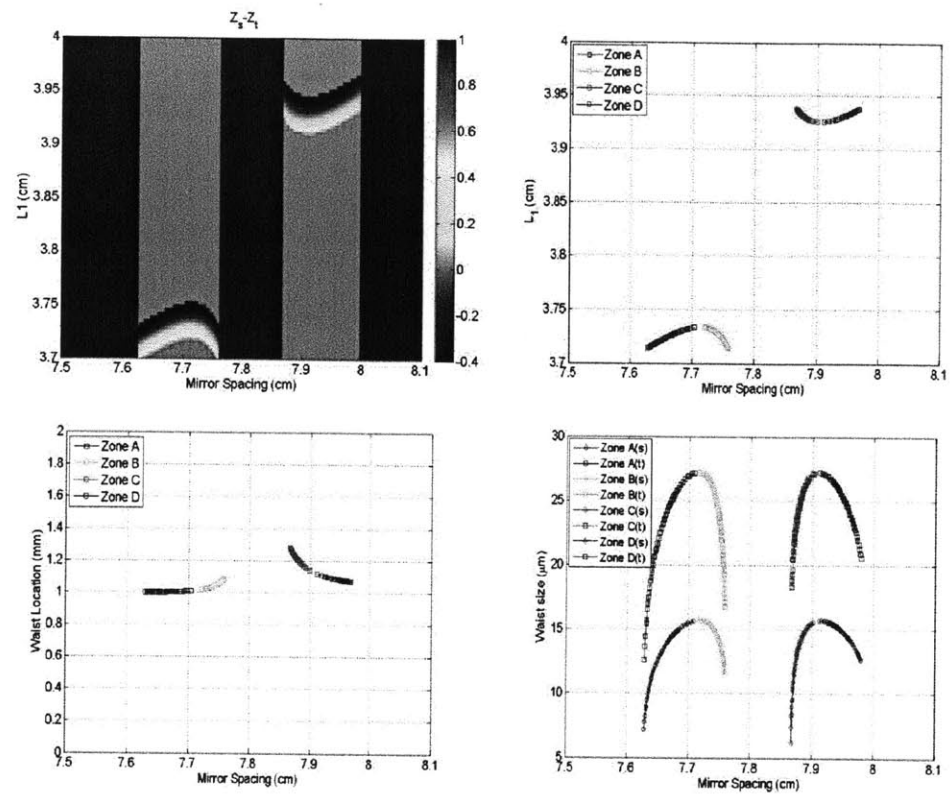

Figure 2.14 Analysis of astigmatism-compensated cavity with d=0.5L_2. (Top-left) Difference in real part of the self-consistent q-parameter at the crystal surface close to the mirror M_1 between sagittal and tangential plane. The value is normalized to the total crystal length L_2. (Top-right) L1 vs. mirror spacing for astigmatism-free operation. (Bottom-left) waist location inside the crystal for astigmatism-free operation. (Bottom-right) Waist size vs. mirror spacing

When designing KLM laser cavities, these plots are very convenient for studying the connection between laser performance and cavity parameters such as waist size and location inside the crystal for the laser beam. For example, Table 2.3 shows the action needed to move the beam waist location d inside the crystal while keeping the same waist size and operating on the edge of the stability region.

d	θ_1	θ_2	L_1	L_3	$L_1 + L_3$
↑	↑	↓	↓	↑	—
↓	↓	↑	↑	↓	—

Table 2.3 Action needed for moving the beam waist location d inside the crystal

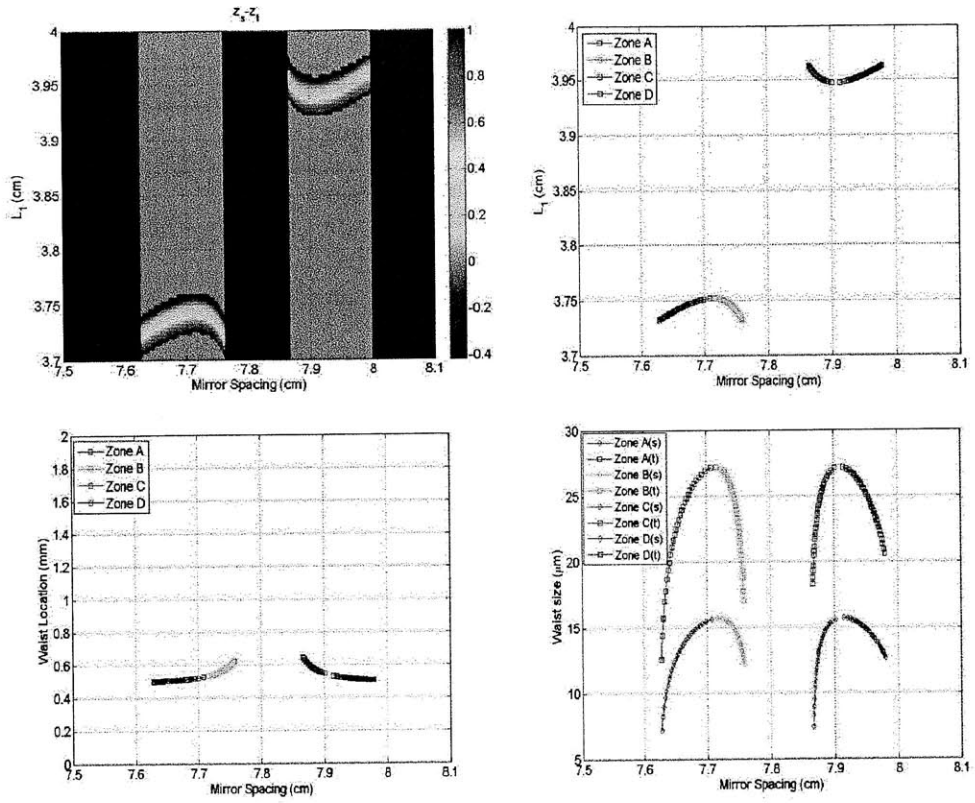

Figure 2.15 Analysis of astigmatism-compensated cavity with d=0.25L_2. (Top-left) Difference in real part of the self-consistent q-parameter at the crystal surface close to the mirror M_1 between sagittal and tangential plane. The value is normalized to the total crystal length L_2. (Top-right) L1 vs. mirror spacing for astigmatism-free operation. (Bottom-left) waist location inside the crystal for astigmatism-free operation. (Bottom-right) Waist size vs. mirror spacing.

Toward	θ_1	θ_2	L_1	L_3	$L_1 + L_3$
Edge	—	—	↓	↑ ↑	↑
Center	—	—	↑	↓ ↓	↓

Table 2.4 Action needed for changing the beam waist size in zone B

Toward	θ_1	θ_2	L_1	L_3	$L_1 + L_3$
Edge	—	—	↑	↓ ↓	↓
Center	—	—	↓	↑ ↑	↑

Table 2.5 Action needed for changing the beam waist size in zone C

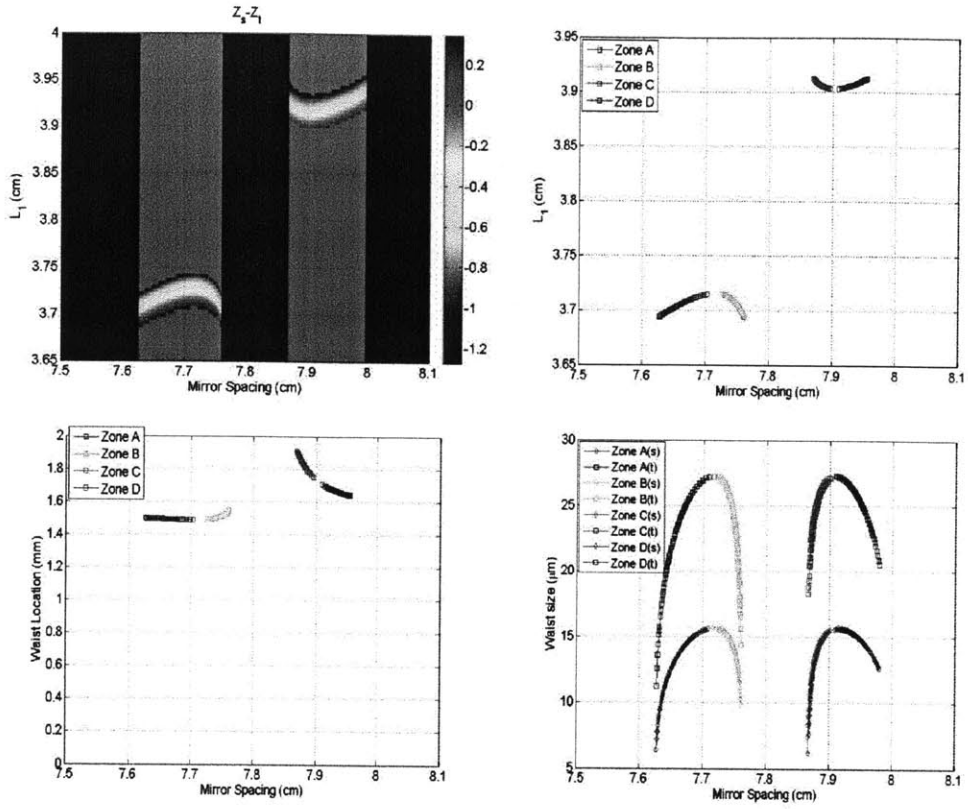

Figure 2.16 Analysis of astigmatism-compensated cavity with d=0.75L_2. (Top-left) Difference in real part of the self-consistent q-parameter at the crystal surface close to the mirror M_1 between sagittal and tangential plane. The value is normalized to the total crystal length L_2. (Top-right) L1 vs. mirror spacing for astigmatism-free operation. (Bottom-left) waist location inside the crystal for astigmatism-free operation. (Bottom-right) Waist size vs. mirror spacing.

Besides moving the beam waist, other important optimization parameters include the size of beam waist and the operating point on the edge of stability region. When one moves the operating point toward the edge, the beam waist becomes smaller. Table 2.4 and Table 2.5 provide useful guidelines for adjusting the beam waist while keeping other parameters unchanged. As can be seen, either moving the beam waist or changing its size cannot be accomplished with one parameter (L_1 or L_3) alone. As a result, the alignment becomes difficult without these guidelines in mind.

Alignment of laser cavity: Ring resonator

Ring cavities have only one region of stability, similar to symmetric linear cavities. Take a 2GHz ring cavity with 2.5cm ROC mirrors as an example. Same analysis is performed with $d = 0.5\ L_2$, and shown in Figure 2.17. The top-left plot shows the "hot zone" formed by the choice of L_1 and L_3 and the top-right plot draws a contour where the cavity beam is astigmatism-free inside the crystal. Experimentally it is found that mode-locking can be initiated on the left edge. The geometric parameters for the marked operating point are listed in Table 2.6.

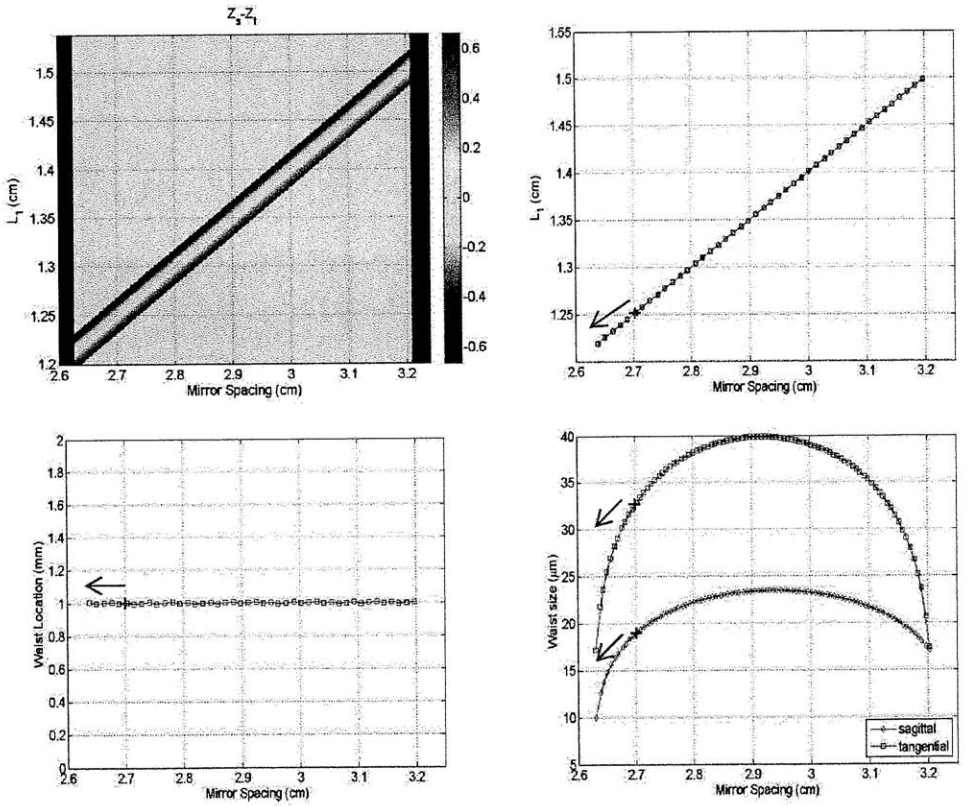

Figure 2.17 Analysis of astigmatism-compensated ring cavity with d=0.5L_2. (Top-left) Waist location difference between sagittal and tangential plane. (Top-right) L1 vs. mirror spacing for astigmatism-free operation. (Bottom-left) waist location inside the crystal for astigmatism-free operation. (Bottom-right) Waist size vs. mirror spacing. The red mark shows the current operating point and the arrow shows the desired direction of optimization.

R_1=R_2	L_2	$L_1 = L_3$	$\theta_1 = \theta_2$	$L_4 + L_5 + L_6$
25 mm	2 mm	1.25 cm	10.03 °	~12cm

Table 2.6 2GHz ring resonator parameters for the marked operating point.

One might think that a similar optimization approach used in linear cavities can be applied in ring cavities. As a matter of fact aligning ring cavities is not as trivial as linear cavities because ring cavities have a closed beam path defined by all the cavity components together. Unlike linear cavities whose folding angle and the distance between crystal and the curved mirror can be controlled independently in both arms, adjusting any single component in a ring cavity results in a change in the whole beam path. As an example, Figure 2.18 shows the ideal beam path when the laser operates in the marked operating point. For best laser efficiency, the pump beam must overlap with the cavity beam inside the gain medium (i.e. $\overline{BC}$). Assuming we want to make the beam waist smaller to see whether the laser performance can be improved or not. In linear cavities, this can be easily done by moving the laser crystal and one mirror by Δx and $2\Delta x$ in the same direction. However, when similar method is applied to the ring cavity, a new beam path will be defined and hit on a different spot on each component. This will lead to a change in all the folding angles, as shown in Figure 2.19, and the cavity astigmatism becomes no longer compensated. Most importantly, the cavity beam will propagate along different path $\overline{B'C'}$ as the pump beam path $\overline{BC}$. As a result, the high-order transverse modes are excited and the output power drops. Experimentally, we often found that the structure of the high-order modes belongs to the Ince-Gaussian family, meaning that cavity astigmatism is present [32].

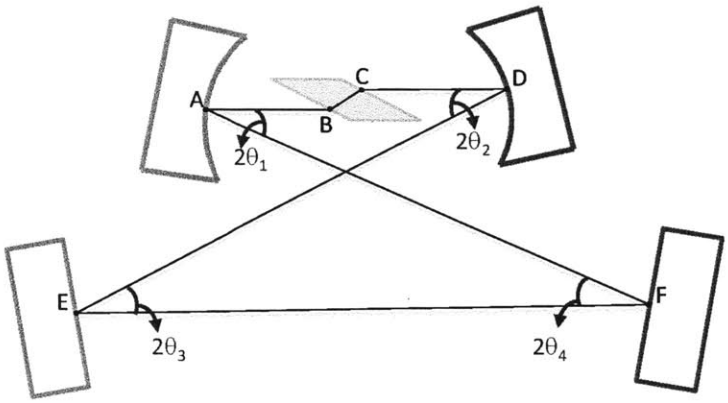

Figure 2.18 Geometry of a 2GHz ring cavity operated at an astigmatism-free operating point (marked in red in Figure 2.17). Points A-F indicate the position of each components that the cavity mode hits on.

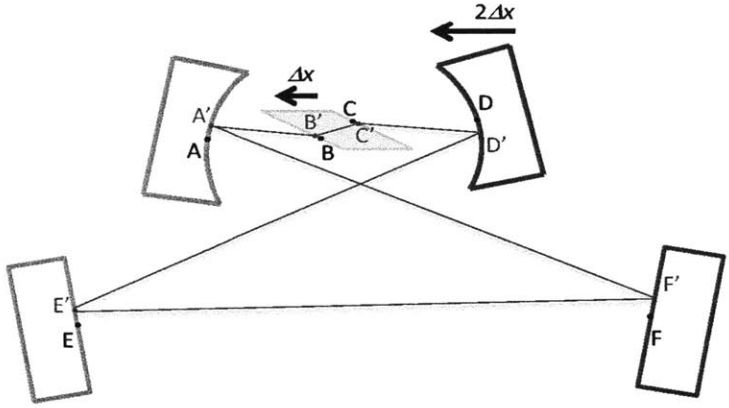

Figure 2.19 Change in cavity mode path when moving the laser crystal and one mirror by Δx and $2\Delta x$ in the same direction. Points A'-F' indicate the new position that the cavity mode hits on.

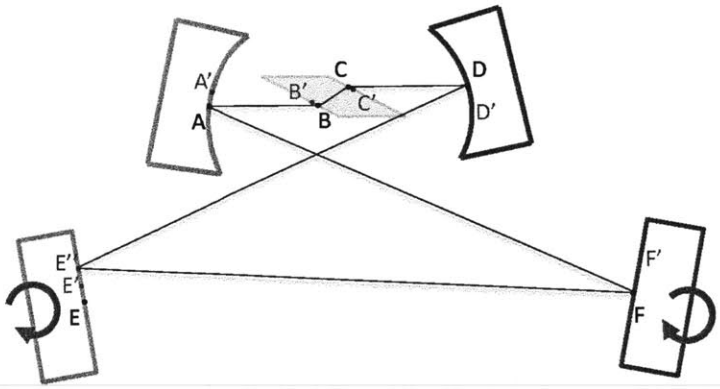

Figure 2.20 Schematic showing how to compensate for the cavity beam path change. When both flat mirrors are tilted clockwisely, the cavity mode could hit the original positions A-F except point E and the cavity is operated at the astigmatism-free point again.

To fix the problem addressed above, one must adjust the tilt of the two flat mirrors. From our cavity path solver, we found that the two mirrors need to rotate clockwisely by some small amount as shown in Figure 2.20. The calculation shows that, when the astigmatism is compensated again, the cavity mode will hit the original positions on every component except for one flat mirror M_3.

2.3. Kerr-lens Mode-locking

Kerr-lens modelocking (KLM) is a method of modelocking lasers via a nonlinear optical process known as the optical Kerr effect. This method allows the generation of pulses of light with a duration as short as a few femtoseconds. To favor the pulsed mode over cw, the cavity design should emphasize aperture effects. Older designs use a hard aperture that simply cuts off the cw beam that is not influenced by the Kerr effect. Modern designs, which are also the topic of our interest in this thesis, use a soft aperture defined by the overlap between the pumped region of the gain medium and the pulse. In the case of soft aperture KLM, the Kerr lens leads to a better overlap of laser and pump beam, and thus to a higher gain for the peak of the pulse, as shown in Figure 2.21. This phenomenon provides a mechanism for self-amplitude modulation (SAM) that keeps shortening the pulse until other pulse lengthening effects such as gain-filtering and dispersion come into play and balance the pulse duration.

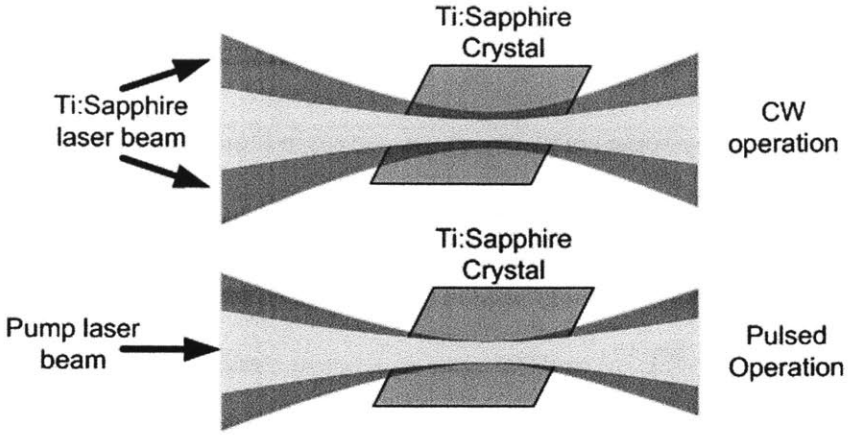

Figure 2.21 Concept of soft-aperture Kerr-lens mode-locking.

2.3.1. Dispersion Management

Precise control of cavity dispersion is a key to the generation of ultra-broadband pulses from a laser cavity. In a prism-free KLM cavity, the dispersion usually comes from the material and cavity mirrors. The material dispersion is unavoidable but can be well characterized and described by Sellmeier equations. Since the materials usually provide positive (or normal) dispersion around the wavelength of interest (800nm), the main goal of the laser mirror design is to provide opposite dispersion of the intracavity materials over a large wavelength range.

Materials

The Sellmeier equation describing the material dispersion is usually in the following form

$$n^2(\lambda) = 1 + \frac{B_1\lambda^2}{\lambda^2 - C_1} + \frac{B_2\lambda^2}{\lambda^2 - C_2} + \frac{B_3\lambda^2}{\lambda^2 - C_3}, \tag{2.33}$$

where n is the refractive index, and λ is the wavelength $B_{1,2,3}$ and $C_{1,2,3}$ are experimentally determined Sellmeier coefficients. These coefficients are usually quoted for λ in microns in vacuum.

	B_1	B_2	B_3	C_1	C_2	C_3
Ti:Sapphire	1.023798	1.058264	5.280792	0.0037758	0.012254	321.3616
Air	0.0002463	0.000299	-	0.0082250	0.003637	-
BaF_2	0.643356	0.506762	3.8261	0.0033396	0.012029	2151.698
Fused silica	0.68374	0.42032	0.58503	0.0046035	0.013397	64.493

Table 2.7 The Sellmeier coefficients of the commonly used material in prism-less KLM laser cavity. The coefficients for air are for NTP condition.

Double-chirped mirrors

Dispersion compensating chirped mirrors are similar to dielectric Bragg type reflectors in that they both use quarter-wave thickness layers of dielectric materials for generating multiple reflections to ultimately achieve a high reflectivity. While Bragg reflectors have layers with only one (optical) thickness through the material, the layer thickness in a dispersion compensating mirror is slowly changed or "chirped" for each layer, resulting in a wavelength dependent penetration depth into the mirror coating.

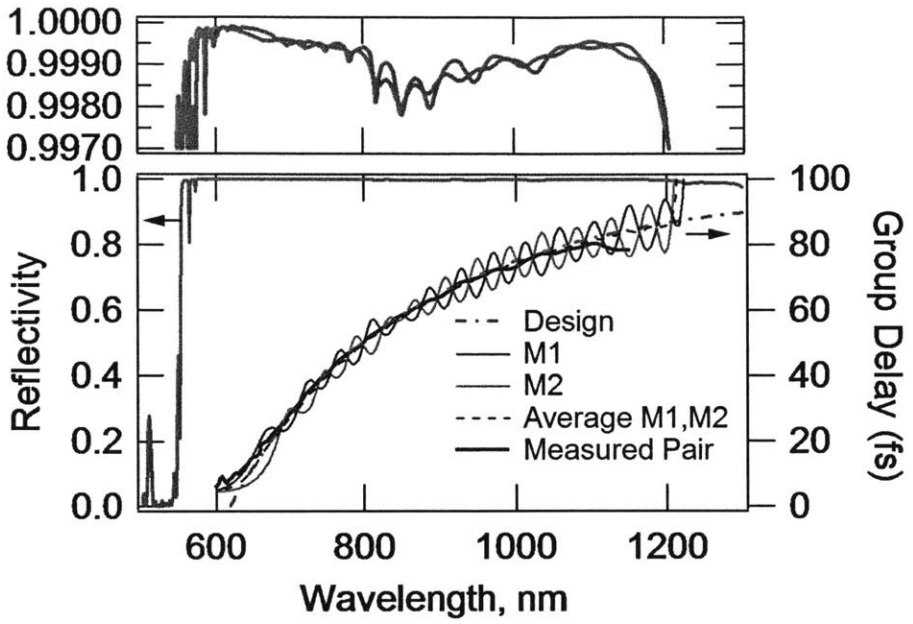

Figure 2.22 Reflectivity and group delay for a typical double-chirped dispersion compensating mirror pair used in the octave-spanning Ti:Sapphire laser. The high reflectivity band extends from 600 – 1200 nm, with a region of extremely low reflectivity near 532 nm to allow transmission of light from the pump laser. In the lower portion of the graph is the designed and measured group delay for each mirror as well as the average value.

A subtlety of the mirror design requires that the mirrors be used in pairs. The requirement is a result of a design modification necessary for broadband operation. Most wavelengths must penetrate into the layer stack a finite distance before being reflected, so it turns out to be necessary to use an anti reflection (AR) coating on the front surface of the chirped layer stack. This AR coating prevents small spurious reflections generated by the impedance mismatch between air and the first layer from destabilizing the mode-locking process. An elegant solution to this problem is to insert a quarter-wave-thickness layer for the central wavelength between the AR coating and the chirped layer stack. In the frequency domain, these spurious reflections are equivalent to an oscillating group delay. The addition of the quarter wave layer shifts the oscillations by a phase of π, allowing

cancellation of the reflections when such mirrors are used in pairs. This type of mirror is referred to as double chirped dispersion compensating mirrors (DCM). Figure 2.22 shows the typical performance of a DCM pair that can support octave-spanning operation of the Ti:sapphire lasers. The dispersion of the mirrors is carefully engineered to compensate the normal dispersion (including the high-order dispersion) in the laser cavity caused by air and sapphire crystal. Determining the exact dispersion compensating scheme is simply a matter of summing the contribution from each element. Since there is a rather large uncertainty in this calculation due to residual oscillations in the group delay of the DCMs, it is better to allow for some tuning of this value in the construction of the laser than to try to achieve a particular value. Experience has shown that this method is reasonably reliable for achieving broadband mode locking.

2.4. Octave-spanning, Dual-output 2GHz Ti:sapphire Laser

In this section, a self-referenced octave-spanning Ti:sapphire laser with a repetition rate of >2 GHz is demonstrated., which shows to our knowledge the highest repetition rate. A ~20dB improvement (using 100kHz RBW) of CE beat note for a gigahertz-repetition-rate phase-stabilized laser oscillator is proved. This is possible, because the laser uses specially designed double-chirped mirror pairs [33–35] with excellent dispersion characteristics over the full Ti:sapphire gain bandwidth. In addition, one of the mirrors is designed to transmit the 1f and 2f spectral components used for CE-phase stabilization as a second output, separately from the main output from the output coupler, in a non-intrusive manner [36], [37]. This

design allows the laser to deliver a phase-stabilized, octave-spanning laser beam directly from the main output ready for future applications.

2.4.1. Motivations

Over the past few years, several Ti:sapphire lasers [38–43], with gigahertz-repetition rates up to 10 GHz achieved most recently [44], have been demonstrated. However, octave spanning operation was only obtained up to 1.35 GHz by Fortier *et al.* and at the high end the CE beat note was already reduced from 31 to 25 dB measured with a 300kHz resolution bandwidth (RBW) when increasing the repetition rate from 550MHz to 1.1GHz [40], making a transfer oscillator necessary. Although these authors have shown that the continuum generation resulting from an enhanced self-amplitude modulation by introducing a convex mirror can be used to assist octave-spanning operation even when the dispersion is only controlled across the center portion of the Ti:sapphire gain bandwidth, we demonstrate here that broadband dispersion compensation helps to maintain an octave spanning spectrum for even 2GHz repetition rate.

2.4.2.Cavity Design and Alignment

The laser setup is shown in Figure 2.23. We use a 4-mirror Kerr-lens-mode-locked (KLM) ring cavity consisting of two dispersion-matched pairs of broadband double-chirped mirrors (DCM), (M1,M2) and (M3,M4), which is a modified design based on our recently proposed configuration for maximum carrier-envelope (CE) beat signal generation [36], [37]. A 2.2 mm long Brewster-cut Ti:sapphire crystal (α=4.5 cm^{-1}) is located between two concave DCMs with a radius of curvature

(ROC) of 2.5cm. The laser is pumped by a multimode diode-pumped solid-state laser (Millennia Xs) through a lens with a focal length of 4 cm. The folding angle at the curved mirrors is set to 21 degree for astigmatism compensation. To increase the stability of the laser when mode-locked at high repetition rate, we replace M4 with a slightly convex mirror (ROC=50 cm), instead of using two flat mirrors for the second DCM pair. It was pointed out earlier by Bartels *et al.* [39] that this configuration leads to a stronger self-amplitude modulation coefficient or KLM strength δ inside the cavity.

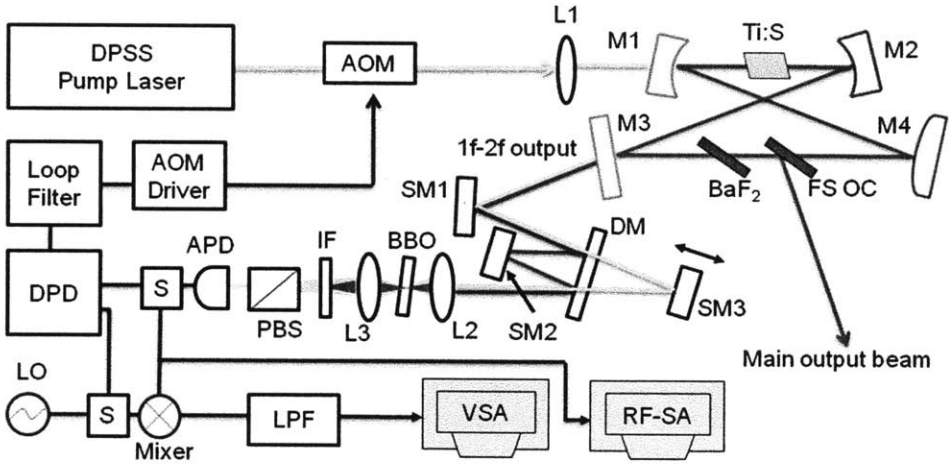

Figure 2.23 Setup of CE phase stabilized octave-spanning Ti:sapphire (Ti:S) laser and phase-locking electronics. The four-mirror cavity is formed by two pairs of DCM, (M1,M2) and (M3,M4). M1 and M2 are concave mirrors (ROC=2.5cm). M4 is a convex mirror (ROC= 50 cm). AOM, acousto-optic modulator; L1, pump lens (f= 4 cm); FS OC, wedged fused silica output coupler; SM1-3, silver mirrors; DM, dichroic mirror; L2-L3, lens (f=20mm); IF, interference filter centered at 580nm; PBS, polarization beamsplitter; APD, avalanche photodetector; DPD, digital phase detector; S, power splitter; LO, local oscillator; LPF, low-pass filter; VSA, vector signal analyzer; RF-SA, RF spectrum analyzer.

The DCMs used here are identical to those in Ref. [37] and are designed to have a smooth average group delay and negative group delay dispersion (GDD) from 650 to 1100 nm to compensate for the positive dispersion of all other

intracavity elements in this spectral range of interest. The coating on M3, same as M1, is designed to transmit 50% of the intracavity power around *f* and *2f* components, which allows the main output to be completely separated from the 1f-2f output (coupled out from M3) so that the main pulses are not affected by any extracavity manipulations needed for CE-phase stabilization. A 1.5 mm-thick BaF_2 plate and a 1 inch long fused-silica (FS) wedge with a central thickness of 1.7 mm are placed at Brewster angle. The corresponding path length of BaF_2 and FS is 1.83 mm and 2.12 mm, respectively. Although there are some remaining fluctuations in the GDD of the DCMs for discussion of the dispersion compensation the average GDD curve is used. As shown in Figure 2.24, considering the dispersion of all intra cavity components as well as the air path results in a vanishing net average GDD within a few fs^2 over the entire bandwidth of the Ti:sapphire crystal, which is the key to the generation of octave-spanning spectra [45]. Due to the physical limits of our cavity, the FS-wedge, which is used for fine-tuning of the intra cavity dispersion and the carrier-envelope offset frequency, is vertically mounted (perpendicular to the table) to maximize the range of adjustment. A 2% broadband output-coupler (OC) coating carried by the wedge is designed to enhance the spectral wings of the output pulses by increasing the reflectivity to >50% below 650 nm and above 1050 nm.

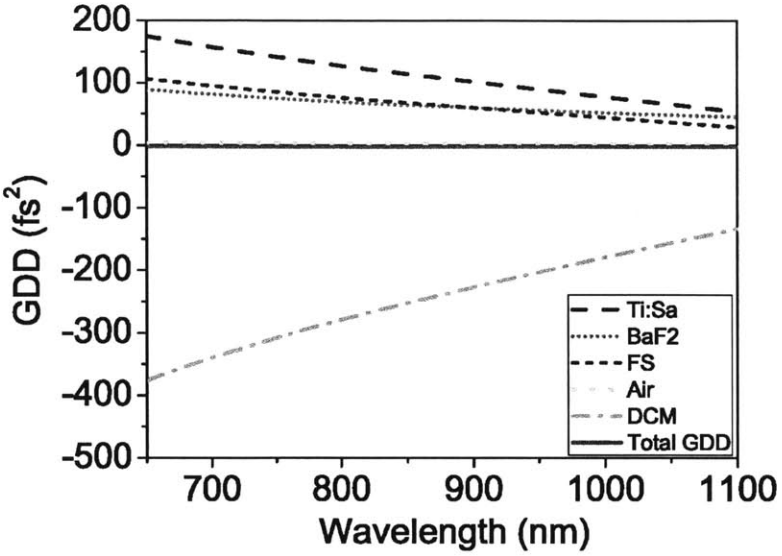

Figure 2.24 Calculated total intra cavity GDD (red solid curve) and individual GDD for each component including 2.2mm Ti:Sa (black dashed curve), 1.83mm BaF_2 (purple short dotted curve) , 2.12mm FS (blue short dashed curve), 15cm air (green dotted curve), and 2 DCM pairs (gray dash dotted curve)

The cavity was initially aligned for best continuous-wave operation, which was judged by having a maximized output power and a clear transverse-mode transition from fundamental TEM_{00} to circular symmetric higher-order modes when translating mirror M2 towards M1 at the inner edge of the stability region. Both criteria are very important for achieving optimum KLM because the former ensures that the laser gain is maximized, while the latter helps to verify that there is no transverse displacement or angular tilt between the optical axes of the cavity and the pump beam [46]. When above criteria are met, bidirectional mode locking is easily initiated by pushing M2 inward to the position where the first or second higher-order mode was supposed to appear. Unidirectional mode-locking is finally achieved by further translation of M2 by a few tens of microns.

2.4.3. Laser Performance

Figure 2.25 shows the radio-frequency (RF) spectra of the directly detected pulse stream when the laser is in unidirectional operation. The clean RF-spectrum indicates stable fundamental mode locking with a repetition rate of ~2.166 GHz which is slightly higher than our previous result [47]. At 10.5 W of pump power the laser generates a total output power of 812 mW including a main output of 750 mW and a 1f-2f output of 62 mW.

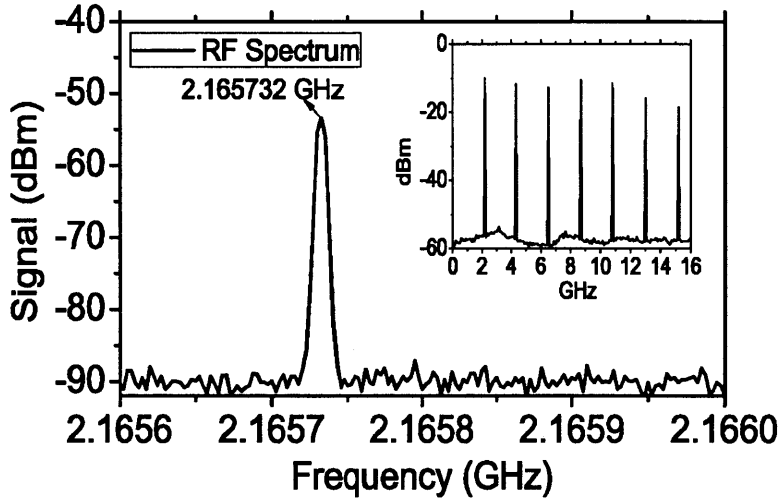

Figure 2.25 RF spectrum of pulse train detected with a 10 GHz photo detector: With high resolution at the fundamental repetition rate of 2.166 GHz; inset shows full spectrum up to 16 GHz.

For comparison, the calibrated spectra displaying power spectral density for both outputs are shown in the same plot (see Figure 2.26). The spectral components of the 1f-2f output below 600 nm and above 1120 nm, although containing only a few percent of the total power, are stronger than the main output. The result matches perfectly with our DCM design [45], [48] and also shows that we can generate the necessary 1f-2f components in a very simple and efficient way without

affecting the main output of the laser. Moreover, the main output covers a spectral range of more than 700 nm (extending from 570 nm to 1300 nm, when considering a 30 dB dynamic range from the maximum at 800 nm). The power per mode in the center of the spectrum is 18 μW with more than 100 nW per mode available from 250 THz to 500 THz. The power leaving the 1f-2f output port within a 10 nm bandwidth located at 580nm and 1160nm, the wavelengths used for the CE-lock, are 0.884 mW and 4.49 mW, respectively, which is more than enough power for subsequent self-referencing.

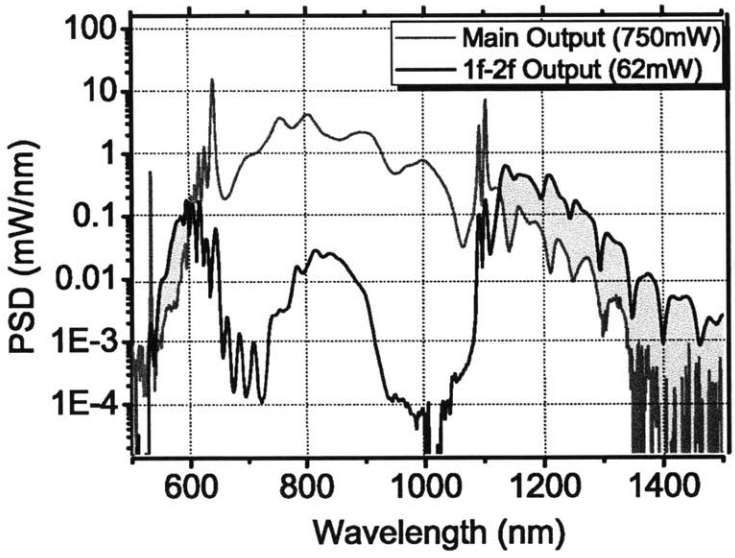

Figure 2.26 Output spectra of (a) 1f-2f output beam (black curve) and (b) main output beam (red curve) from the laser. The filled area between two curves visualizes that the spectral components of 1f-2f output below 600 nm and above 1120 nm are stronger than in the main output.

2.4.4. Carrier-envelope Phase Stabilization

The CE-phase is detected with a 1f-2f interferometer at the output of M3 (see Figure 2.23) where a dichroic mirror is used to separate the 1f and 2f components for proper group delay adjustment to maximize the CE-beat signal. The f-to-2f beat

note is generated and collected through a pair of uncoated lenses with a focal length of 2 cm. The first lens was used to focus the laser beam into a 1 mm-BBO crystal for second-harmonic generation (SHG), while the other is used to collect and re-collimate the fundamental and generated SHG beams, which are then filtered by a 10-nm-bandwidth interference filter centered at 580 nm, and directed to a fast avalanche photodiode (MenloSystems APD210). The delay line based on a dichroic beam splitter, rather than DCMs, is used for generating the CE-beat note since the overall achievable CE-phase error was dominated by the noise from the multimode pump laser used [36], [37], [49]. This simple and inexpensive scheme still generates a free-running CE beat note with a SNR of 50 dB measured in a 100 kHz resolution bandwidth (see Figure 2.27 (a)) and a similar result for the integrated residual phase jitter when compared with our previous lasers using the same type of pump laser [49], [50].

The CE-offset frequency (f_{ceo}) is locked to a local oscillator (LO) set at 20MHz through a phase-locked loop (PLL) (see Figure 2.23) that feeds the phase difference between the CE-beat signal and the LO to an acousto-optic modulator regulating the pump power, thus shifting the CE-frequency. The PLL uses a digital phase detector to increase the capture range ($-32\pi \sim +32\pi$) beyond a traditional analog mixer ($-\pi/2 \sim +\pi/2$). Figure 2.27 (b) shows the measured RF spectra of the CE beat note signal in both linear and log scale when the laser is locked. As demonstrated by the plot, a delta-function-like CE beat note with a linewidth of <10 Hz (the resolution limit of our RF spectrum analyzer) is achieved. The central peak within four times the 10Hz resolution bandwidth (RBW) contains 91% of the

overall power that takes the entire pedestal caused by the amplitude and phase noise into account. In order to precisely estimate the residual CE phase error when the laser is locked, the following measurement is done. The residual phase noise of our system was obtained by splitting the CE-beat note signal and mixing one part of it directly with the local oscillator signal using a broadband analog mixer because it is difficult to measure the small residual phase fluctuations from the digital phase detector. The output from the mixer was filtered by a 10 MHz low-pass filter and fed into a vector signal analyzer (VSA) for measuring the one-sided power spectral density (PSD) of the residual CE fluctuations S_{ϕ}, (see red curve in Figure 2.27 (c)). The dashed curve in the same plot shows the integrated CE root-mean-square phase error$\Delta\phi(f) = [\, 2\int_{1MHz}^{f} S_{\phi}(f')df']^{\frac{1}{2}}$ calculated from

$$\Delta\phi_{rms} = [-\int_{1MHz}^{f} S_{\phi}(f')df']^{1/2} \tag{2.34}$$

Although in general it is true that the range of integration should be up to Nyquist frequency [51], i.e., 1 GHz, it is difficult to measure S_{ϕ} at high frequencies as it is lower than the noise floor set by the photodetector. This has to be expected, since the major source of carrier envelope phase noise are intracavity intensity fluctuations, which rapidly decay beyond the relaxation frequency of Ti:sapphire lasers, which is typically a few hundred kHz. Therefore, the upper limit of integration in our case is set to be 1 MHz to exclude the high-frequency noise contributed by the noise floor rather than the laser phase noise itself. The accumulated phase error integrated from 0.1 Hz to 1 MHz is 0.187 rad. This is equivalent to a timing jitter of 79 as at the center wavelength of 800nm, which is

slightly better than earlier constructed Ti:sapphire combs pumped by a multimode laser. Multimode pump lasers are known to have significantly higher relative intensity noise than single-mode pump lasers at high frequencies, where the feedback loop of the PLL has already low gain for stability reasons or it is already outside the loop bandwidth at all [49], [50]. Thus the CE-phase noise can be further suppressed by switching to a single-frequency pump source such as Coherent Verdi-10.

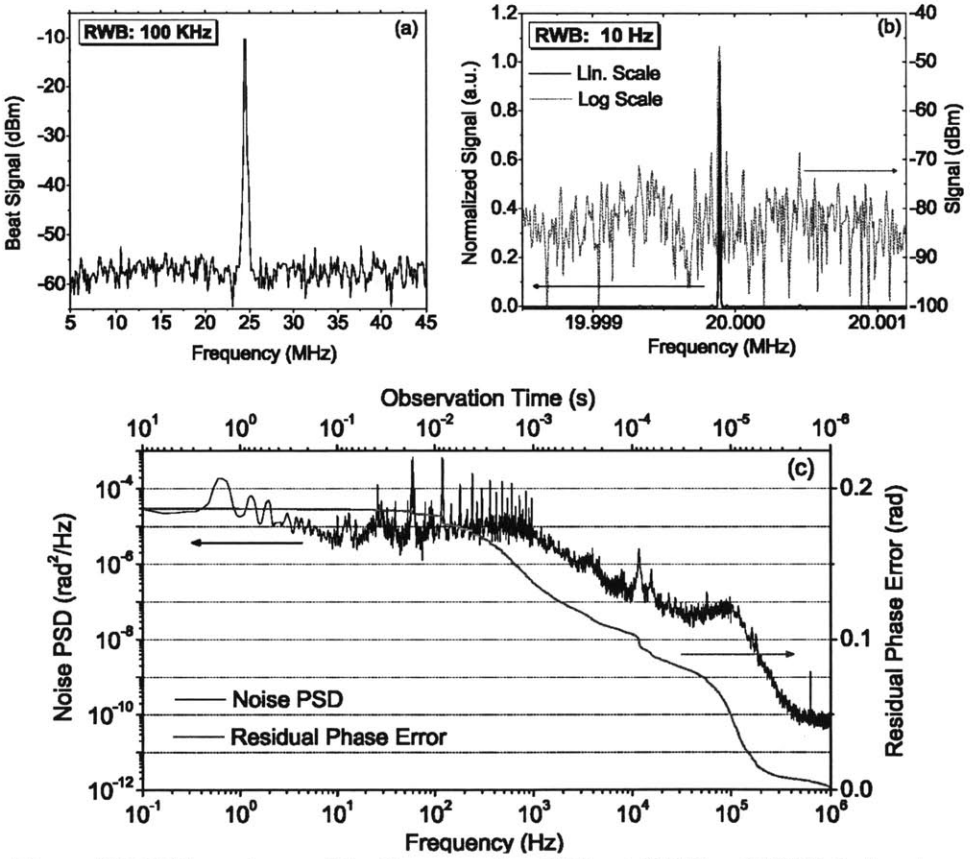

Figure 2.27 RF spectrum of the free-running CE-beat (RWB = 100 kHz) showing a SNR of ~50 dB. (b) RF spectrum of the locked CE-beat signal in log scale (red dotted curve) and linear scale (black solid curve) showing a resolution-limited linewidth of 10 Hz. (c) Power spectral density (PSD) of the residual carrier-envelope phase fluctuations (black curve) and integrated carrier-envelope phase error (red curve). The accumulated phase error integrated from 0.1 Hz to 1 MHz is 0.187 rad.

2.4.5. Conclusion

In conclusion, we demonstrated a self-referenced octave-spanning Ti:sapphire laser operating with the highest repetition rate of >2GHz while maintaining a strong (>50dB) CE-beat note in a 100kHz resolution bandwidth. The laser cavity uses novel double-chirped mirror pairs that provide both the main octave-spanning output carrying more than 90% of the total output power and a separate output port for the 1f-2f frequency components used for non-intrusive carrier-envelope phase-stabilization.

Chapter 3

Spatiotemporal Model for Octave-Spanning Ti:sapphire lasers

3.1. Motivations

With the advances in Kerr-lens mode-locked (KLM) solid-state laser technology nowadays, generation of few-cycle optical pulses directly from a laser cavity with a broadband gain medium such as Ti:sapphire and other Chromium-doped crystals has been routinely achieved. Despite the great success in constructing few-cycle lasers, the spatiotemporal pulse dynamics in this regime has not been precisely understood from the existing numerical models. In the early spatiotemporal models proposed by Herrmann [25], [52] and Christov [53–57], spatial effects in the Kerr-lens mode-locking process such as gain-guiding and space-time astigmatism were first studied. Nevertheless, these models are only able to simulate and provide design guidelines for the lasers delivering pulses as short as sub-10fs. In order to simulate sub-two-cycle or even octave-spanning Ti:sapphire lasers demonstrated with the ultra-broadband dispersion-compensating-mirrors, a pure temporal approach was employed by Sander [48] in 2009, in which all the spatial effects were modeled by an artificial saturable absorber. Although the laser spectra seen from the experiments become numerically reproducible in this approach, the

physics behind many phenomena in these few-cycle lasers has not been unveiled. First of all, these lasers not only show variation in spot size at different wavelengths, the mode structure also changes across the entire spectral range. In addition, some pronounced spectral peaks are often found across the entire spectrum with its dependence on the cavity dispersion unanswered. The main challenge is that, in these ultra-broadband lasers, much shorter pulses and much higher intracavity intensities are reached inside the gain medium in comparison to lasers delivering pulses longer than 10fs. Therefore, the intracavity pulses experience stronger phase modulation when propagating through the nonlinear medium. The modulation leads to coupling between longitudinal and transverse modes of the laser simultaneously from the self-phase modulation (SPM) and self-focusing (SF) effects that dominate the spatiotemporal dynamics of the pulse. Moreover, since the beam is usually tightly focused onto the gain medium, the peak intensity could reach to the level where the multi-photon processes (ionization and absorption) might become non-negligible. These processes not only add perturbations to the pulse dynamics but also provide feedback to the mode-locking itself by introducing nonlinear losses and plasma defocusing to the pulse transients. In this chapter, an extended 3-D numerical model is developed capable of dealing with the complete spatiotemporal dynamics of a dispersion-managed, Kerr-lens mode-locked Ti:sapphire laser operating in the few-cycle regime.

3.2. NLSTPEE for Pulse Propagation

To study the spatiotemporal dynamics of the optical pulse circulating inside the laser cavity, the pulse evolution within one round-trip needs to be modeled and simulated in a numerically efficient way. The nonlinear propagation of the pulse through the crystal can be modeled by a three-dimensional nonlinear spatiotemporal pulse evolution equation (NLSTPEE). The equation is valid for pulses in single-cycle regime as long as the envelope and the phase of the electric field slowly vary. This is also known as slowly-evolving-wave-approximation (SEWA) [58]. The NLSTPEE equation is generally written using a retarded time $\tau \equiv t - z/v_g$ as:

$$\frac{\partial A(x,y,z,\tau)}{\partial z} = \left(\hat{L} + \hat{N}\right) A(x,y,z,\tau) \tag{3.1}$$

A is the complex envelop function with its amplitude normalized to the intensity I (i.e. $|A|^2 = I$). The operator $\hat{L}$ accounts for the linear effects including diffraction (first term) and dispersion (second term) which are independent of pulse intensity, and are given by

$$\hat{L} = \left[-T^{-1} \frac{j}{2n_0 k_0} \nabla_\perp^2 - j \sum_{n=2}^{\infty} \left(\frac{k^{(n)}}{n!} \left(-j \frac{\partial}{\partial \tau} \right)^n \right) \right] \tag{3.2}$$

where $\nabla_\perp^2 \equiv \partial^2/\partial x^2 + \partial^2/\partial y^2$ is the transverse Laplace operator and $k^{(n)}$ accounts for the n-th order derivative of the propagation constant. In solid-state lasers both terms should be included while in fiber lasers only the dispersion is considered. k_0 is the wavenumber in vacuum corresponding to the carrier frequency ω_0. $T \equiv \left(1 - (j/\omega_0)\partial_\tau\right)$ is the operator used to correct the diffraction and nonlinear

effects that have frequency dependency. $\hat{N}$ is the operator for intensity-dependent nonlinear effects, divided into two parts:

(1) $\hat{N}_L$: In standard soft-aperture KLM Ti:sapphire lasers, mode-locking is initiated through self-amplitude modulation (SAM) induced by self-focusing that provides more gain to pulses with higher intensity. The nonlinear operator accounting for the optical Kerr effect (first term) and saturated gain (term) from the gain medium is given by:

$$\hat{N}_L = -jTk_o n_2 |A|^2 + g(x,y,z,t) \tag{3.3}$$

where n_2 is the nonlinear refractive index of the medium and spatial gain profile g is given by

$$g(x,y,z,\tau) = \mathbf{IFT}\left\{\frac{\eta_q \alpha}{2}\frac{W_p(x,y,z)/W_{Sat}}{1+\left(W_l(x,y,z)/W_{Sat}\right)}\frac{1}{1+j(\Omega/\Delta\Omega_L)^2}\right\} \tag{3.4}$$

Here **IFT** is the inverse Fourier transform operator, Ω the detuning from the carrier frequency ω_0, α the absorption constant for the pump wavelength in the gain medium, and η_q the quantum efficiency defined as the photon energy ratio between the pump wavelength and the laser central wavelength. $W_{sat}=h\omega_0/(2\pi\sigma_L\tau_l f_{rep})$ is the saturation energy density of the gain medium with a cross-section σ_L and an upper-state lifetime τ_L. $f_{rep}=1/T_R$ denotes the repetition rate of the cavity and $\Delta\Omega_L$ the half-width half-maximum (HWHM) bandwidth of the gain-spectrum. W_p and W_l are the integrated energy density (J/m^2) over one cavity round-trip time of the circulating laser and pump beam.

$$W_p(x,y,z)=\frac{2P_0e^{-\alpha}/f_{rep}}{\pi w_x(z)w_y(z)}\exp\left(-\frac{2x^2}{w_x^{\,2}(z)}-\frac{2y^2}{w_y^{\,2}(z)}\right) \tag{3.5}$$

$$W_l(x,y,z)=\int_{-T_R/2}^{T_R/2}\left|A(x,y,z,t)\right|^2 dt \tag{3.6}$$

(2) $\hat{N}_{MPI}$: In order to extend the model to few-cycle lasers in which much shorter pulses and much higher intracavity intensities (>1TW/cm^2) are usually reached inside the gain medium, additional nonlinear effects related to multiphoton ionization (MPI) are taken into account. These effects add additional loss and defocusing terms that provide feedback to the pulse dynamics in the high-intensity regime. The standard MPI processes are treated with a nonlinear operator that connects to a plasma generation equation given by:

$$\hat{N}_{MPI}=-\frac{\beta^{(K)}}{2}\left|A\right|^{2K-2}-\frac{\sigma}{2}T(1-j\omega_0\tau_c)\rho \tag{3.7}$$

$$\frac{\partial\rho}{\partial t}=\sigma_K\left|A\right|^{2K}(\rho_{at}-\rho)+\frac{\sigma}{n^2U_i}\left|A\right|^2\rho-\frac{\rho}{\tau_{rec}} \tag{3.8}$$

The first term and the second term in eq. (3.7) correspond to multiphoton absorption (MPA) and plasma absorption/defocusing. The first and second terms in eq. (3.8) describe the generation of free electrons through MPI and avalanche ionization processes, respectively. The last term represents recombination of the electrons with a characteristic time. The description of the parameters are given as follows: K is the photon number required to induce band-to-band transitions of electrons in the Ti:sapphire crystal, which is defined as mod(U_i/E_P). U_i is the material bandgap and E_P the

photon energy of the laser. ρ is the plasma density with an upper limit of background atom density ρ_{at}. $\beta^{(K)} = K\hbar\omega_0\sigma_K\rho_{at}$ corresponds to the MPA coefficient proportional to a cross-section σ_K derived from the Keldysh's model. σ is the inverse Bremsstrahlung cross-section that is computed with the reduced electron mass m_e^* in the medium. τ_c represents a average electron collision time and τ_{rec} the electron recombination time.

Based on literature[59–61], the value of abovementioned parameters for the Ti:sapphire crystal are listed in Table 3.1. Figure 3.1 plots the peak plasma density inside the Ti:sapphire crystal generated by a 10fs pulse with an increasing peak intensity from 0.1 to 10 TW/cm^2. For a 5-photon process, the importance of MPA and plasma effects increases with intensity to the power of 4 and 5, correspondingly, while the Kerr effect is only linearly proportional to the intensity. Figure 3.2 compares the nonlinear coefficients for Kerr effect (= $n_0k_0n_2I$), MPA (= $\beta^{(5)}I^4/2$), and plasma effects (=$\sigma I^5\rho/2$). As shown in the plot, both MPA and plasma effects can be omitted for an intensity of <1 TW/cm^2. When the intensity approaches 1 TW/cm^2, the contribution from MPA is no longer negligible as its coefficients is only about one order of magnitude less than the Kerr effect. For a higher intensity (>4 TW/cm^2), the nonlinear coefficients of the plasma and MPA effects exceed the Kerr effect and the pulse enters the filamentation regime.

Parameters (at 800nm)	Value	
n_0	1.76	
n_2	3×10^{-20}	$\mathbf{m^2/W}$
ω_0	2.3562×10^{15}	**rad/s**
η_q	0.6650	
α	450	$\mathbf{m^{-1}}$
σ_L	3×10^{-23}	$\mathbf{m^2}$
τ_L	300	**μs**
U_i	7.3	**eV**
E_p	1.55	**eV**
K	5	
ρ_{at}	11.6×10^{28}	$\mathbf{m^{-3}}$
σ_K	3.45×10^{-73}	$\mathbf{s^{-1}m^{10}W^{-5}}$
$\beta^{(K)}$	4.97×10^{-62}	$\mathbf{m^7W^{-4}}$
σ	1.9×10^{-21}	$\mathbf{m^2}$
m_e^*	0.35	m_e
τ_c	1	**fs**
τ_{rec}	150	**fs**
$\Delta\Omega_L$	3.24×10^{14}	**rad/s**

Table 3.1 Parameters for Ti:sapphire crystals

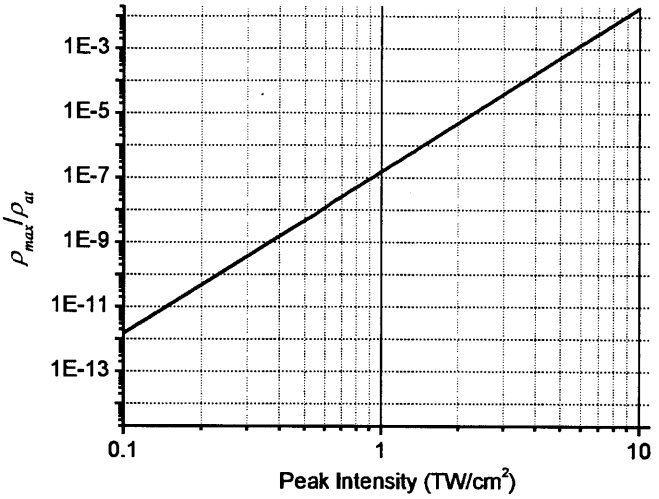

Figure 3.1 Maximum plasma density generated from a 10fs pulse of different peak intensity.

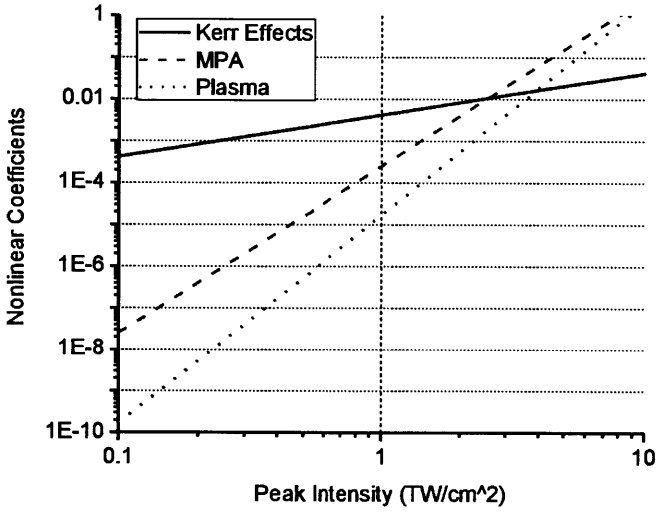

Figure 3.2 Nonlinear coefficients for Kerr effect, MPA, and plasma effects as a function of peak intensity assuming a 10fs pulse.

3.3. Numerical Methods

In order to minimize the computational complexity, a 2+1D simulation is performed by assuming a cylindrically symmetric laser beam (i.e. $x = y = r/\sqrt{2}$).

The GNLSE is solved using the split-step Fourier-Hankel method implemented with a fourth-order Runge-Kutta method in the interaction picture (RK4IP) [62], [63]. The split-step method takes care of the linear propagation operator $\hat{L}$ and nonlinear propagation operator $\hat{N}$ in different steps and the RK4IP is used for achieving an accuracy of $O(h^4)$ in the numerical integration. Since the linear step is often treated in the frequency domain while the nonlinear step is computed in the real domain (time and space), Fourier and Hankel transforms are used to convert the field back and forth between the two domains for time and space, respectively.

3.3.1. Hankel Transform

The Hankel transform (HT) and the inverse Hankel transform (IHT) are typically chosen in the cylindrical coordinates, defined as:

$$\textbf{(HT)} \quad F(v) = 2\pi \int_0^\infty f(r) J_p(2\pi v r) r dr \tag{3.9}$$

$$\textbf{(IHT)} \quad f(r) = 2\pi \int_0^\infty F(v) J_p(2\pi v r) v dv \tag{3.10}$$

where v is the spatial frequency and J_p the p-th order Bessel function of the first kind. In our model, the optical system is assumed to be uniform along the azimuthal axis (i.e. p =0). Unlike Fourier transform using periodic sinusoidal functions as the basis, computation of HT in a discrete system requires special treatment to the grid size in r-axis due to the non-periodic behavior of the Bessel functions. In our model, a quasi-discrete Hankel-Transform (QDHT) proposed by Guizar-Sicaiross [64] is implemented. This method is highly efficient and can be used as the following condition is met:

$$f(r) = 0 \text{ for } r > R \tag{3.11}$$

where R is the maximum physical radius and the size of spatial window used in the simulation. The window is divided into m points which forms a radius vector $\bar{r}$. It should be noted that the elements in $\bar{r}$ are not uniformly distributed but located at the roots of the Bessel function J_0 scaled by R/α_{m+1}:

$$r_i = R\frac{\alpha_i}{\alpha_{m+1}} \quad \textbf{for } 1 \le i \le m \tag{3.12}$$

where α_i is the i-th root of $J_0(x)$. Similarly, the elements of spatial frequency vector $\bar{\nu}$ are defined as:

$$\nu_i = V\frac{\alpha_i}{\alpha_{m+1}} \quad \textbf{for } 1 \le i \le m \tag{3.13}$$

where $V = \alpha_{m+1}/2\pi R$ is the limiting spatial frequency. For efficient numerical computation of the HT and IHT, a $m \times m$ transformation matrix $\mathbf{T}$ and a column vector $\bar{J}$ are prepared.

$$\mathbf{T}_{ij} = \frac{J_0\left(\alpha_i\alpha_j \big/ \alpha_{m+1}\right)}{\left|J_1(\alpha_i)\right|\left|J_1(\alpha_j)\right|\alpha_{m+1}} \quad \textbf{for } 1 \le i, j \le m \tag{3.14}$$

$$J_i = \frac{\left|J_1(\alpha_i)\right|}{R} \quad \textbf{for } 0 \le i \le m \tag{3.15}$$

The HT and IHT can then be easily computed in the following way:

$$\bar{U} = \mathbf{HT}\{\bar{u}\} = \mathbf{T} * [\bar{u} / \bar{J}] \tag{3.16}$$

$$\bar{u} = \mathbf{IHT}\{\bar{U}\} = \mathbf{T} * [\bar{U} / \bar{J}] \tag{3.17}$$

where * denotes matrix multiplication and / denotes element-by-element division.

3.3.2. Linear Step

The linear propagation of the laser beam is numerically computed by integrating the partial differential equation $\partial_z A(r,z,\tau) = \hat{L}A(r,z,\tau)$ along the z-axis where $\hat{L}$ is defined in (3.2). In the split-step method, this step is usually treated in the frequency domain (for both time and space) instead of solving the equation directly in the real space. The frequency-domain field, for both time and space, can be calculated by

$$\tilde{\mathbf{A}}(\nu,z,\Omega) = \mathbf{FT}\{\mathbf{HT}\{A(r,z,\tau\}\} \tag{3.18}$$

The physical meaning is also easier to understand when the beam is viewed as a superposition of many frequency components representing different longitudinal and transverse modes. After an arbitrary propagation distance Δz, a phase shift of $\hat{L}\Delta z$ is added to each mode, i.e.,

$$\tilde{\mathbf{A}}(\nu,z+\Delta z,\Omega) = \exp\left\{ j\left[\left(1+\frac{\Omega}{\omega_0}\right)^{-1}\frac{2\pi^2\nu^2}{n_0 k_0} - \sum_{n=2}^{\infty}\frac{k^{(n)}}{n!}\Omega^n\right]\Delta z\right\}\tilde{\mathbf{A}}(\nu,z,\Omega) \tag{3.19}$$

where the differentiation in $\nabla_\perp^2$ and ∂_τ can be avoided and conveniently replaced by $-4\pi^2\nu^2$ and $j\Omega$. It should be noted that energy is conserved when using eq. (3.19). The operator T is now replaced by a frequency scaling factor $(1+\Omega/\omega_0)^{-1}$ which accounts for the space-time focusing effect.

3.3.3. Nonlinear Step

As mentioned earlier, the nonlinear propagation of a laser beam is usually treated in the real space. Different from the linear operator that has no z dependency, the nonlinear operator acts on the envelope function $A(r,z,\tau)$ while taking $A(r,z,\tau)$ itself as an input parameter. As a result, nonlinear evolution of the pulse must be estimated iteratively by propagating $A(r,z,\tau)$ over many small steps. When the step size is small enough, the nonlinear terms can be considered as perturbations of the pulse.

$$A(r,z+\Delta z,\tau)-A(r,z,\tau)=\Delta z\hat{N}\big(A(r,z,\tau)\big)A(r,z,\tau) \tag{3.20}$$

By assuming that the peak intensity of the pulse does not far exceed 1 TW/cm^2, one can omit the last two terms of eq. (3.8) and calculate the plasma distribution $\rho(r,z,\tau)$ by

$$\rho(r,z,\tau)=\sigma\rho_{at}\int_{-\infty}^{\tau}\left|A(r,z,t)\right|^{2K}dt \tag{3.21}$$

The right-hand side of (3.20) can be decomposed into three terms for Kerr, MPA, and plasma effects:

$$\hat{N}_{Kerr}(r,z,\tau)=-jn_2k_0\Delta z\cdot\mathbf{IFT}\left\{\left(1+\frac{\Omega}{\omega_0}\right)\mathbf{FT}\left\{\left|A(r,z,\tau)\right|^2A(r,z,\tau)\right\}\right\} \tag{3.22}$$

$$\hat{N}_{MPA}(r,z,\tau)=-\frac{\beta^{(K)}\Delta z}{2}\left|A(r,z,\tau)\right|^{2K-2}A(r,z,\tau) \tag{3.23}$$

$$\hat{N}_{plasma}(r,z,\tau)=-\frac{\sigma(1-j\omega_0\tau_c)}{2}\Delta z\cdot\mathbf{IFT}\left\{\left(1+\frac{\Omega}{\omega_0}\right)^{-1}\mathbf{FT}\left\{\rho(r,z,\tau)A(r,z,\tau)\right\}\right\} \tag{3.24}$$

For simulating KLM Ti:sapphire lasers with a pulse duration of > 10fs, one can only consider the Kerr effect. However, in order to simulate sub-10fs lasers, including MPA effects becomes necessary. Although the last term only has contribution when the peak intensity is much higher than 1 TW/cm^2 and can be ignored for most of the time, physically it behaves as a feedback that prevents the beam from collapsing during propagation.

3.3.4. 4th Order Runge-Kutta method in the interaction picture (RK4IP) with Adaptive Step-size Control

Due to the complicated nonlinear processes during the propagation, the evolution of the pulse should be evaluated in a careful way. When solving the NLSE for soliton propagation, the most commonly employed scheme is the simple split-step method which has a second-order accuracy [65]. Although it is possible to implement a higher-order split-step scheme (e.g. Blow and Wood [66]), the global accuracy is still limited to the method used to integrate the nonlinear step. For this reason, Runge-Kutta schemes are used to increase the global accuracy. However, the numerical expense for implementing a high-order Runge-Kutta scheme increases dramatically with the order number. In order to keep the high-order global accuracy while reducing the numerical expense, an optimized Runge-Kutta scheme in the interaction picture (RK4IP) is developed. RK4IP was first proposed to study the Bose-Einstein condensates and have been successfully applied to simulation of highly-nonlinear fiber for supercontinuum generation. In our spatiotemporal model, the RK4IP is employed. The procedure of RK4IP is shown in Figure 3.3 and summarized in the following equations:

$$A_I = \exp(\frac{j\hat{L}\Delta z}{2})A \tag{3.25}$$

$$k_1 = \exp(\frac{j\hat{L}\Delta z}{2})\left[\Delta z\hat{N}(A,z)\right]A \tag{3.26}$$

$$k_2 = \Delta z\hat{N}(A_I + k_1/2, z + \frac{\Delta z}{2})(A_I + k_1/2) \tag{3.27}$$

$$k_3 = \Delta z\hat{N}(A_I + k_{21}/2, z + \frac{\Delta z}{2})(A_I + k_2/2) \tag{3.28}$$

$$k_4 = \Delta z\hat{N}[\exp(\frac{j\hat{L}\Delta z}{2})(A_I + k_3), z + \Delta z](\exp(\frac{j\hat{L}\Delta z}{2})(A_I + k_3)) \tag{3.29}$$

$$A(r, z + \Delta z, \tau) = \exp(\frac{j\hat{L}\Delta z}{2})(A_I + k_1/6 + k_2/3 + k_4/3) + k_4/6 \tag{3.30}$$

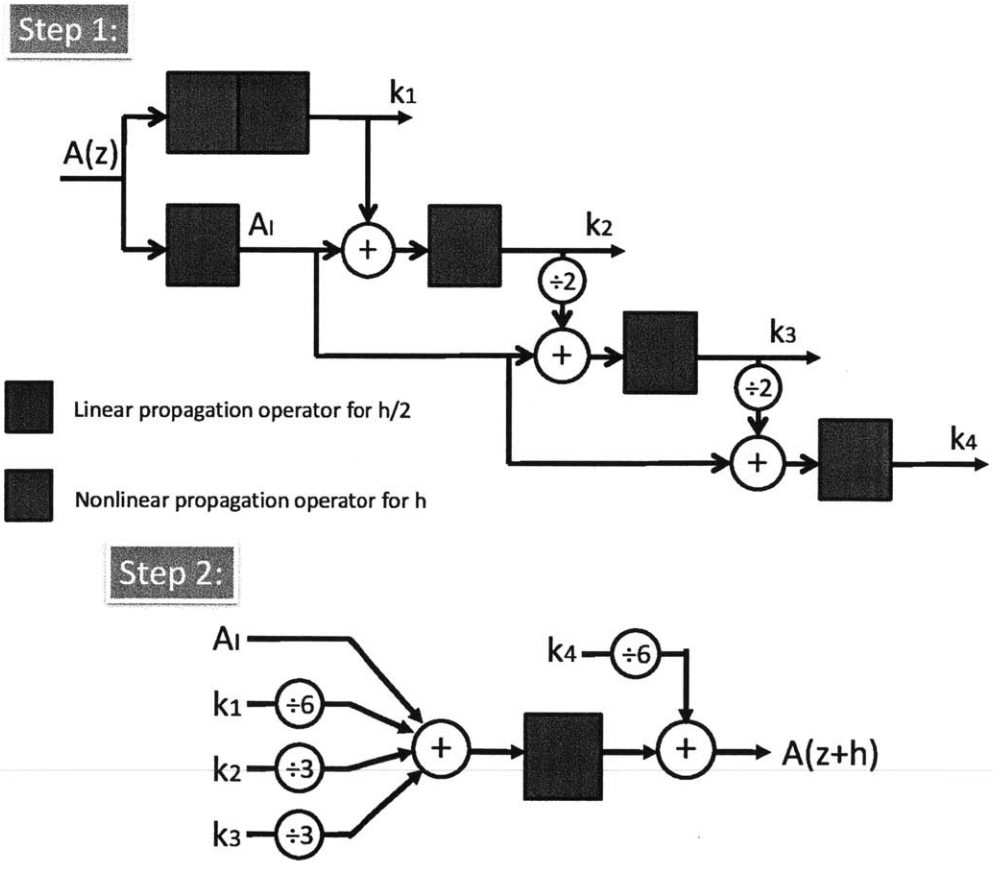

Figure 3.3 Numerical procedure of RK4IP

The RK4IP scheme has a global error of $O(h^4)$, which means the accuracy of the simulation can be significantly increased by reducing the step size h. However, choosing a too small step size also slows down the simulation. In order to choose an optimal step size, we implemented an adaptive step-size control method similar to the one reported in Ref. [67]. In this approach, two fine evaluation with $h=\Delta z/2$ and one coarse evaluation with $h=\Delta z$ are made separately to propagate the beam from z to $z+\Delta z$, as shown in Figure 3.4.

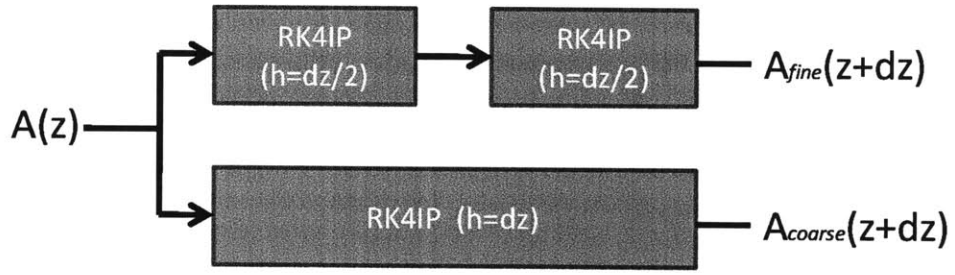

Figure 3.4 Concept of adaptive step-size control

When the solutions with fine and coarse steps are found, one can calculate the local error δ by

$$\delta = \frac{\left\| A_{fine} - A_{coarse} \right\|}{\left\| A_{fine} \right\|} \tag{3.31}$$

The goal of adaptive step size control is to maintain a local error within a reasonable range of (δ_{LB}, δ_{UB}) where δ_{LB} and δ_{UB} are the lower-bound and upper-bound of the acceptable error. If $\delta > \delta_{UB}$, the solution is discarded and the step is repeated with the step size h multiplied by 2/3. If $\delta < \delta_{LB}$, the solution is kept and the step size h is divided by 2/3 for the next step. If δ is within the range, then the result obtained from fine steps is used since it is closer to the exact solution. The

algorithm used here is a simplified version from the one in the original paper which adjusts the step size in almost every step. The reason is that in spatiotemporal models the size of the dispersion and diffraction matrices are often huge and they need to be recalculated when the step size is adjusted might significantly increase the computation time, if the step size is changed too often.

3.4. Efficient Round-trip Cavity Model

In each round-trip, the pulse experiences nonlinear evolution when passing through the gain or Kerr medium, which dynamically reshapes its spatial and temporal profile. For the rest of the path, the pulse experiences linear propagation according to the spatial arrangement as well as the dispersion of the intracavity components. However, since the pulse diverges very quickly after leaving the crystal, a large spatial window would be required for the simulation. To circumvent this problem, an equivalent optical system with two effective lenses attached to the front and back of the crystal and separated by an effective distance can be found. This ensures that the maximum spot size outside the crystal will not exceed that inside the crystal. As an example, Figure 3.5 shows the schematic of a typical cavity path outside the crystal and the corresponding equivalent system. To find the equivalent system, an overall ABCD matrix describing all the components in the real path is calculated. The beginning and ending reference planes are both chosen inside the crystal. n_r is the refractive index ratio between crystal and free space; θ_1 and θ_4 are the Brewster's angle of the interfaces; θ_2 and θ_3 are the incident angles on the focusing mirrors used for astigmatism compensation. With these parameters, the

ABCD matrices corresponding to each individual component can be obtained using Table 3.2 and used to compute the overall ABCD matrix:

$$\begin{pmatrix} A & B \\ C & D \end{pmatrix} = M_B(\theta_4, n_r^{-1}) * M_A(D_3) * M_C(\theta_3, 2f_2) * M_A(D_2) * M_C(\theta_2, 2f_1) * M_A(D_1) * M_B(\theta_1, n_r) \tag{3.32}$$

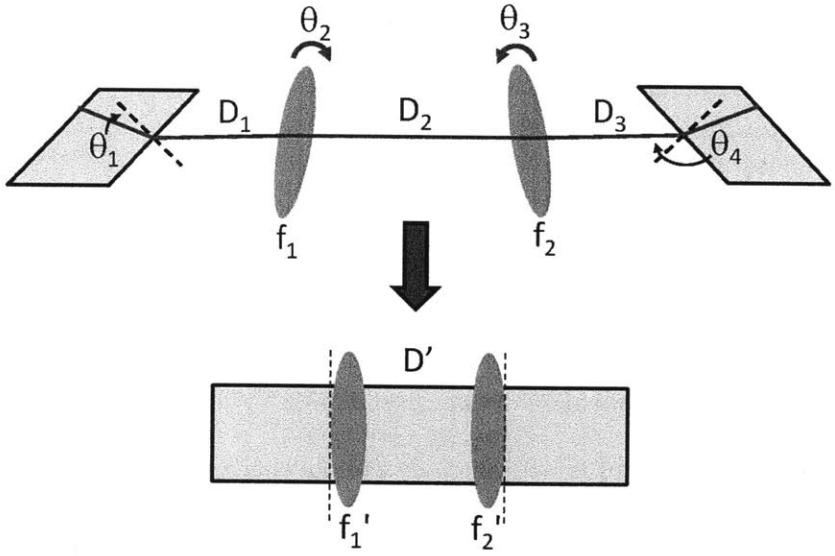

Figure 3.5 Schematic of a typical unfolded cavity path (top) and its equivalent system (bottom) for efficient simulation of the beam propagation outside the crystal.

Once the overall matrix is found, the focal length ($f_1'f_2'$) and spacing D' of the two effective lenses in the equivalent system can be calculated by

$$D' = B \tag{3.33}$$

$$f_1' = \frac{B}{1-A} \tag{3.34}$$

$$f_2' = \frac{B}{1-D} \tag{3.35}$$

Element	Sagittal M^S	Tangential M^T
Propagation in a medium with constant n $M_A(d)$	$\begin{pmatrix} 1 & d \\ 0 & 1 \end{pmatrix}$	
Refraction at a curved interface $M_B(\theta_i, n_r)$	$\begin{pmatrix} 1 & 0 \\ 0 & 1/n_r \end{pmatrix}$	$\begin{pmatrix} \frac{\sqrt{n_r^2 - \sin^2\theta_i}}{n_r \cos\theta_i} & 0 \\ 0 & \frac{\cos\theta_i}{\sqrt{n_r^2 - \sin^2\theta_i}} \end{pmatrix}$
Reflection at a curved interface $M_C(\theta_i, R)$	$\begin{pmatrix} 1 & 0 \\ -2/R\cos\theta_i & 1 \end{pmatrix}$	$\begin{pmatrix} 1 & 0 \\ -2\cos\theta_i/R & 1 \end{pmatrix}$

Table 3.2 Same as Table 2.1 with $M_B(\theta_i, n_r, R)$ reduced to $M_B(\theta_i, n_r)$ for a flat interface.

With the equivalent system, one can easily propagate the beam around the cavity with a series of transformations without changing the simulation window:

$$\mathbf{A}_{i+1}(r,\Omega)\big|_{z=0} = \mathbf{D} \otimes \mathbf{F}_2 \otimes \mathbf{IHT}\left\{\mathbf{L} \otimes \mathbf{HT}\left\{\mathbf{F}_1 \otimes \mathbf{A}_i(r,\Omega)\big|_{z=L}\right\}\right\} \tag{3.36}$$

where $\mathbf{F}_{1,2}$ are the matrices for the lens transformation; $\mathbf{L}$ is the matrix for propagating a distance of D'; $\mathbf{D}$ is the matrix for overall cavity dispersion excluding the crystal. These matrices can be pre-calculated using the following formulas:

$$\mathbf{F}_{1,2}(r,\Omega) = \exp\left[j\left(1+\frac{\Omega}{\omega_0}\right)\frac{n_0 k_0 r^2}{2f_{1,2}'}\right] \tag{3.37}$$

$$\mathbf{L}(\nu,\Omega) = \exp\left[j\left(1+\frac{\Omega}{\omega_0}\right)^{-1}\frac{2\pi^2\nu^2}{n_0 k_0}D'\right] \tag{3.38}$$

$$\mathbf{D}(r,\Omega) = \exp\left[-j\sum_{n=2}^{\infty}\frac{k_{all}^{(n)}}{n!}\Omega^n\right] \tag{3.39}$$

In both ring and linear cavity lasers, the same approach can be applied to the linear propagation section for the round-trip. The only difference is that in linear cavities two separate sets of transformation matrices for propagating the beam in each of the two arms should be prepared.

Although it is possible to avoid using a large spatial window during the free space propagation with the above method, there is still a theoretical limit due to the finite resolution of the spatial grid. Since the focal lengths of the effective lenses are usually very small, the phase difference between two adjacent radial points might become too large to be resolved as r increases. To find a range of r that has no aliasing effect, one can use the following condition (assuming Δr is the spatial grid size):

$$\frac{2\pi}{\lambda}\frac{n_0}{2|f|}\left[r^2-(r-\Delta r)^2\right]<\pi \tag{3.40}$$

By using the approximation that $\Delta r<<r$, the following condition can be found

$$r<\frac{\lambda|f|}{2\Delta r n_0} \tag{3.41}$$

After a rearrangement of eq. (3.41) using $N = R/\Delta r$, another useful criterion can be derived for determining the required number of spatial grid points for running a simulation with a spatial window size R

$$N>\frac{2n_0R^2}{\lambda|f|} \tag{3.42}$$

3.5. Simulation Results and Discussions

3.5.1. GPU accelerated computing

The spatiotemporal model is implemented in MATLAB® accelerated by GPU computation techniques using the Jacket® platform. The simulations are performed on a machine equipped with two Intel® Xeon 5680 (6 cores, 12 threads) CPU processors, two nVidia® Tesla C2070 GPU cards with 6 GB of onboard memory on each card, and 96 GB of RAM. With the GPU as a backend computation engine, Jacket® boosts the computational speed by parallelizing many time-consuming operations such as matrix multiplication and FFTs while maintaining the user-friendliness of the MATLAB programming. To give an idea of the computing power of a GPU for large matrices, I compare three types of operations including simple matrix addition, matrix multiplication, and FFTs with a 1024x1024 matrix using GPU and CPU. As shown in Table 3.3, computation using GPU enables significant speedup comparing to the traditional CPU computing. Even though computation on GPU is extremely fast, the memory available on the GPU is limited. As a result, data transmission between CPUs and GPUs often becomes the bottleneck in the simulation. Avoiding unnecessary data transmission is an important issue in optimization of the program.

Operations	GPU nVidia C2070	CPU (2x) Intel Xeon 5680	Speedup
Addition	33 μs	6 ms	182 ×
Matrix Multiplication	18 ms	146 ms	8 ×
1D-FFT	870 μs	14.7 ms	17 ×
2D-FFT	1.4 ms	22.3 ms	16 ×

Table 3.3 Comparison of computational speed using GPU and CPU

3.5.2. Cavity Setup

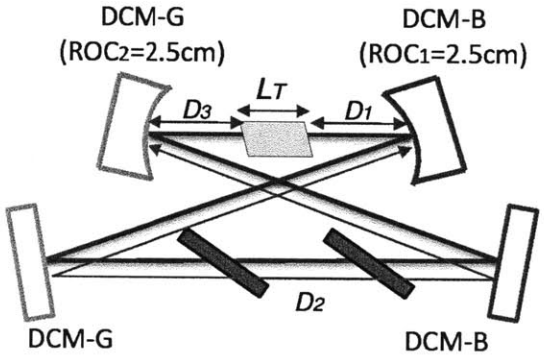

Figure 3.6 Setup of a 2GHz four-mirror ring cavity Ti:sapphire laser used for simulations and experiments.

The numerical model is tested on a four-mirror ring cavity similar to the 2GHz laser discussed in Chapter 2. As shown in Figure 3.6, the cavity consists of one pair of flat mirrors and one pair of curved mirrors with a radius of curvature of 2.5cm. The curved mirrors are tilted to compensate the astigmatism introduced by the crystal that is placed at Brewster angle to minimize reflection loss. The path length inside the crystal L_T is 2mm. The length D_2 is set to 12cm for a ~ 2GHz cavity. In order to precisely control the size and the relative position of the cw laser mode and

pump laser mode inside the crystal, we numerically adjust the position and the angle of the curved mirrors based on the analysis of cavity stability region performed in Figure 2.17. In the experiments, the dispersion of the crystal is usually overcompensated by the ultra-broadband double-chirped mirrors and then adjusted by inserting additional dispersion compensating wedges made of, for example, BaF_2 or fused silica. To simplify the numerical study and explain the spatiotemporal mode-locking dynamics, we first test an ideal cavity with a constant loss and zero cavity dispersion for all wavelengths. The dependence of important cavity parameters will be studied. Finally, the reflectivity and dispersion from the DCMs as well as the output coupler calculated from the real mirror designs will be used to simulate the practical cavity. In our simulation, we use a 300 × 1024 matrix to describe the field with a spatial and time resolution of 0.5 μm and 1.2 fs, respectively.

3.5.3. Mode-locking Dynamics

To check if the laser cavity can support a stable pulse, we calculate the local error between round-trips using the following formula

$$\varepsilon_A = \frac{\left\| |A_{i+1}(\omega,r)| - |A_i(\omega,r)| \right\|}{\left\| A_i(\omega,r) \right\|} \tag{3.43}$$

The error converges to zero when the pulse approaches the steady state. Theoretically, the mode-locking starts from mode beating, which generates temporal spikes and induces the self-amplitude modulation. To simulate this phenomenon, a long initial pulse is used to trigger the mode-locking. As the very first test of the model and a reference point of operation used for later comparisons,

we create an ideal dispersion-less cavity by assuming that the crystal dispersion is cancelled by all the dispersion compensating components (e.g. mirrors and materials other than the crystal). The round-trip loss of the cavity is set at 7% for all the wavelengths. The path length of the crystal L_T is 2 mm. The cavity is numerically aligned to support a fundamental transverse mode with a beam waist at the center of the crystal and a FWHM spot size of 23 μm (in tangential plane). The pump beam is also focused onto the same location with a FWHM spot size of 10 μm. The mode-locking dynamics is excited with a 5nJ, 100fs initial Gaussian pulse and a pump power of 7 Watt. Round-trip iterations repeat until the local error converges and reaches 10^{-4}.

The temporal profile of the pulse and its evolution when passing through the crystal and from the initial to the steady-state are shown in Figure 3.7. In the early stage (0 – 100 passes) of the evolution, along with the growth of the pulse energy, more spectral components are generated due to self-phase modulation. Later (100 – 250 passes), the spectrally broadened pulse is compressed by the cavity components outside the crystal and becomes a shorter pulse with higher peak intensity. Finally (250 passes to steady state), a few-cycle pulse forms with its profile gradually smoothened and cleaned.

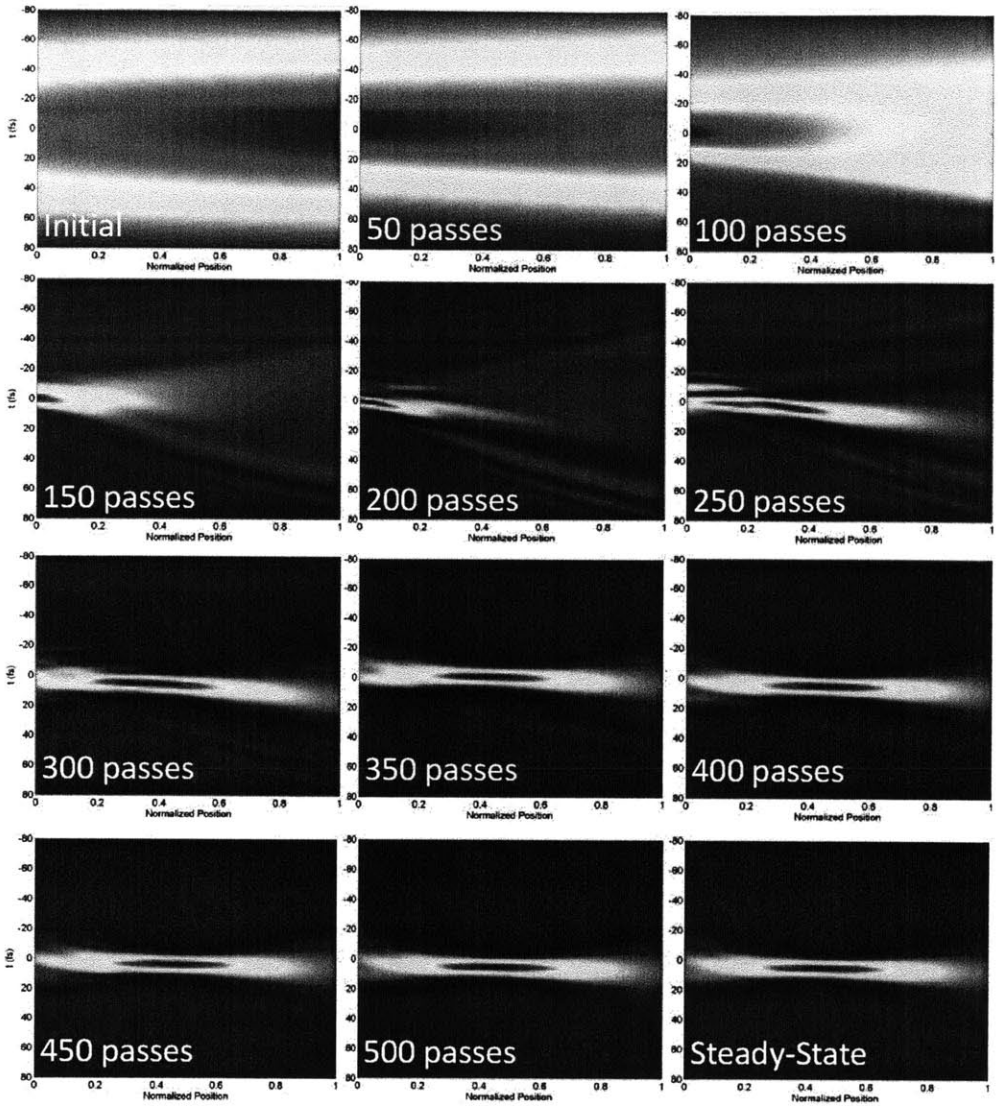

Figure 3.7 The temporal evolution of the pulse inside the crystal for every 50 round-trips from initial to steady state.

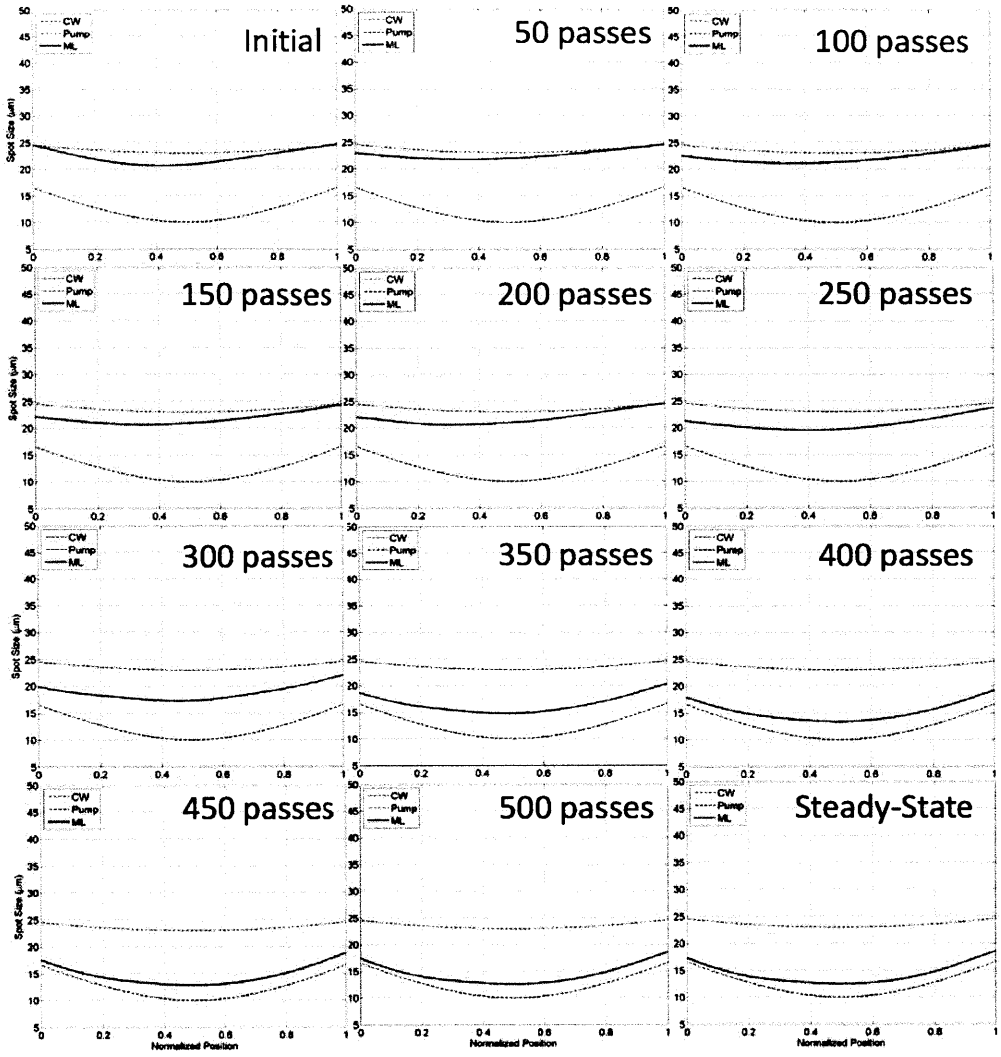

Figure 3.8 The evolution of laser spot size and its overlap with the pump beam inside the crystal for every 50 round-trips from initial to steady state.

The main pulse-shaping mechanism in soft-aperture KLM lasers is the intensity-dependent overlap between the laser and pump beam, as shown in Figure 3.8. In the early stage when the pulse is still long and its intensity is weak, the spot size of the laser beam is not too different from that in a cold cavity. However, as the energy and the peak intensity grow, the interplay between gain-guiding, diffraction, and self-focusing effects triggers the oscillation in the laser beam size. Meanwhile, the main pulse shapes itself by radiating energy in the time domain (see passes

150 – 250 in Figure 3.7). Since the radiated pulse transients have a lower intensity, they do not experience the same amount of nonlinear phase and therefore diverge at different rate as the main pulse. As a result, the main pulse and the transients will overlap with the pump beam differently in the following round-trips. If the cavity is properly aligned such that the high-intensity main pulse is favored, pulse transients will die out eventually and a clean, stable short pulses will build up. The steady-state pulse spectrum is shown in Figure 3.9, corresponding to a transform-limited pulse of 6.17fs.

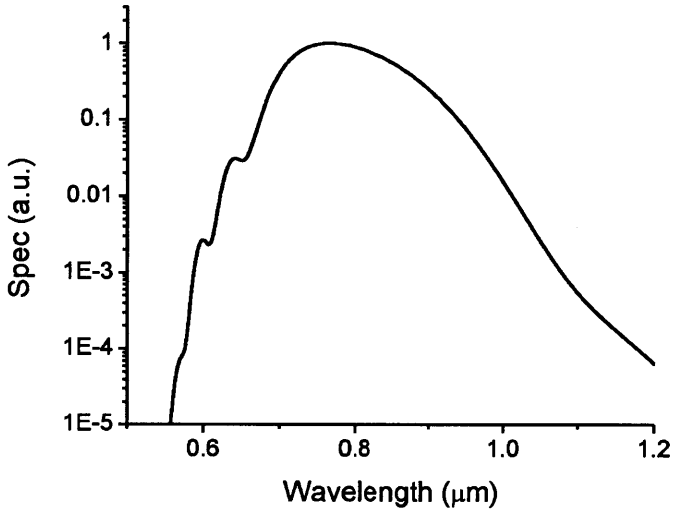

Figure 3.9 The steady-state pulse spectrum for an ideal dispersionless laser cavity. The transform-limited pulse duration is 6.17fs

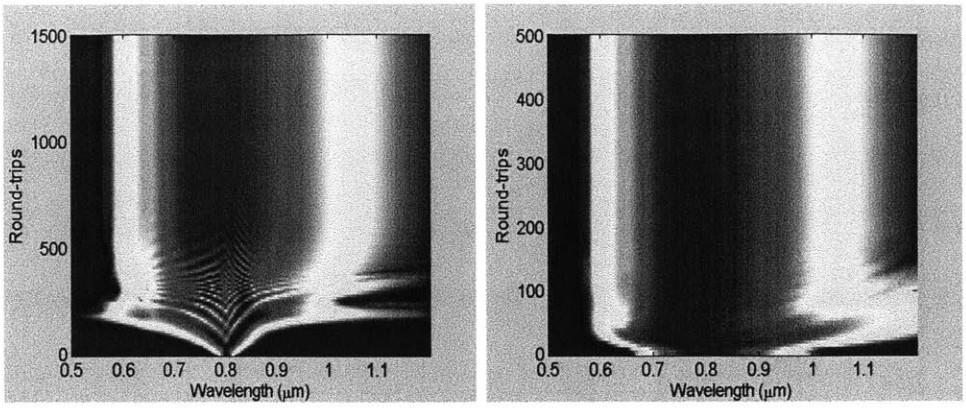

Figure 3.10 Spectral evolution (log scale) of the intracavity pulse vs. number of round-trips. The figures are obtained with an initial pulse of (left) 100fs and (right) 10fs.

Figure 3.10 shows the evolution of the pulse spectrum with number of round-trips performed using a 100fs (left) and 10fs (right) initial pulse. As discussed above and shown in the 100fs plot, the pulse spectrum is first broadened, reshaped, and finally smoothened out. The pulse converges to its steady state in about 1500 round-trips. As a comparison, we repeat the simulation using the same laser parameters but with a 10fs initial duration. Not surprisingly, the same results are found as shown in the figure, which verifies that the steady-state solution is unique and independent of the initial pulse chosen. However, when an initial pulse that is closer to the steady-state solution is used, one can save a significant amount of simulation time. Figure 3.11 compares the local error for both cases. In the 100fs case, the pulse transients cause an increase in the local error during the first 400 round-trips. Once the pulse transients die, the error converges linearly. In the 10fs case, the local error converges quickly down to 10^{-3} in 200 round-trips while the 100fs takes about 1100 round-trips.

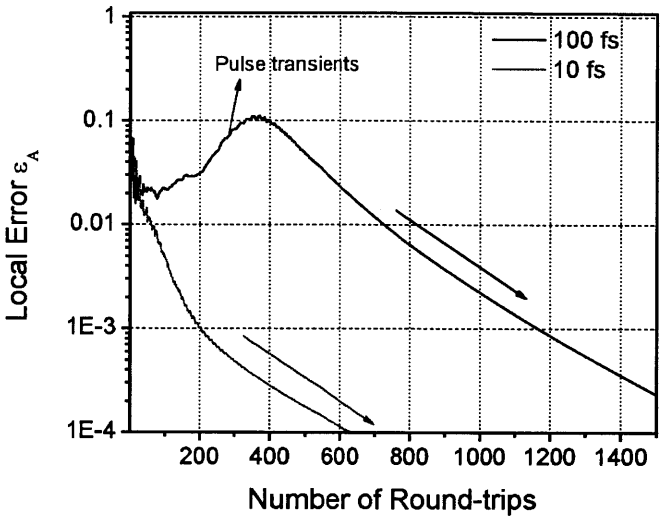

Figure 3.11 Comparison of local error convergence using a long (100fs) and a short (10fs) initial pulse. Once the pulse transients die, the error converges linearly.

3.5.4. Operating Point vs. Laser Performance

Finding an operating point with a large Kerr sensitivity is an important issue in the construction of KLM lasers. Even though the results from a pure temporal laser model have shown that octave-spanning spectra can be generated with some saturable absorption effect and careful dispersion management, the model fails to figure out the strength of the effective saturable absorption and its connection to the cavity alignment. To study the dependence of laser performance on the operating point, the spatiotemporal model must be employed. In this section, 6 different operating points on the shorter edge of the stability region with a cw waist size from 20~25 μm (see Figure 3.12) are simulated.

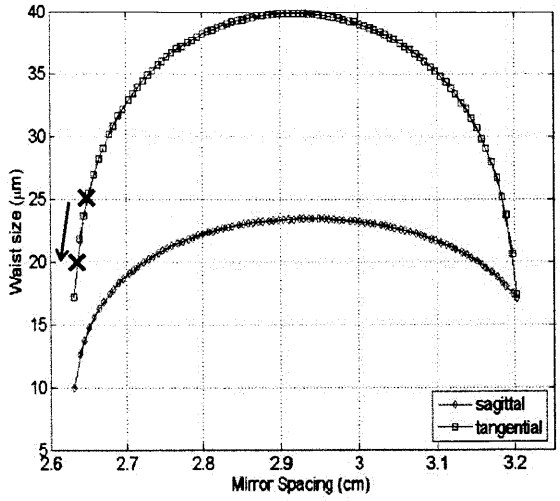

Figure 3.12 Region of stability of the simulated laser cavity. The laser is operated at the edge of shorter mirror spacing with a waist size of 20~25 μm.

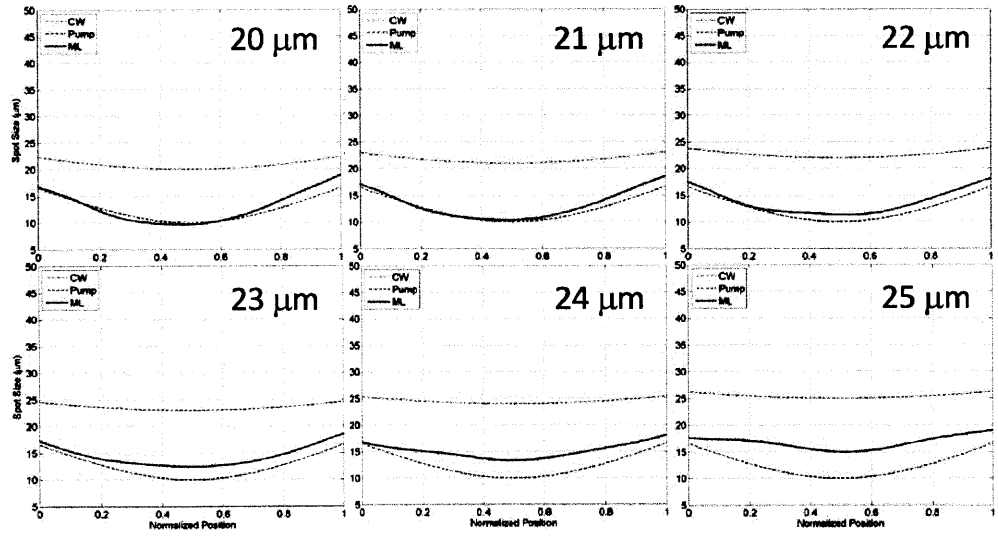

Figure 3.13 The steady-state laser spot size and its overlap with the pump beam inside the crystal as a function of cw laser waist size from 20 ~ 25 μm.

In this set of experiment, same waist size and power for the pump beam are used as the previous setup. Figure 3.13 shows the steady-state laser spot size and its overlap with the pump beam for all the cases. It can be clearly seen that the laser beam is focused to a smaller spot when the laser operating point is closer to the

edge of the stability region. As shown in Figure 3.14, the peak intensity of the pulse is the highest near the center of the crystal. The maximum pulse intensity could be as high as >1 TW/cm^2 for the 20μm case and as low as <0.5 TW/cm^2 for the 25μm case. As a result, the spectrum is broader (see. Figure 3.15) due to stronger SPM when an operating point closer to the edge of stability region is used.

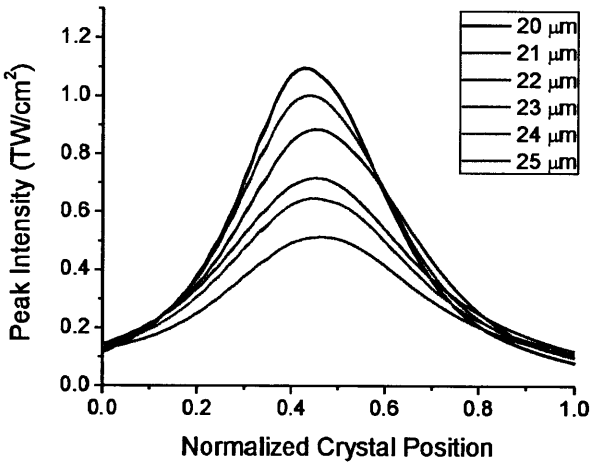

Figure 3.14 Peak intensity of the pulse inside the laser crystal.

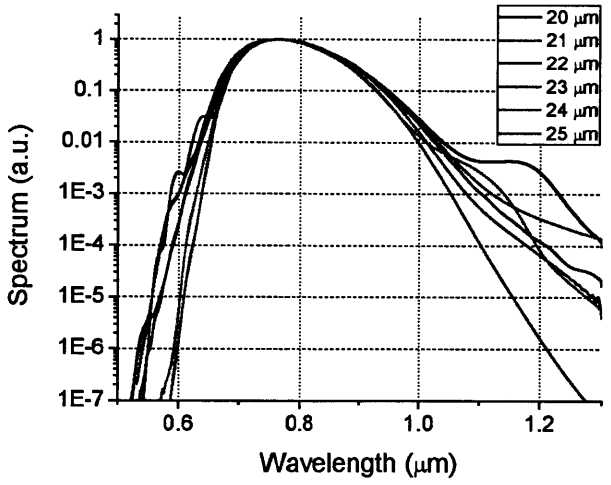

Figure 3.15 Intracavity spectrum of the steady-state pulse with different operating points of the laser.

The strength of SPM can be roughly estimated by the nonlinear phase accumulated along the nonlinear medium. This is calculated by finding the difference between the round-trip phase of the steady-state pulse and the total Gouy phase shift in a cold cavity. Figure 3.16 plots the accumulated nonlinear phase at different operating points for 7W, 8W, and 9W of pump power. With a higher pump power, the nonlinear phase becomes larger since the pulse energy also increases. However, the laser might enter an unstable zone if the beam is too tightly focused.

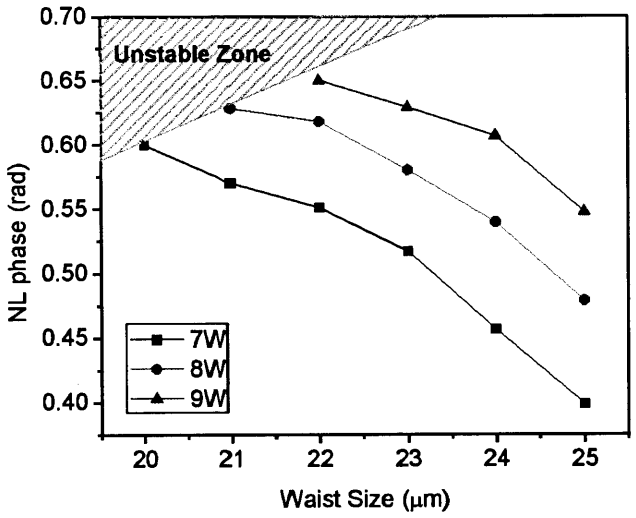

Figure 3.16 Accumulated nonlinear phase vs. operating point at different pumping powers.

The limiting factor behind the instability is the maximum intensity of the pulse inside the crystal. As shown in Figure 3.17, the estimated intensity threshold for the unstable zone is ~1.1 TW/cm^2. This is also the level where a significant MPA effect is induced. Theoretically, the KLM Ti:sapphire laser is considered as a dispersion-managed soliton that maintains its shape by the interplay of SPM and dispersion. However, when the intensity is too high, MPA effect occurs and

introduces instability to the pulse by absorbing the energy from the pulse peak. This process effectively causes energy radiation from the soliton to a dispersive transient wave. In order to stay in a stable mode-locking state, much stronger SAM must be provided. Since the MPA effect is highly nonlinear, the demand for SAM also increases exponentially. As a result, stable mode-locking can hardly be found once the pulse enters the MPA regime.

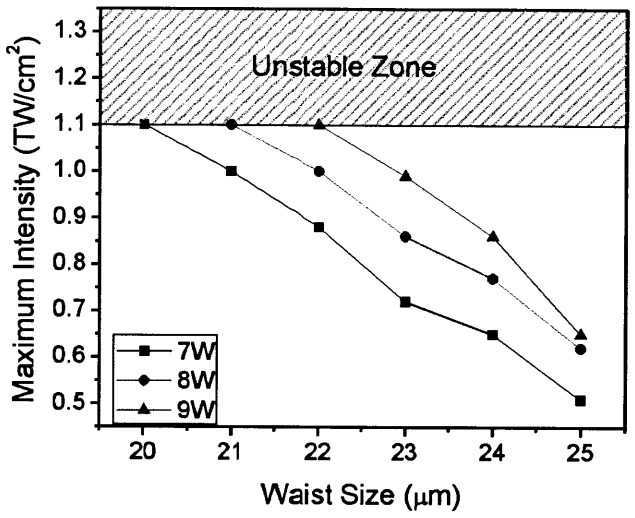

Figure 3.17 Maximum intensity vs. operating point at different pumping powers.

Figure 3.18 shows the calculated intracavity pulse energy at the operating point of interest with different pump powers. The pulse energy decreases when a smaller cw laser waist is used for a fixed pump power, which agrees with our experimental observations. The result suggests that in order to maximize the output power from a few-cycle laser, a large cw laser beam waist should be used. Ideally, one can still acquire similar amount of nonlinear phase by increasing the pump power. Practically, the beam distortion caused by the thermal lensing effect might become a serious problem when the pump power is too high. Finally, Figure 3.19

plots the local round-trip errors of the 6 operating points at a pump power of 8W. The pulse transients live longer when a smaller cw laser beam waist is used. For the 20 μm case, there is no sign of convergence after 3500 round-trips.

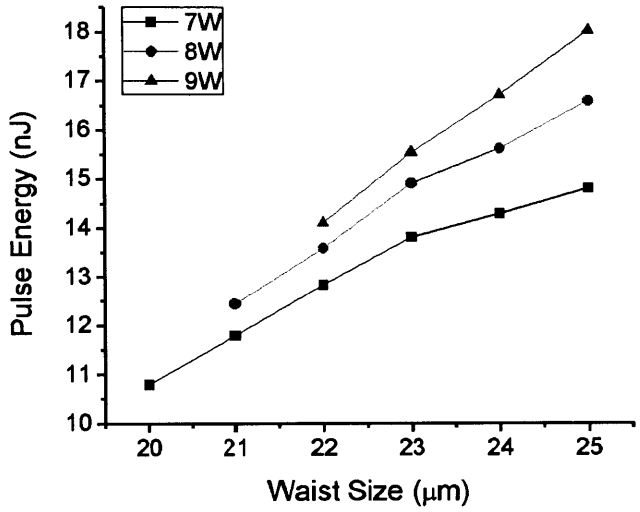

Figure 3.18 Intracavity pulse energy vs. operating point at different pumping powers.

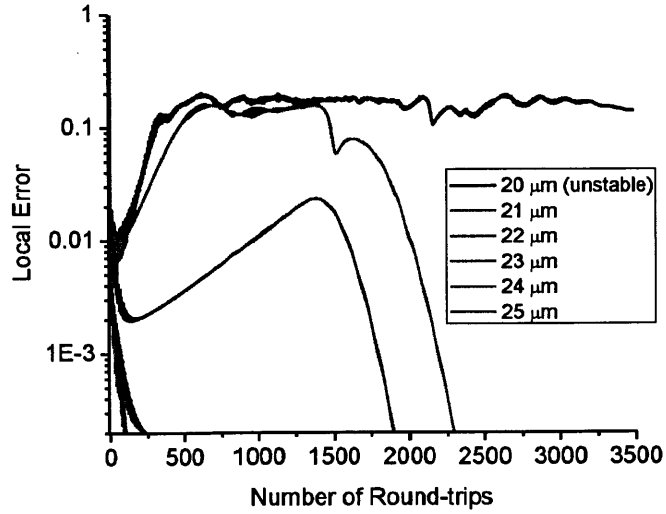

Figure 3.19 Convergence of local error for different operating points with a pump power of 8W.

3.5.5. Cavity Dispersion

In this section, the influence of cavity dispersion on the laser performance is studied. The dispersionless cavity (7W pump power, 23 μm waist size) analyzed in the beginning of this section is also used here as a reference point for comparison. We first compare the laser output spectrum with a net cavity GDD of -10, -5, -2 , 0, and 2 fs^2 and no high-order dispersion. Figure 3.20 and Figure 3.21 shows the simulated transform-limited pulse width and intracavity pulse energy supported by the cavity.

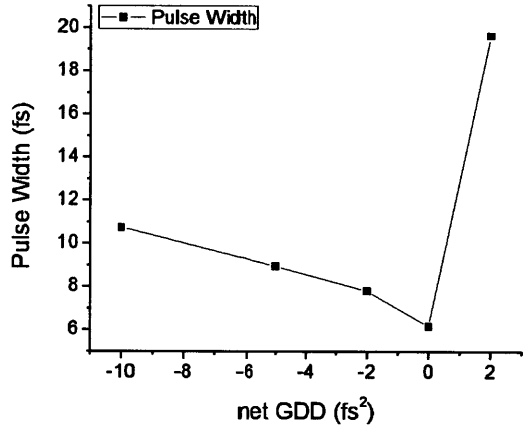

Figure 3.20 Transform-limited pulse width vs. net cavity GDD

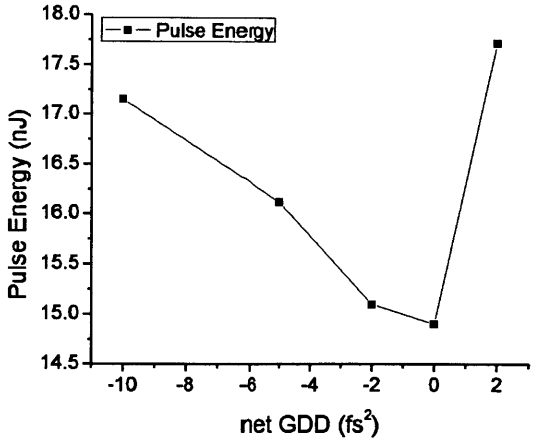

Figure 3.21 Simulated intracavity pulse energy vs. net cavity GDD

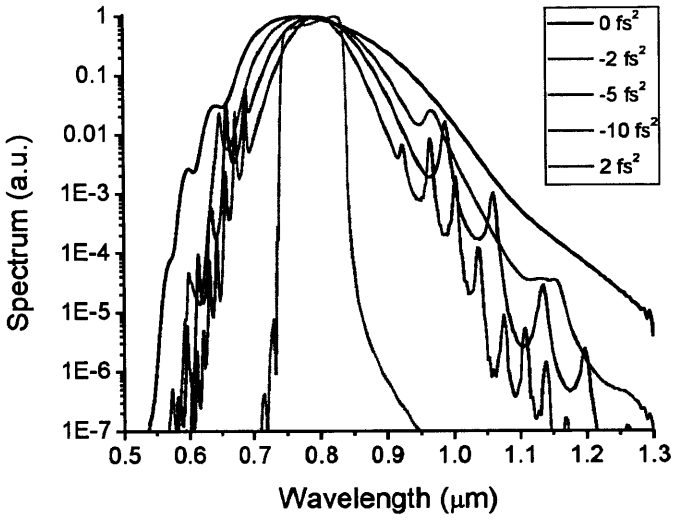

Figure 3.22 Simulated intracavity laser spectrum vs. net cavity GDD

As shown in Figure 3.22, the spectrum is broader as the net cavity GDD is approaching from a negative value to 0. When the GDD becomes positive, a flat-top spectrum is formed with two steep edges. These phenomena agree with the theory of dispersion-managed soliton mode-locking. However, the existing theory was not able to accurately explain the physical origin of the spectral peaks that are often seen on both sides of the spectrum as shown in the simulation. When the net GDD is closer to zero, the peaks become less dense. In the past, researchers used to attribute these peaks to phase-matching resonances, but unfortunately the phase-matching condition was not yet found. In facts, these spectral features often come with highly-structured beam profiles. As an example, Figure 3.23 shows the simulated laser beam profile as a function of wavelength from a cavity with a net GDD of 0, -2, -5, and -10 fs^2.

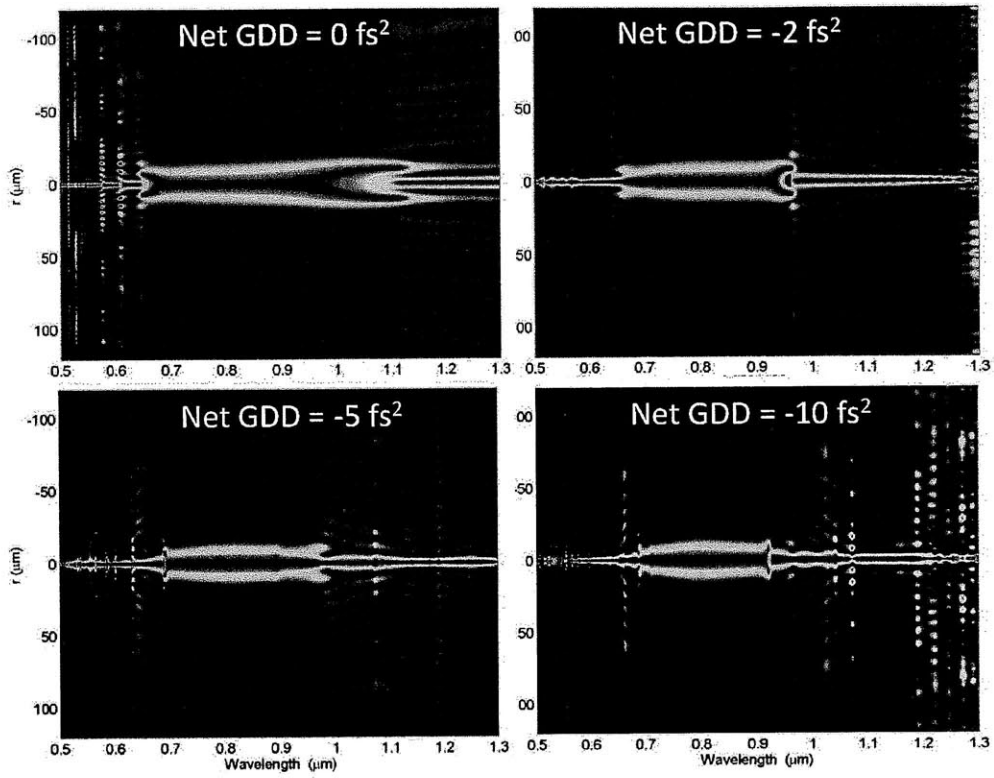

Figure 3.23 Wavelength-dependent beam profile of a mode-locked beam from a cavity with a net GDD of 0, -2, -5, and -10 fs^2.

The influence of third-order dispersion (TOD) on the laser spectrum is also simulated. Figure 3.24 compares the spectra generated from a cavity with zero GDD and a net cavity TOD of 2, 0, and -2 fs^3. It can be observed that the presence of TOD skews the laser spectrum. For a negative TOD, the peak wavelength shifts to the short wavelength side; for a positive TOD, the peak wavelength shifts towards the long wavelength side. Although the spectral peaks are still found in both cases, the wavelength-dependent beam profile in Figure 3.25 shows very different mode structures on both sides of the spectrum depending on the sign of the applied TOD.

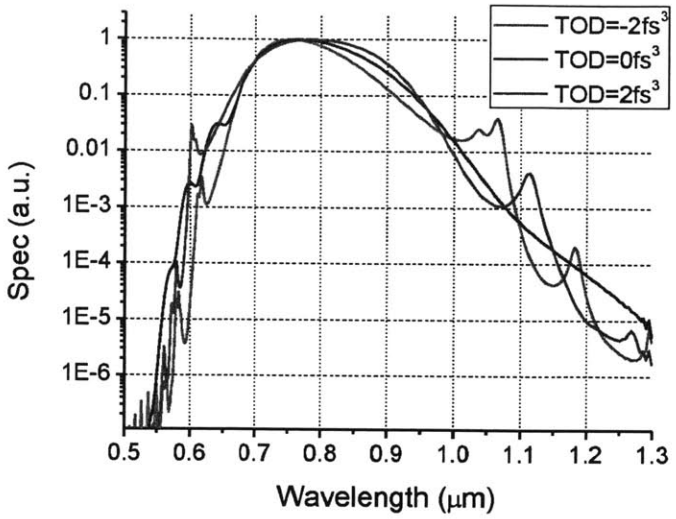

Figure 3.24 Simulated intracavity laser spectrum for net cavity TOD of -2, 0 and 2 fs^3. The net cavity GDD is set to 0 fs^2.

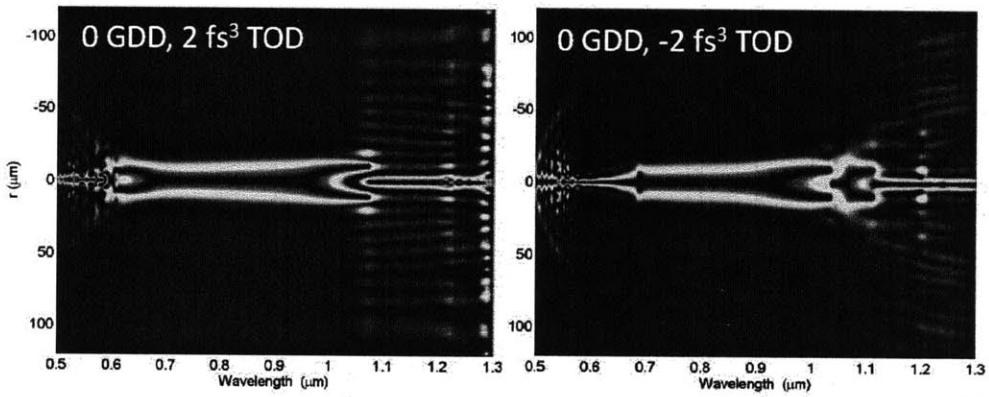

Figure 3.25 Wavelength-dependent beam profile of a mode-locked beam from a cavity with a net TOD of 2 and -2 fs^3.

3.5.6. Wavelength-dependent Beam Profile and Resonant Condition

As discussed earlier, the output beam produced from an ultra-broadband laser strongly depends on wavelength and is also affected by the cavity dispersion. Figure 3.26 shows the typical beam profile measured from an octave-spanning, Ti:sapphire ring cavity laser. Experimentally, the mode is found to be less

structured if it is in the wavelength range where the cavity loss and dispersion are small (e.g. λ ~ 700-900 nm). For the wavelength region with a higher output coupling/loss or a larger dispersion (λ ~ 600-700 nm and 900-1100 nm), higher-order spatial modes are observed. For the region where the cavity is extremely lossy (λ < 600 nm and > 1100 nm), the mode structure is determined by the single-pass nonlinear effects inside the crystal. In this region, a typical ring structure appears.

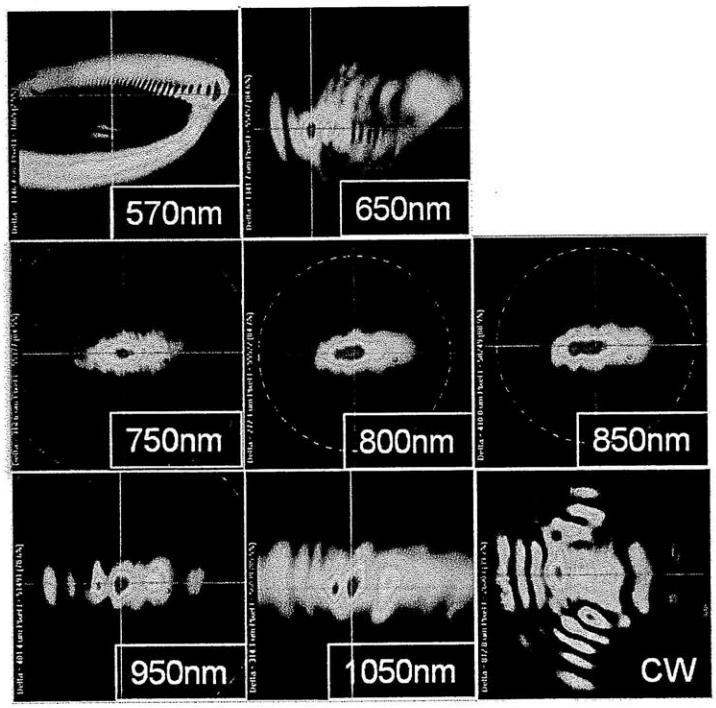

Figure 3.26 Measured beam profile at different wavelengths from a DCM-based ring cavity Ti:sapphire laser

To analyze these mode structures and find the connection to the laser spectrum, we numerically setup a laser cavity using the dispersion and reflectivity calculated from the real mirror designs used in the experiment [36], [68]. The cavity is operated at a nearly dispersion-free point by carefully adjusting the

thickness of the BaF_2 and fused silica in the cavity. The overall round-trip phase from the cavity dispersion is shown in Figure 3.27.

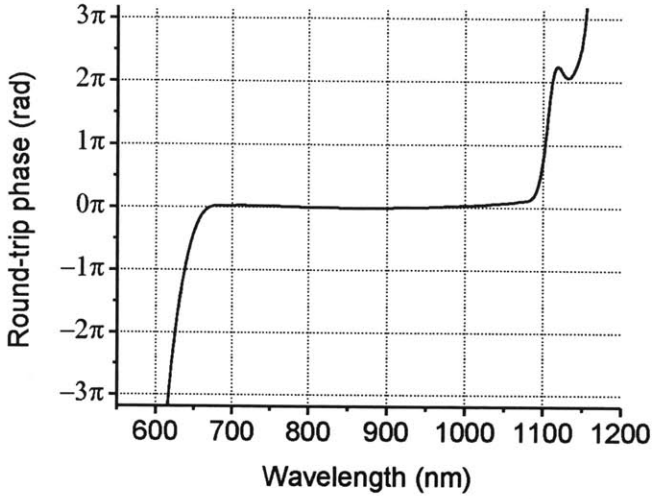

Figure 3.27 Cavity round-trip phase from dispersion

Similar features as in the experiment can be observed from the simulated beam profile shown in Figure 3.28.

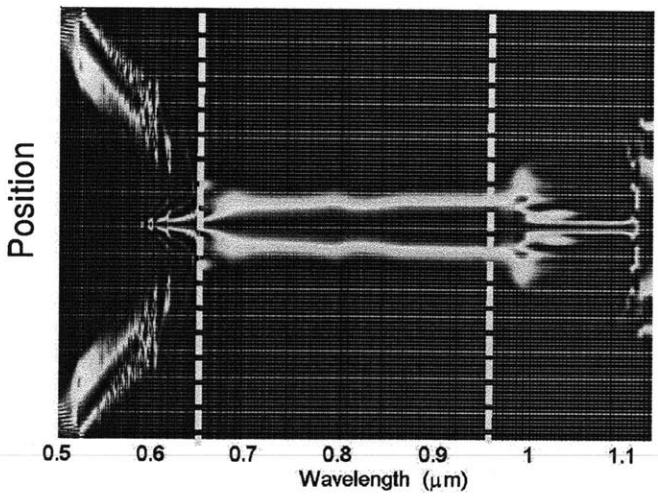

Figure 3.28 Simulated wavelength-dependent spatial beam profile of the laser beam from a DCM-based ring cavity Ti:sapphire laser

Figure 3.29 compares the measured and simulated output spectrum of the same laser. As shown in the plot, both spectra share a common feature of multiple spectral peaks near 650nm and 1100nm.

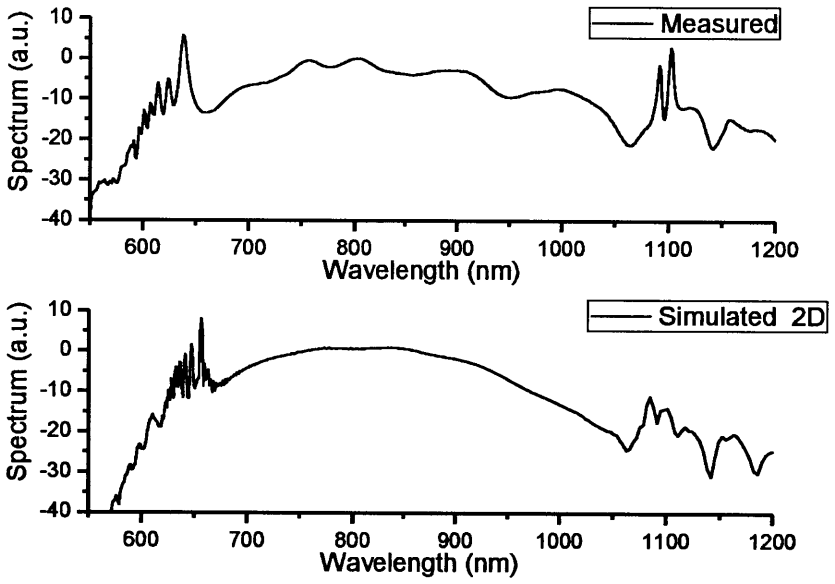

Figure 3.29 Comparison of measured and simulated spectra from a DCM-based ring cavity Ti:sapphire laser

The physical origin of the peaks can be explained by a general phase-matching process between a soliton-like wave and a dispersive wave. In a mode-locked laser, the circulating pulse only gains a fixed amount of nonlinear phase and does not change its shape after every round-trip. However, unlike a real soliton whose shape always maintains during the propagation due to the balance of SPM and dispersion, the shape and the spectrum of the pulse travelling inside the laser cavity change dramatically within each round-trip. Also, in addition to SPM and dispersion, the soliton-like mode-locked pulse experiences loss and gain during the

propagation. Since the loss, gain, and TOD per round-trip are usually small in the steady-state, they can be treated as perturbations to a dispersion-managed soliton whose dynamics is still dominated only by the SPM and dispersion. These perturbations lead to radiation of dispersive waves that propagate around the cavity with only linear effects like dispersion and diffraction. When the phase contributed by the linear effects equals to the nonlinear phase experienced by the soliton wave, the newly generated and existing dispersive waves will coherently add up, result in resonantly enhanced peaks in the spectrum. The phase-matching process described here is similar to the fiber-optic Cherenkov radiation using photonic crystal fibers (PCFs). The only differences are that the soliton propagation is perturbed by TOD of the PCF and there is one phase-matching condition since the PCF only supports one spatial mode. The detailed explanation will be discussed in Chapter 5 of this thesis.

In the solid-state laser cavity, since the Kerr effect not only induces coupling between longitudinal modes via SPM but also the transverse mode via self-focusing, the dispersive wave at each wavelength can be viewed as a superposition of transverse modes. Even in the linear propagation regime, higher-order modes experience more Gouy phase than lower-order modes, which leads to a different phase-matching condition. Here we assume that the soliton is mainly in the fundamental transverse mode. By requiring that the nonlinear phase ϕ_{NL} is equal to the linear phase contributed by the cavity dispersion ϕ_D and the round-trip Gouy-phase shift $\phi_{Gouy,RT}$, one can write the a general phase-matching condition for any transverse mode assuming a radial symmetry

$$\phi_{NL} + \phi_{Gouy,RT} + 2m\pi = \phi_D(\lambda) + (2p+1)\phi_{Gouy,RT} \tag{3.44}$$

$$\phi_D(\lambda) = \phi_{NL} - 2p\phi_{Gouy,RT} + 2m\pi \tag{3.45}$$

According to eq. (3.45), the position of the phase-matching peaks becomes predictable as shown in Figure 3.30.

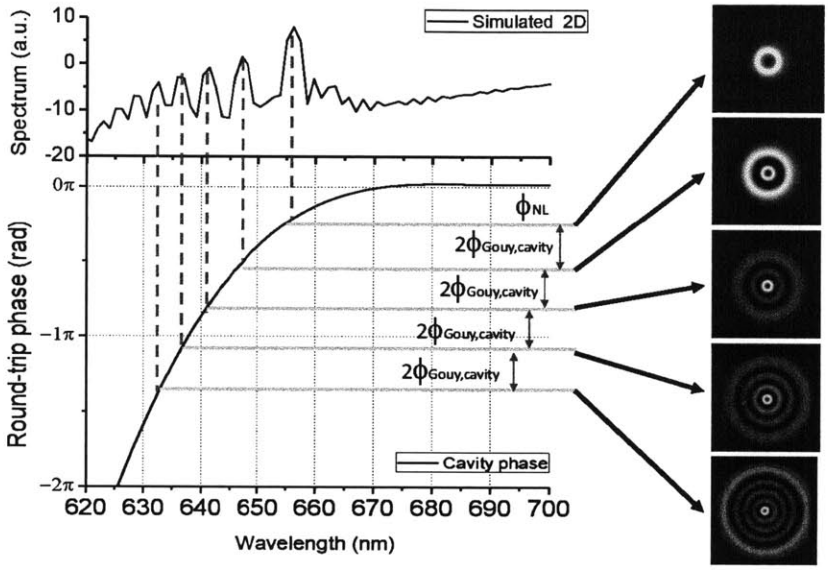

Figure 3.30 (Top) Zoom-in of the resonant peaks near 650 nm of the simulated. spectrum. (bottom) cavity round trip phase ϕ_D from dispersion. The color plots on the right show the beam profile corresponding to the phase-matched wavelengths.

3.5.7. Optimization of Laser Output Spectrum

According the phase-matching condition derived above, the fundamental mode can be enhanced when the nonlinear phase is equal to the linear phase contributed by the dispersion per round-trip. To demonstrate this idea, we artificially create a phase profile that phase-matches the nonlinear phase for the wavelengths above 1050nm and below 650nm, as shown in Figure 3.31. The original cavity has a dispersion of 0 fs^2 GDD and -2 fs^3 TOD and a constant output coupling of 3%.

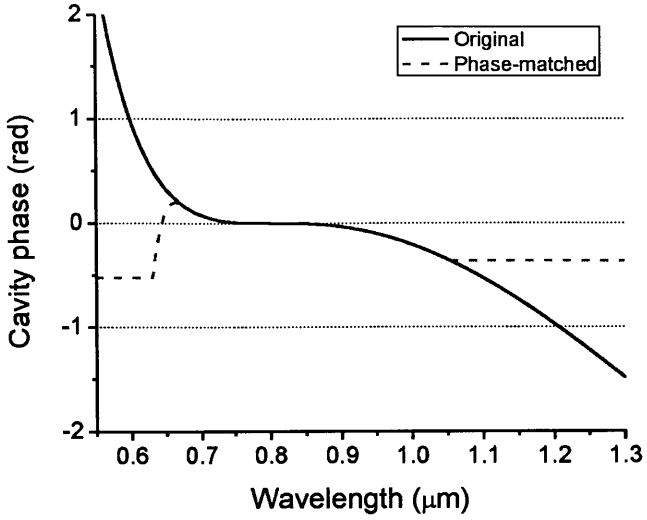

Figure 3.31 (Black solid) Round-trip phase from a cavity with 0 fs^2 GDD and -2 fs^3 TOD. (Red dashed) engineered phase for enhancing side-band generation using the phase-matching concept.

Figure 3.32 compares the simulated output spectra for the original and phase-matched cavities. We first tested the case with phase-matching on the long wavelengths side and then on both sides. As shown in the plot, the spectrum from 700 to 1000nm is nearly the same but the frequency components typically used for 1f-2f self-referencing are greatly enhanced.

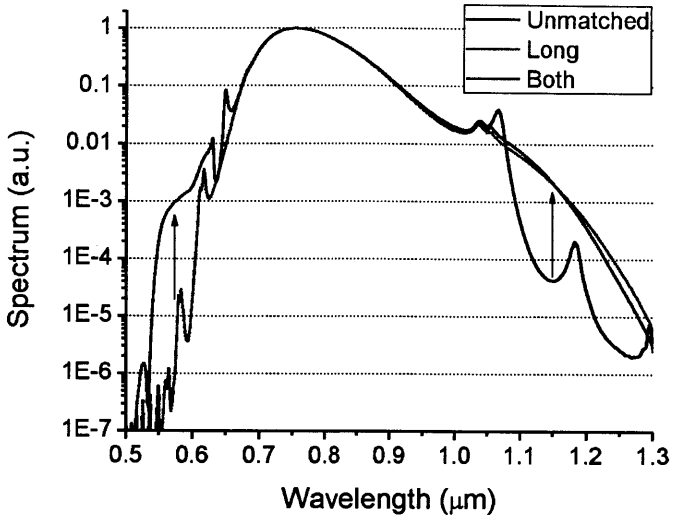

Figure 3.32 Simulated output spectra for (1) original cavity (Black), (2) cavity with phase-matching phase in long wavelength wing (Red), and (3) cavity with phase-matching phase in both wavelength wings (Red).

The wavelength-dependent beam profile plotted in Figure 3.33 confirms that the fundamental mode is enhanced for these wavelengths. To further optimize the laser, we gradually increase the output coupling from 3% to 100% for the wavelength below 600nm and above 1100nm and repeat the simulation. Figure 3.34 shows the simulated output spectra for each case. It is noticeable that the output power for the 1f-2f window drops when the output coupling increases. Also, since the intracavity enhancement process is done by the coherent interference between the existing wave in the cavity and newly-generated wave after each pass through the crystal, the process will become weaker when the loss of the cavity is too high. As a result, the beam profile will become less confined and eventually the structure will be dominated by the self-focusing effect in the single pass of the crystal when the output coupling becomes 100%. This is confirmed by the wavelength-dependent beam profile plotted in Figure 3.35.

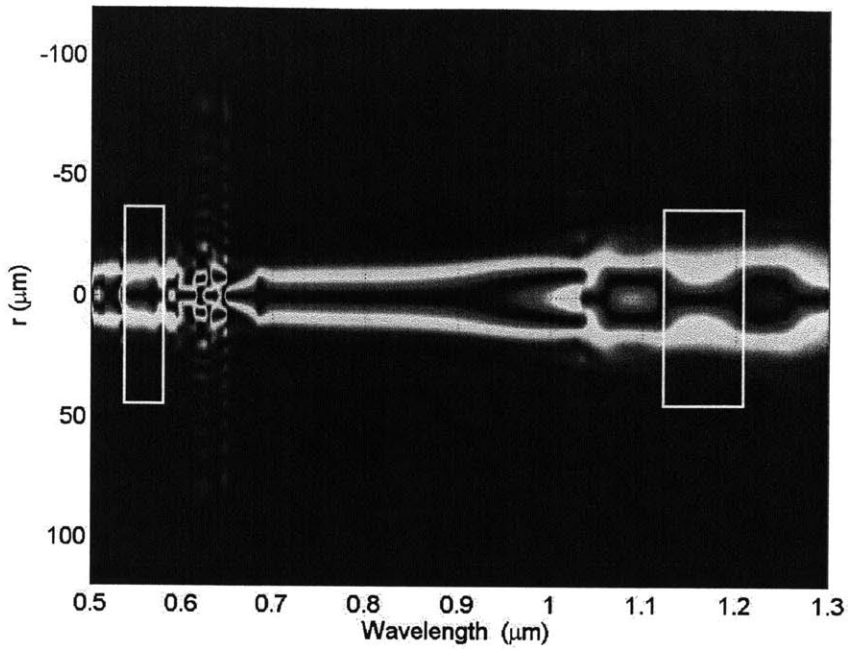

Figure 3.33 Simulated wavelength-dependent spatial beam profile from a phase-matched laser. Fundamental modes are generated for the 1f (1140nm) and 2f (570nm) wavelengths.

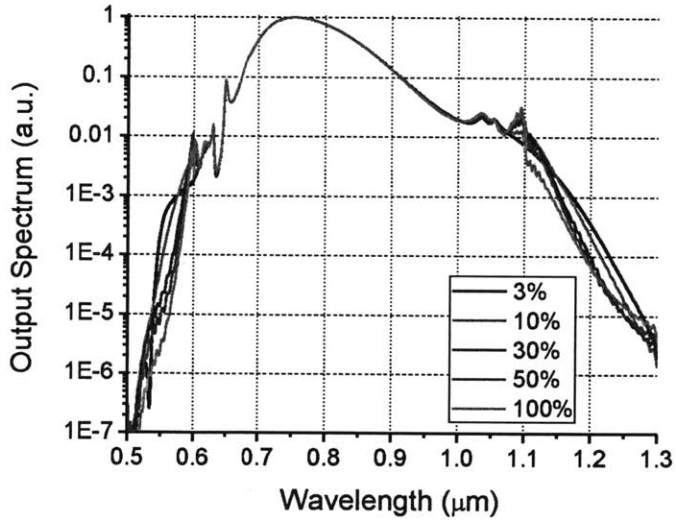

Figure 3.34 Simulated output spectra with different output coupling for the 1f and 2f wavelengths

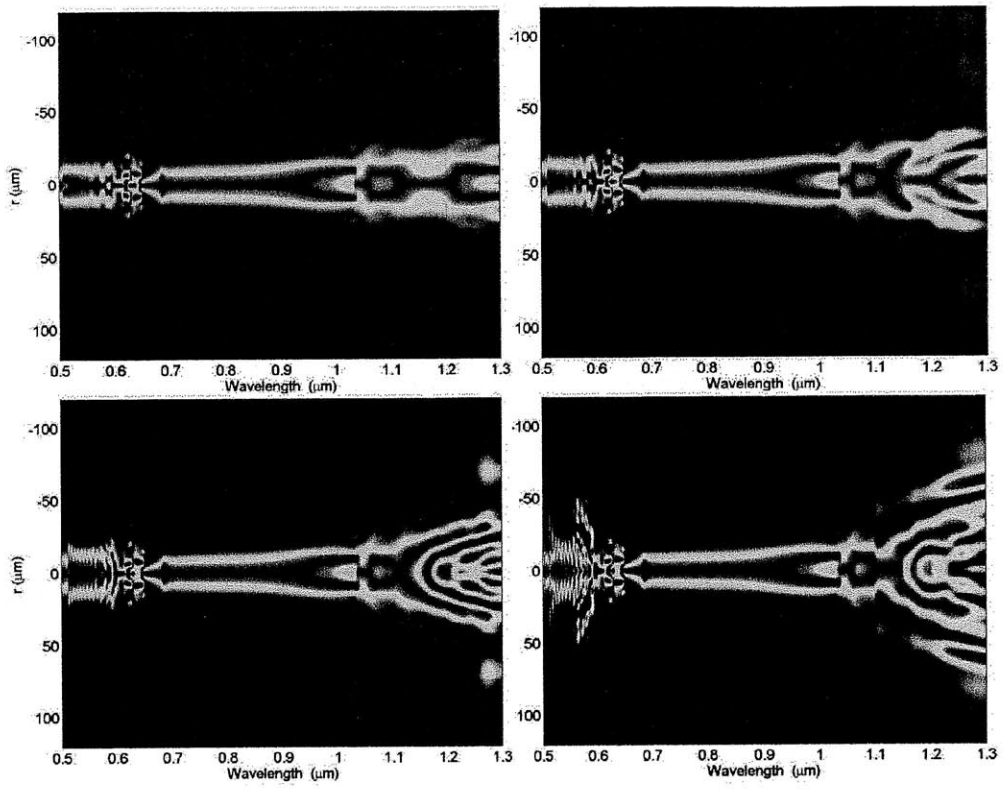

Figure 3.35 Simulated wavelength-dependent spatial beam profile from a phase-matched laser with different output coupling for the 1f and 2f wavelengths: (1) 10%, (2) 30%, (3) 50%, and (4) 100%. When the output coupling is higher, the beam becomes more structured.

Chapter 4

Gain-Matched Output Couplers

4.1. Motivations: Balance of pulse shortening and lengthening effects

Passive mode-locking assisted by the Kerr nonlinearity [16] has been experimentally proven to be a very successful technique for generating ultrashort pulses from various broadband laser media. As discussed earlier, the mechanism can be understood as an artificial saturable absorber that creates a self-amplitude modulation (SAM) on the circulating intracavity pulses, which leads to pulse shortening until pulse lengthening caused by gain-filtering keeps the balance. Different from traditional saturable absorbers [69] whose response is typically limited by the material characteristics, KLM utilizes an instantaneous lensing effect that imposes no additional limitations on the pulse duration achievable beyond the limitation set by the laser gain bandwidth and overall cavity dispersion. With an ultra-broadband gain medium such as Ti:sapphire, generation of octave-spanning spectra directly from a KLM laser cavity operating at different repetition rates using double-chirped-mirror pairs (DCMPs) has been demonstrated [49], [50], [70], [68], [71]. In order to overcome the strong gain-filtering effect, such lasers usually demand high pump power, low output coupling, and critical cavity alignment which

means that the laser can only be operated within a small range at the edges of the cavity stability region where SAM is maximized. Although optimization of the KLM strength has been studied both experimentally and theoretically by many researchers [30], [52], [72–75], the current operating point for the ultra-broadband version of these lasers suffers from many practical issues such as high mode-locking threshold, low laser efficiency, less robust operation, and greatly reduced beam quality. However, if there would be no or only strongly reduced net gain filtering, which implies that the total cavity loss has the same spectral profile as the gain, an arbitrary low KLM action could sustain short pulses covering the spectral range where the intracavity dispersion is well-compensated. This also suggests that mode-locking with less critical alignment, lower pulse energy, less self-focusing and, therefore, improved beam quality can be expected.

4.2. Output Coupler Design

Creating an intracavity frequency-dependent loss has been demonstrated previously in a Ti:sapphire regenerative amplifier with a thin angle-tuned etalon [76]. However, the etalon behaves as an additional lossy component that significantly lowers the laser efficiency. Moreover, the spectral profile of the transmitted power and phase cannot be controlled independently as they are predefined by the interference nature and the thickness of the etalon, which makes it very challenging to precisely match the laser gain profile over a large spectral range while not introducing uncompensatable dispersion. As a solution to this problem, a new type of gain-matched output coupler (OC) based on a multi-layer dielectric coating has

been designed. Since dielectric coatings do have a high flexibility in design, the presented technique provides a general solution as it can be adapted to lasers with vastly different gain media. In this paper, the general idea is demonstrated with a broadband dielectric gain-matched OC for a linear cavity Ti:sapphire laser supporting sub-10fs pulses. Under these conditions, we found that mode-locking can be initiated and run robustly with much improved beam quality for a pump power just above the continuous-wave (cw) lasing threshold.

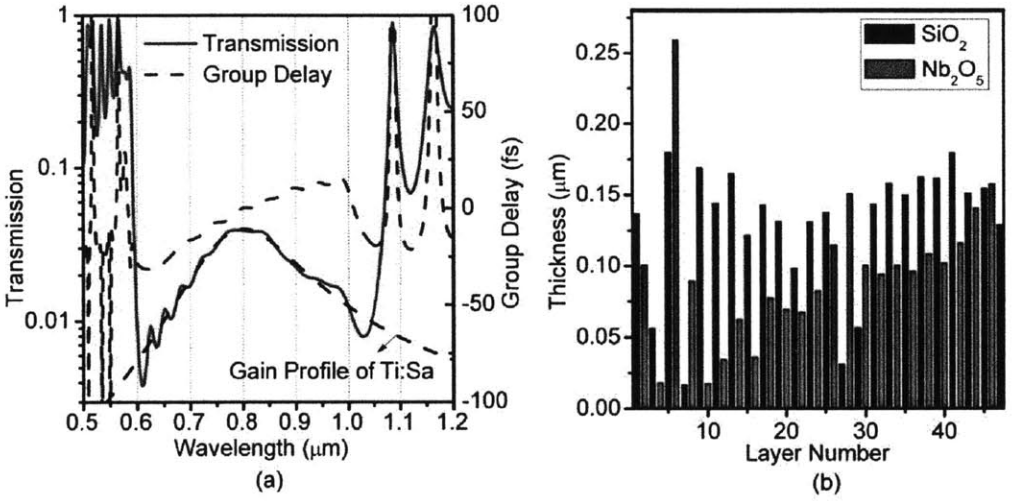

Figure 4.1 (a) Gain profile of Ti:sapphire crystal (dashed black) and the designed transmission (solid red) and group delay (dashed blue) of inverse-gain output coupler; (b) Layer structure of the gain-matched output coupler design. The layers are numbered from top (free-space) to bottom (substrate).

To derive the transmission profile for a gain-matched OC design, we start from measuring the fluorescence spectrum of the Ti:sapphire crystal [77] and use a rescaled version of it as the design goal in the coating optimization procedure. The measured spectrum shows a typical Lorentzian profile with a center frequency of 375 THz and a full-width-half-maximum of 101 THz. In order to minimize the

uncompensated dispersion introduced by the OC, we set the group-delay (GD) goal of the design to be complementary to BaF_2 of some to-be-determined path length, which can be easily taken into account by changing the already present intracavity BaF_2 plate to a thicker one. The design procedure optimizes the thicknesses and number of layers using the approach developed in [78]. Figure 4.1 (a) shows the design goal and nominal transmission characteristics of the gain matched OC. It has a peak transmission of 4% and a smooth GD that can be compensated by a 1.1 mm-long BaF_2 plate in the wavelength range of 600-1000 nm. Figure 4.1 (b) shows the structure of the gain-matched OC consisting of 47 layers of SiO_2/Nb_2O_5 on a fused-silica substrate. The impact of this design on the laser output was then first studied numerically using the model developed in [45]. Simulations of the pulse dynamics confirm that for a cavity with a gain-matched OC the modulation depth of the effective saturable absorption could be decreased by half its initial value and stable steady state pulses are still generated. With the previously used output couplers the modulation depth could not be varied over such a large range without loss of pulse stability. To further demonstrate it experimentally, the OC was fabricated and tested in a commercial 85 MHz ultrabroadband Ti:sapphire laser (IdestaQE Octavius-85M) in which three double-chirped-mirror pairs are used to compensate the material dispersion of the 3.6m-long air path, the 2.2mm-long Ti:sapphire crystal and three BaF_2 plates including two adjustable wedges for dispersion fine-tuning. Since the laser was originally equipped with a 1% OC that had only negligible dispersion, the dispersion change due to the gain-matched OC is

compensated by increasing the optical path length of BaF_2 in one arm of the laser cavity by 1.1 mm.

4.3. Characterization of Laser Performance

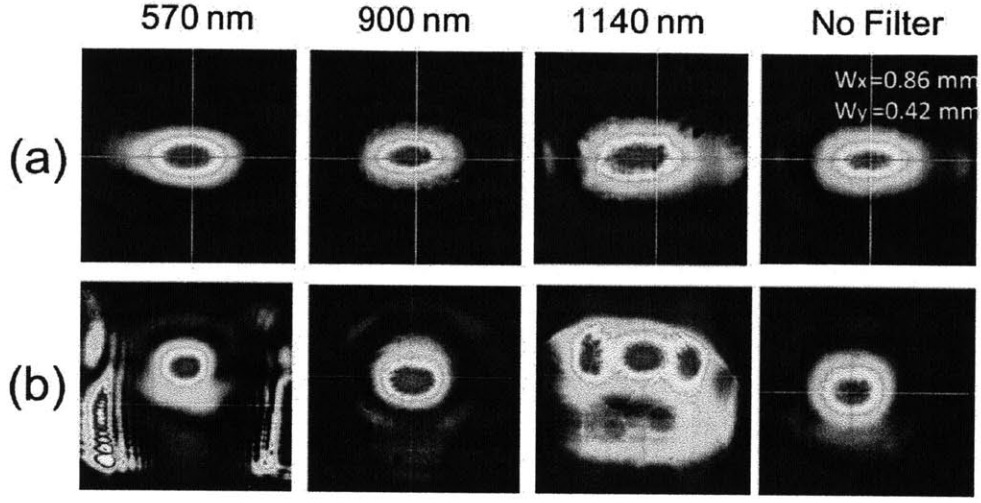

Figure 4.2 Measured beam profile of mode-locked Ti:sapphire laser when operated at (a) center of stability region with gain-matched output coupler and (b) edge of stability region with traditional output coupler without an interference filter and after 10 nm filters centered at 570 nm, 900 nm, and 1140 nm.

We first observed the cw-behavior of the laser and noticed that it lases at one or more wavelengths simultaneously in a range over 200 nm, which implies that a broadband, flat net-gain is successfully generated by the OC. By slightly tapping the end mirror, mode-locking is initiated easily, even so the cavity is at or near the center of the stability region where the SAM is small. The mode-locking is very robust even when the laser is directly exposed to free-space. Figure 4.2 (a) shows the mode-locked beam profile in this configuration both without any interference filter and after 10-nm filters centered at 570 nm, 900 nm, and 1140 nm

under 5.5 W pumping. Compared to the original laser without compensated gain filtering, the new design has improved beam quality with nearly no wavelength dependence across a range of frequencies spanning one octave. Moreover, there is no noticeable change in beam profile as we change the pump power. Figure 4.2 (b) shows the typical beam profiles at the corresponding wavelengths from the original laser in which frequency-dependent beam distortions [26] due to strongly coupled nonlinear effects and spot-size changes can be observed.

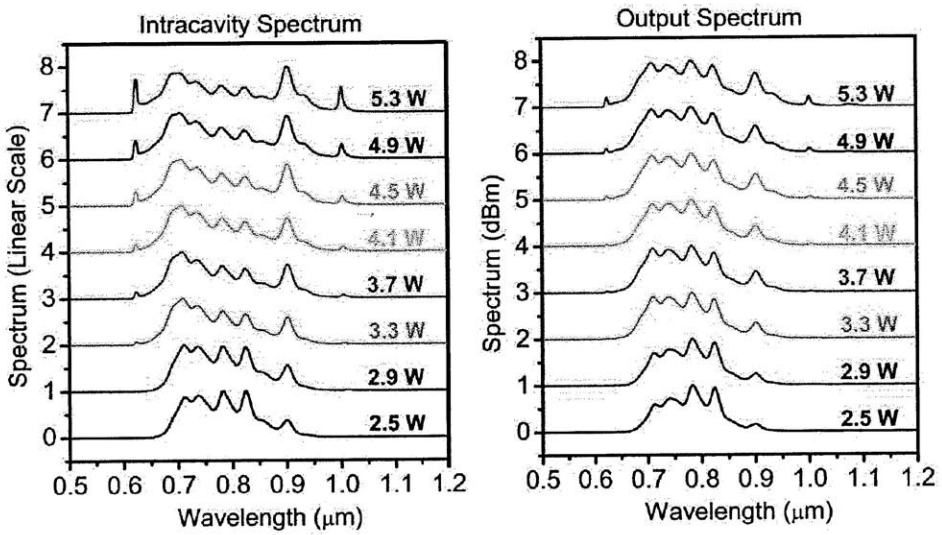

Figure 4.3 (a) Intracavity and (b) output optical spectrum generated at different pump power levels.

We also measured several important laser parameters to characterize its performance in such a low-SAM region. Since our test laser has a relatively high intracavity loss due to the scattering from many material surfaces, the cw lasing threshold is about 2.85 W. However, we are able to initiate mode-locking at a pump power of 2.9 W when the cw output power is only 7 mW. Once mode-locked, we could further decrease the pump power to 2.5 W and still generate sub-10 fs pulses.

Figure 4.3 shows the optical output spectrum and the corresponding intracavity spectrum calculated with the measured output coupling at different pump levels. As shown in the graph, the laser has only weak pump power dependence for the center portion of the output spectra. However, as the pump power increases, the intracavity pulse energy also increases, which induces stronger self-phase modulation that broadens the spectra and shortens the pulses. Due to the output coupling profile, the pulses undergo spectral filtering by the OC, so that the output pulse duration is longer by 5-10% percent in comparison with the intracavity pulse duration. Figure 4.4 (a) shows the calculated output and intracavity pulsewidth based on the measured spectrum assuming transform-limited pulses. As also plotted in Figure 4.4 (a), the measured output power from the gain-matched OC does not change significantly with increased pump power, since the output coupling profile produces reduced average loss seen by the intracavity pulses with increasing spectral bandwidth. Such bandwidth-dependent output coupling also explains the large difference between the cw and mode-locked output power (7 mW vs. 108 mW) near the lasing threshold (2.85 W). The calculated intracavity pulse energy based on the average output coupling is plotted as a function of pulsewidth in Figure 4.4 (b). The product of intracavity pulse width and pulse energy is almost constant indicating that optical soliton formation is the major pulse shaping process.

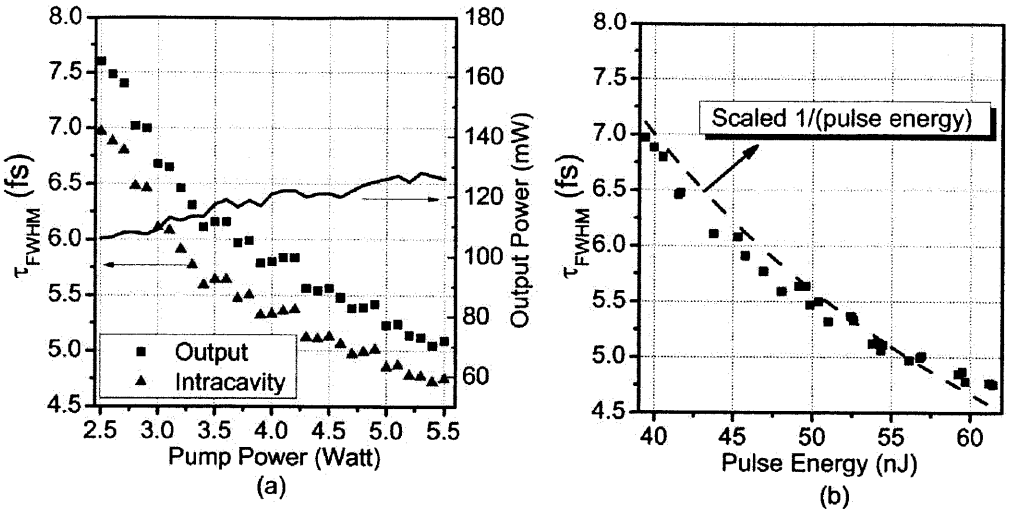

Figure 4.4 (a) Intracavity and output pulsewidth at different pump power levels (left axis) and the corresponding output power (right axis). (b) Calculated intracavity pulse energy vs. intracavity pulsewidth. Dashed curve shows pulsewidth that is inversely proportional to the pulse energy.

4.4. Summary

In conclusion, we have demonstrated that the use of a gain-matched output coupler greatly reduces the nonlinearity required for ultra-broadband mode-locking. Already at pump power levels close to the cw lasing threshold it is possible to initiate robust mode-locking and generate <8 fs output pulses from Ti:sapphire lasers with excellent beam quality operating in the center of its stability range. We believe this technique can be applied to many other lasers with widely different gain media to extract pulses covering the full gain spectrum of the laser medium with minimum saturable absorber action and at high average output power.

Chapter 5

Application: Fiber-Optic Cherenkov Radiation in the Few-Cycle Regime

5.1. Motivation and Application of Broadband Visible Wavelength Generation

Fiber-optic Cherenkov radiation (FOCR), also known as dispersive wave generation or non-solitonic radiation, describes the radiation from a fiber-optic soliton when perturbed by higher-order fiber dispersion [79–83]. This intriguing phenomenon has emerged as a wavelength conversion technique to generate significant radiation in the visible-wavelength range, where mode-locked femtosecond lasers are not available [84–88]. First theoretically studied in 1986, FOCR has attracted renewed research interest in company with the advent of photonic crystal fibers (PCFs) whose properties can be flexibly engineered [89]. For example, controlling a PCF's hole-size and inter-hole spacing results in two zero-dispersion wavelengths (ZDWs) which in turn give rise to two FOCR bands [90]. As a matter of fact, deliberate designs allow the presence of three ZDWs [91]; such a PCF would accommodate a variety of novel phenomena arising from phase-matched interactions between soliton and the resulting FOCR [92]. To date, most of FOCR research in PCFs is carried out in the context of supercontinuum generation

since FOCR extends the spectrum towards shorter wavelength [84], [85], [93–98]. Supercontinuum generation requires that the pump pulse propagate in the anomalous dispersion regime and form a higher-order soliton. To achieve a SC without substantial spectral gaps, the pump's center wavelength needs to be close to the fiber's ZDW so that the generated FOCR merges with the spectral components building up from other nonlinear effects. As this wavelength separation increases, FOCR manifests as an isolated spectrum that corresponds to a wavelength up-conversion or down-conversion of the pump depending on the sign of the third-order dispersion [86], [87], [90], [99], [100]. The up-conversion FOCR is of particular importance due to its capability of converting near-infrared (NIR) ultrafast lasers (e.g., Ti:Sapphire laser) to their counterparts in the visible wavelength range. The resulting ultrafast sources are desired in many applications, such as multi-photon microscopy, fluorescence spectroscopy, and optical coherence tomography. It is widely believed that FOCR generates resonant, narrowband (i.e., ~10 nm in the visible wavelength range) spectrum with relatively low conversion efficiency (~10%). These two drawbacks have hampered many real-world applications that demand high photon flux with a broadband coverage. Recently, we have explored the dependence of these two quantities (i.e., bandwidth and conversion efficiency) on the NIR pump-pulse's parameters (such as duration and pulse energy), and have demonstrated FOCR featuring high efficiency (>40%), broadband spectrum (>50 nm), and low threshold (<100 pJ for pulse energy) [101]. Such a dramatic improvement results from using few-cycle pump pulses to drive the radiation.

Generation of few-cycle laser pulses and their applications for investigating ultrafast processes in physics and chemistry have received a great deal of research attention [102]. While FOCR excited by few-cycle pulses has been pursued for different purposes (e.g., investigation of soliton-trapped FOCR [88] and synthesis of single-cycle pulses [103]), a thorough and detailed study of FOCR emphasizing bandwidth and conversion efficiency in this new regime is yet absent. In this chapter, the FOCR in the few-cycle regime will be theoretically and experimentally investigated.

5.2. Theory of Fiber-Optic Cherenkov Radiation

In the FOCR process, three characteristic propagation scales are defined: 1) initial buildup stage in which FOCR acquires most (>90%) of its energy; 2) quasi-independent propagation with minimal interaction with its host soliton; and 3) strong interaction with the host soliton that is decelerated by stimulated Raman scattering (SRS). Since the FOCR spectrum splitting and trapping that take place in the 3rd stage has been well studied, we rather focus on the first two stages.

5.2.1. Phase-matching and the Concept of Coherence Length

Propagation of an ultrashort pulse inside an optical fiber is well modeled by the generalized nonlinear Schrödinger (GNLS) equation [104]

$$\frac{\partial A}{\partial z}+\left(\sum_{n=2}^{\infty}\beta_n\frac{i^{n-1}}{n!}\frac{\partial^n}{\partial T^n}\right)A=i\gamma\left(1+\frac{i}{\omega_0}\frac{\partial}{\partial T}\right)\left(A(z,T)\int_{-\infty}^{+\infty}R(t')\left|A(z,T-t')\right|^2dt'\right) \tag{5.1}$$

where $A(z,t)$ represents the input pulse's amplitude envelope. $\beta_n=\frac{\partial^n\beta(\omega)}{\partial\omega^n}$ is evaluated at the central frequency ω_0 of the input pulse. γ is the nonlinear parameter

of the fiber and $\beta(\omega)$ the fiber's dispersion curve. $R(t)$ describes both the instantaneous electronic and delayed molecular responses (i.e. SRS) of fused silica, and is defined as

$$R(t) = (1 - f_R)\delta(t) + f_R[(f_a + f_c)h_a(t) + f_b h_b(t)] \tag{5.2}$$

Typical values of f_R, f_a, f_b, and f_c are 0.245, 0.75, 0.21, and 0.04, respectively [105]. Isotropic Raman response $h_a(t)$ and anisotropic Raman response $h_b(t)$ are defined as

$$h_a(t) = (\tau_1^2 + \tau_2^2)/(\tau_1 \tau_2^2)\exp(-t/\tau_2)\sin(t/\tau_1) \tag{5.3}$$

$$h_b(t) = \Theta(t)(2\tau_b - t)/\tau_b^2 \exp(-t/\tau_b) \tag{5.4}$$

where τ_1, τ_2, and τ_b have values of 12 fs, 32 fs, and 96 fs, respectively. If higher-order dispersion (i.e. β_n , n>2), self-steepening, and SRS are absent, equation under $\beta_2 < 0$ supports fundamental soliton solution with propagation constant

$$\beta_s(\omega) = \beta_0 + \beta_1(\omega - \omega_0) + (1 - f_R)\gamma P_0/2 \tag{5.5}$$

The peak power P_0 and full-width-half-maximum (FWHM) duration T_0 are related by the soliton area theorem, i.e.,

$$(1 - f_R)\gamma P_0 = 3.1|\beta_2|/T_0^2 \tag{5.6}$$

Optical soliton—a non-dispersive pulse with the propagation constant $\beta_s(\omega)$—is a consequence of interplay between anomalous dispersion and self-phase modulation (SPM). Higher-order dispersion exerts perturbation onto a soliton and enforces it to shed away energy carried out by a dispersive pulse; the pulse travels with a propagation constant which coincides with the fiber's dispersion curve $\beta_s(\omega)$. Evidently, two sources contribute to the FOCR at position $z+\Delta z$: (1) the FOCR at z, which propagates Δz distance and acquires an extra phase due to fiber dispersion;

and (2) the new radiation emitted by the soliton as it moves from z to Δz. Depending on their phase difference, these two fields add up constructively or destructively. If the phase-matching condition, i.e. $\beta_s(\omega)=\beta(\omega)$, is satisfied for any frequency, the two fields stay in-phase all the time and the generation of FOCR is maximized. In reality, however, the phase-matching condition only holds at a certain discrete frequencies. This is owing to the fact that $\beta_s(\omega)$ is a linear function of frequency (that is why soliton is non-dispersive) while $\beta(\omega)$ could be highly oscillatory for specially engineered dispersion. These phase-matched frequencies grow up monotonically along the propagation due to constructive interference. In contrast, non-phase-matched frequencies experience destructive interference and thus are strongly suppressed given enough propagation distance. Such a phase-sensitive mechanism explains why FOCR is widely regarded as a resonance process and forms a narrowband spectrum—a popular image one bears in mind. To describe phase-mismatch caused spectral narrowing, we introduce a new quantity L_c —*coherence length*—defined as

$$L_c(\omega) = \pi / |\beta(\omega) - \beta_s(\omega)| \tag{5.7}$$

Plugging in the expression of the soliton's propagation constant, after a little math, the coherence length can be expressed as a function of fiber's dispersion and input soliton peak power,

$$L_c(\omega) = \frac{\pi}{|\beta(\omega) - \beta_s(\omega)|} = \frac{\pi}{\left|\sum_{n\geq 2} \frac{(\omega-\omega_0)^n}{n!}\beta_n(\omega_0) - \frac{(1-f_R)\gamma}{2}\right|} \tag{5.8}$$

Apparently L_c characterizes the fiber length where a π phase-slip accumulates between the CR radiated by a soliton located at $z+L_c$ and the radiation that emerges

at z and then propagates to $z+L_c$. A destructive interference between these two radiations diminishes the efficient power buildup of a FOCR.

It is noteworthy that the physical picture behind FOCR is quite universal in nonlinear optics, especially in illustrating -initiated nonlinear phenomena, such as second-harmonic generation, sum-frequency generation, difference-frequency generation, etc. For example, when driven by femtosecond pulses, optical rectification—a degenerate difference-frequency generation—gives rise to generation of broadband spectrum located at terahertz regime. In fact, we have borrowed the concept of coherence length from the terahertz community. In the context of ultrafast terahertz generation, coherence length quantifies the matching between the terahertz pulse's phase-velocity and the optical pulse's group velocity [106]. This velocity-matching is intrinsically equivalent to phase-matching required for efficient three-wave (i.e. terahertz frequency and two optical frequencies for optical rectification) mixing in a $\chi^{(2)}$ nonlinear process.

For a $\chi^{(2)}$ nonlinear process, it is the thickness of the nonlinear crystal that largely determines phase-matching bandwidth. Thus a thinner crystal is desired to achieve broader bandwidth at the cost of a decrease in conversion efficiency. Since FOCR shares a similar physical mechanism, one may ask whether such a tradeoff between bandwidth and conversion efficiency also exists for FOCR. Answering this question necessitates numerically solving the GNLS equation.

5.2.2. Continuum generation in the few-cycle regime

To investigate the effect of coherence length, we perform simulations for a fundamental soliton propagating in a PCF. The mode-field diameter of the PCF is 1.2 μm. The group-velocity dispersion shown in Figure 5.1 indicates that the PCF has a ZDW at 0.71 μm. Also plotted in the same figure are the coherence lengths for three fundamental solitons with different FWHM duration (i.e. T_0) or center wavelength (i.e. λ_c) which are specified in the legend of Figure 5.1. These three curves share similar features:

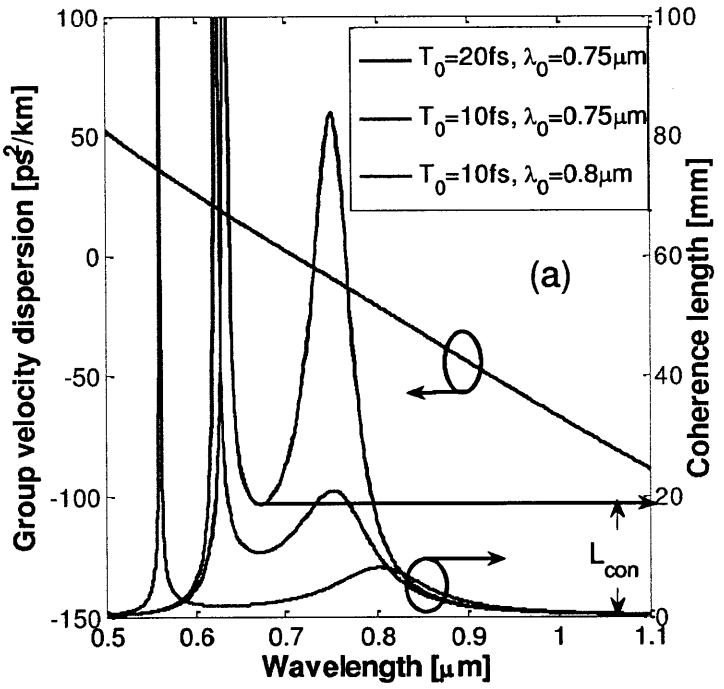

Figure 5.1 The PCF's group velocity dispersion and calculated coherent length for three fundamental solitons with different peak power or center wavelength (see the legend). L_{con} labels the continuum length for the blue curve.

1) The coherence length goes to infinity at the phase-matching wavelength which is shorter than the soliton center wavelength due to a positive third-order dispersion (i.e. $\beta_3(\omega_0)>0$).

2) Similar to a $\chi^{(2)}$ nonlinear process, the FOCR phase-matching bandwidth depends on propagation distance. At the vicinity of the phase-matching wavelength, which is practically useful, the phase-matching bandwidth decreases with the increase of propagation distance.

3) Below a certain distance L_{con} (we refer to it as continuum length hereafter; see the label in Figure 5.1 as an example), phase mismatch $<\pi$ is achieved for a continuous, broad wavelength range covering hundreds of nanometers. For shorter soliton duration (equivalent to increasing soliton peak power) or increasing soliton center wavelength blueshifts the phase-matching wavelength while the continuum length decreases accordingly.

The broad phase-matching bandwidth around the continuum length strongly suggests that a continuum might build up spanning between the phase-matching wavelength and the soliton center wavelength. To verify such a prediction, we take each of the three fundamental solitons as the input and numerically solve the GNLS equation. Figure 5.2 and Figure 5.3 record the resulting spectral evolution for these three solitons propagating up to 10 cm; the spectra normalized to their peak power at each position are shown in logarithm scale. Despite calculated for different inputs, the corresponding spectra evolve following a similar pattern:

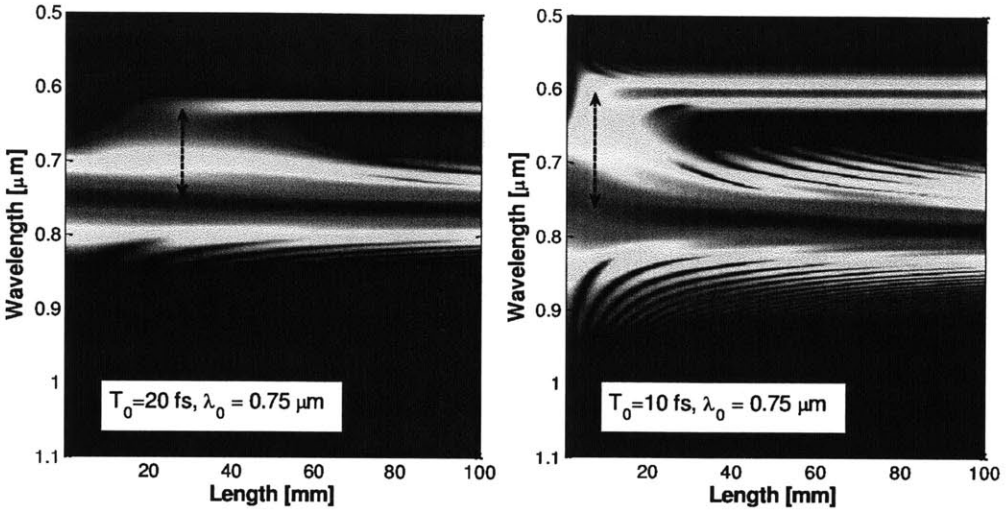

Figure 5.2 Spectrum evolution along propagation distance for fundamental solitons with different FWHM duration. The spectrum intensity is shown in logarithm scale. The double-arrow line marks the continuum that connects the phase-matching wavelength and the soliton center wavelength.

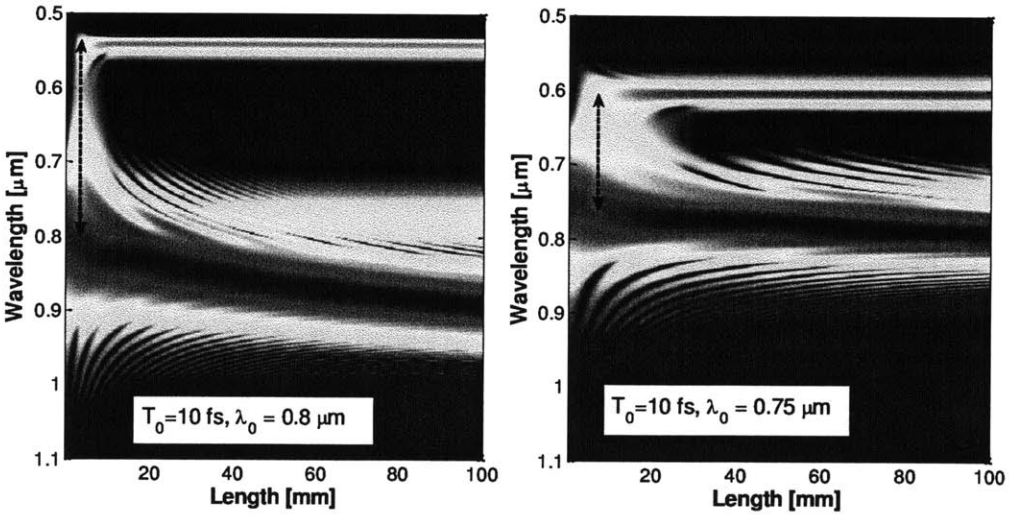

Figure 5.3 Spectrum evolution along propagation distance for fundamental solitons with different center wavelength. The spectrum intensity is shown in logarithm scale. The double-arrow line marks the continuum that connects the phase-matching wavelength and the soliton center wavelength.

1) As the soliton enters the PCF, higher-order dispersion together with other nonlinear effects (e.g., self-steepening and SRS) initiates the FOCR, which primarily extends to the shorter wavelength as predicted by the coherence length shown in Figure 5.1.

2) The blue edge of the radiation eventually reaches the phase-matching wavelength. Meanwhile, a continuum (marked by the double-arrow line in each figure), spanning between the soliton's center wavelength and the phase-matching wavelength, forms at the distance close to the calculated continuum length L_{con}.

3) At the distance of about $2L_{con}$, the continuum nearly vanishes and an isolated spectrum builds up which stays almost unchanged for further propagation.

4) The phase-matching wavelength (i.e. the FOCR peak wavelength) obtained by numerically solving the GNLS equation is always shorter than predicted by equation (5.8). This discrepancy arises from the spectral recoil effect: to preserve the entire-spectrum's center-of-mass, the emitted FOCR red-shifts the soliton spectrum, which in turn emits new FOCR at even shorter wavelength [95]. Consequently, the resulting FOCR is further blue-shifted with a broader bandwidth compared to the prediction from equation (5.8).

Generation of continuum highly depends on input soliton's duration. A comparison between Figure 5.2 reveals that using a shorter, few-cycle pulse as the

input favors continuum generation accompanied by higher power conversion efficiency and better spectral flatness. For most reported FOCR experiments, which exploit input pulses of ~100-fs duration, the continuum generation is extremely weak and thus not observed.

5.2.3. Higher conversion efficiency in the few-cycle pulse regime

Results in Figure 5.1 to Figure 5.3 confirm the physical picture described in section 2; that is, FOCR at a propagation distance $z+\Delta z$ includes two parts: the radiation accumulated before z and new radiation as the soliton travels from z to $z+\Delta z$. Note that the new added radiation $\Delta E_{CR}(\omega)$ is proportional to Δz as well as to the soliton's spectral amplitude at ω. Therefore, a soliton with shorter duration extends more in the spectral domain which enhances FOCR generation, leading to a higher conversion efficiency as indicated by the comparison in Figure 5.2.

The simulation performed in last section has assumed fundamental solitons as the input, which possess low pulse energy. For example, the soliton centered at 0.75 μm with 20-fs duration is only 12 pJ. The typical pulse energy in FOCR experiments is normally at ~1 nJ level. In this scenario, the input hyperbolic secant pulse becomes a Nth-order soliton rather than a fundamental soliton; the soliton order N is given by

$$N = \sqrt{0.32(1-f_R)\gamma P_0 T_0^2 / |\beta_2|} \propto \sqrt{E_0 T_0}, \tag{5.9}$$

where E_0 is the soliton's energy. When perturbed by higher-order dispersion and SRS, a Nth-order soliton becomes unstable and breaks into N fundamental solitons

with different peak powers and durations [107]. The resulting jth ($0<j<N+1$) fundamental soliton has the peak power P_j, duration T_j, and energy E_j given by

$$P_j = P_0(2N-2j+1)^2/N^2 \tag{5.10}$$

$$T_j = T_0/(2N-2j+1) \tag{5.11}$$

$$E_j = E_0(2N-2j+1)/N^2 \tag{5.12}$$

While all these fundamental solitons participate in the FOCR, their contributions differ dramatically. The first (corresponding to $j=1$) fundamental soliton, which possesses the shortest duration and highest peak power, has the strongest spectral amplitude at a given frequency and thus dominates the FOCR yield [98]. The coherence length may be extended to the following expression which is also valid for higher-order soliton as an input:

$$L_c(\omega) = \frac{\pi}{\left|\sum_{n\geq 2}\frac{(\omega-\omega_0)^n}{n!}\beta_n(\omega_0) - \frac{(2N-1)^2(1-f_R)\gamma P_0}{2N^2}\right|}. \tag{5.13}$$

Equation (5.9) indicates that, if soliton energy E_0 is fixed, soliton number N decreases with a reduction of soliton duration T_0. A less N results in a larger P_j, a shorter T_j, and a larger E_j , which in turn lead to a stronger FOCR carrying more shed energy. In other words, using a shorter soliton as the excitation pulse improves FOCR conversion efficiency.

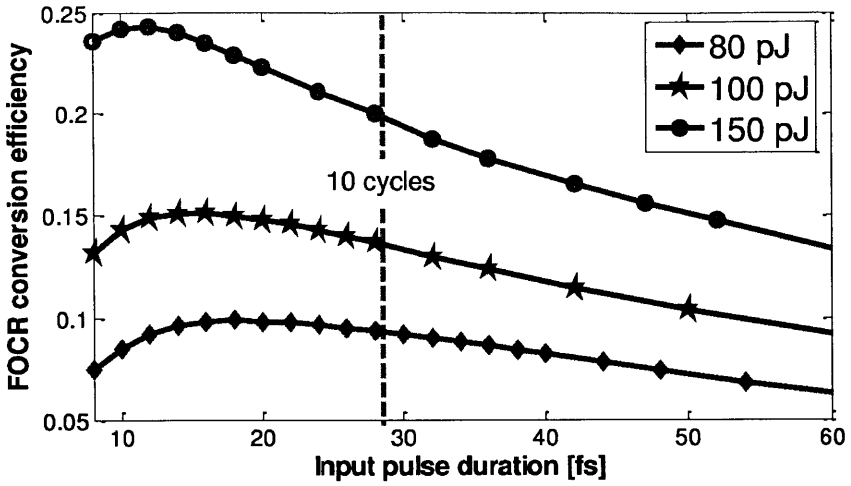

Figure 5.4 Dependency of FOCR conversion efficiency on input pulse duration for different pulse energy. An optimum duration in maximizing conversion efficiency exists for a given input pulse energy; the optimum duration becomes shorter with increasing pulse energy. The orange dashed line indicates the duration that corresponds to a pulse of 10 cycles centered at 0.8 μm.

From above analysis, one might speculate that, with input pulse energy fixed, conversion efficiency may monotonically increase as the input pulse duration decreases. As a matter of fact, this is not true. It has been well known that, if T_0 is so small that the resulting soliton number is much less than 1, fiber dispersion overtakes the nonlinearity and no soliton can form. As a result, FOCR is absent. Therefore there must be an optimum pulse duration that maximizes conversion efficiency for a given input energy. Figure 5.4 plots dependency of FOCR conversion efficiency on input pulse duration for different pulse energy. Evidently, an optimum duration in maximizing conversion efficiency exists for a given input pulse energy, and it becomes shorter with increasing pulse energy. More specifically, the optimum duration decreases from 18 fs to 12 fs as the input pulse duration increases from 80 pJ (red line with diamond marker) to 150 pJ (green line

with square marker); the conversion efficiency at the optimum duration goes up from 10% to 24%. For a given duration, increasing input pulse energy always improves conversion efficiency. The dashed, orange line marks the duration corresponding to 10 carrier oscillation cycles at 0.8 μm. The fact that the optimum duration is less than 10 optical cycles even for a moderate energy level (80 pJ - 150 pJ) indicates that FOCR in the few-cycle regime is highly desirable to achieve higher conversion efficiency and stronger FOCR pulse. The soliton order ranges 1.5 – 2 at the optimum duration.

5.2.4. Broader bandwidth in the few-cycle regime

In the physical picture that qualitatively describes FOCR generation and evolution, the emitted FOCR linearly propagates inside the fiber, only experiencing fiber dispersion. Such a model is valid when the conversion efficiency is low so that the resulting weak FOCR pulse creates negligible nonlinear effects. Apparently this is not the case for FOCR in the few-cycle regime featuring high conversion efficiency. In this new regime, FOCR pulse may carry ~40% of the total input energy [101], strong enough to cause nonlinear effects (e.g., SPM) which in turn reshape the FOCR pulse and broaden its optical spectrum.

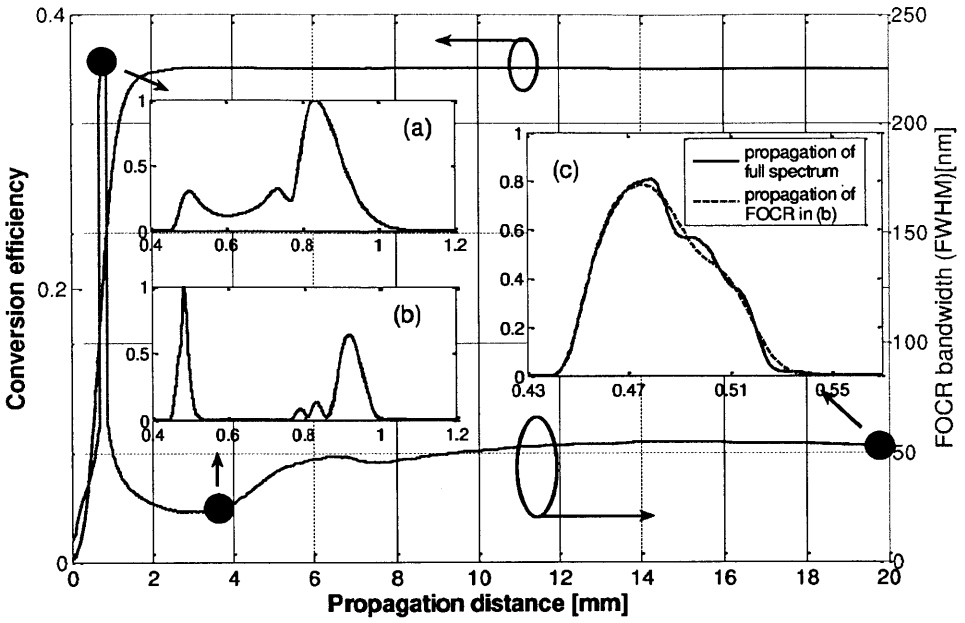

Figure 5.5 Evolution of FOCR conversion efficiency and spectral bandwidth along propagation distance for a 10-fs hyperbolic secant pulse centered at 0.8 μm with 300-pJ pulse energy. Insets (a) and (b) plot spectra corresponding to the maximum and minimum bandwidth. Further propagation of spectrum recorded in (b) up to 2 cm results in the FOCR spectrum shown as the blue, solid line in inset (c). If we propagate only the FOCR spectrum (i.e., spectrum in 0.4-0.6 μm), the corresponding spectrum at 2-cm distance is denoted by the red, dashed curve. See the text for details. Note that the spectra are shown in linear scale.

Figure 5.5 plots the evolution of FOCR conversion efficiency and spectral bandwidth along propagation distance for an input 10-fs pulse of hyperbolic secant shape centered at 0.8 μm with 300-pJ pulse energy. The spectral bandwidth is FWHM of the optical spectrum located in the range of 0.4-0.7 μm. The spectra at 0.8 mm, 4 mm and 20 mm are presented as inset (a)-(c), respectively. A comparison of FOCR spectral bandwidth reveals a three-stage evolution, which normally does not coincide with the aforementioned three-stage process in terms of conversion efficiency:

1) Stage 1 (0 - 0.8 mm): rapid growing of spectral bandwidth due to continuum generation as a result of large phase-matching bandwidth. At the end of this stage, the FOCR continuum partially overlaps with the red-shifted soliton spectrum, forming a smooth supercontinuum (spectrum in inset (a) of Figure 5.5) which spans more than one octave. The spectrum between 0.4 and 0.7 μm accounts for ~20% of the total input energy.

2) Stage 2 (0.8 - 4 mm) mm: fast narrowing of the spectrum within 0.4-0.7 μm due to the reduced phase-matching bandwidth as propagation proceeds beyond the coherence length. The continuum's short-wavelength edge concentrates more and more energy, while the longer-wavelength side diminishes during propagation, leading to the formation of an isolated FOCR spectrum. This stage ends up with a FOCR spectrum of 23 nm bandwidth, which carries 35% of the total input energy. As the spectrum in inset (b) of Figure 5.5 shows, the narrowband FOCR spectrum and its host pumping spectrum are well separated with a spectral gap of ~300 nm. The phase-matching wavelength (i.e. the FOCR peak wavelength) obtained by numerically solving the GNLS equation is always shorter than predicted by equation (14). This discrepancy arises from the spectral recoil effect: to preserve the entire-spectrum's center-of-mass, FOCR red-shifts the soliton spectrum, which in turn emits new FOCR at even shorter wavelength [9]. Consequently, the resulting FOCR is further blue-shifted with a broader bandwidth compared to the prediction from equation (5.13).

3) Stage 3 (4 - 15 mm): gradual broadening of the isolated FOCR spectrum up to 53 nm. The constant conversion efficiency in this stage indicates that there is no further energy exchange between the isolated FOCR spectrum and the residual pump. In the time domain, the residual pump pulse travels faster than the FOCR pulse. Their temporal separation increases during propagation and thus the nonlinear interaction between them diminishes continuously. To verify that the FOCR pulse propagates almost independently from the residual pump pulse in this stage, we seed the GNLS equation with the FOCR spectrum at 4-mm distance (i.e. the isolated spectrum within 0.4-0.6 μm in inset (b) of Figure 5.5), and propagate it for 16 mm; the resulting spectrum is plotted in inset (c) as the red, dashed curve. Clearly, the two spectra perfectly overlap on the short wavelength side (0.43-0.47 μm) and deviate slightly on the long wavelength side (0.47-0.55 μm) while they possess the same energy (i.e., integrated area under both curves). The deviation arises from cross-phase modulation (XPM) exerted by the residual pump pulse whose trailing tail overlaps with the FOCR pulse's leading tail. Propagating in the normal dispersion region, the FOCR pulse develops positive chirp; that is, its leading tail corresponds to the longer wavelength. That explains why such XPM only modifies the FOCR's long wavelength side, leaving the other side unaffected. The results shown in inset (c) also indicate that main mechanism for the FOCR spectral broadening from 23 nm to 53 nm is attributed to the nonlinear effects (e.g., SPM and self-steepening) caused by the FOCR pulse itself. Apparently, a

higher FOCR conversion efficiency—a consequence when pumped in the few-cycle regime—results in a stronger FOCR pulse which facilitates the broadening process.

Note that the concept of coherence length explains the buildup of the FOCR in the first two stages. In the third stage in which CR emission stops, coherence length is not meaningful since interaction between CR and the pump pulse is absent. As for further propagation beyond 20 mm, part of the residual pump develops into a soliton (hereafter, we refer it as Raman soliton) which continuously shifts towards longer wavelength driven by SRS, and as a result, slows down. Eventually the FOCR pulse catches up with the decelerating Raman soliton; their strong nonlinear interaction splits the FOCR spectrum into two well-separated parts. The shorter wavelength part will be captured by the Raman soliton. Detailed studies on FOCR spectral splitting and trapping have been presented in Ref. [88], [101].

5.3. Simulation and Experimental results

To be consistent with experimental results, we simulated an optical pulse centered at 0.8 μm propagating inside a photonic crystal fiber [(PCF) NL-1.8-710, Crystal Fibre A/S]. As the group velocity dispersion curve in Figure 5.6 shows, the fiber exhibits zero dispersion at 0.71 μm. Also plotted in the same figure is the optical spectrum after 2 cm propagation of a hyperbolic-secant pulse with 10 fs FWHM and 300 pJ energy. Clearly, CR has developed an isolated spectrum centered at 0.5

μm determined by the phase-matching condition. Spanning more than 60 nm, this isolated spectrum carries about 40% of the total input power.

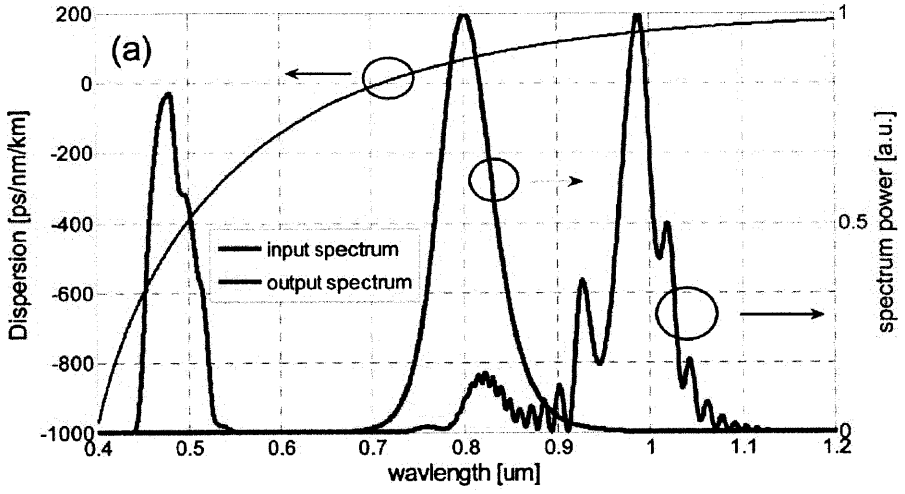

Figure 5.6 PCF dispersion and pulse spectrum after propagating a 300 pJ, 10 fs pulse through 2 cm PCF and

Figure 5.7 illustrates CR efficiency as a function of input pulse energy for three different pulse FWHM durations. We consider the power distributed between 0.4 μm and 0.6 μm being carried on by CR because the isolated CR spectrum appears in this region for all the simulated cases. The CR efficiency is simply defined as the portion of total and a tuning range over 100 nm. Cherenkov radiation Excitation sources: 85MHz and 1GHz Ti:sapphire lasers input power converted into the CR spectrum. Three curves in Figure 5.7 corresponding to 10 fs, 50 fs, and 100 fs follow the same trend: the CR efficiency grows drastically with the increment of input pulse energy and tends to saturate at higher energy levels. These simulations immediately suggest that CR can be a highly efficient (>40%) process if 10 fs level pulses are employed. The broader bandwidth (>60 nm) indicated by Figure 5.6

constitutes another benefit brought from switching to shorter excitation pulses. These two merits (i.e., high efficiency and broad band) are of particular importance for applications that require larger bandwidth out of relatively weak ultrafast sources.

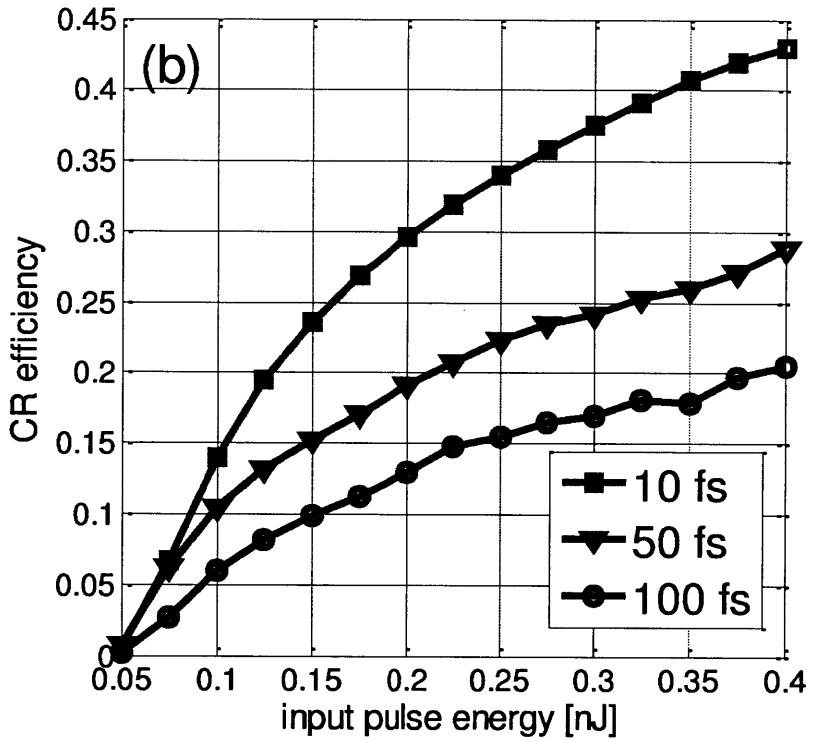

Figure 5.7 (b) CR efficiency versus input pulse energy for three FWHM durations of the input pulse: 10 fs, 50 fs, and 100 fs.

Guided by the simulation, we have performed a series of experiments on CR from NL-1.8-710 PCF pumped by a homebuilt Ti:sapphire laser operating at 85 MHz repetition rate with ~10 fs pulse duration. Because the fiber exhibits slight birefringence, we use an achromatic half-wave plate to align the input pulse polarization and ensure a linearly polarized output. The input power is adjusted with a neutral-density filter wheel inserted into the beam path. The dispersion of the

neutral-density filter, the achromatic half-wave plate, and the coupling lens to the fiber is compensated by 10 bounces on double-chirped mirrors [33–35]. Each bounce provides -60 fs^2 group-delay dispersion. The PCF output is collimated and sent into an optical spectrum analyzer (OSA) or a power meter. To reveal the evolution of CR along the propagation distance inside the fiber, which has not been experimentally studied before, we coupled 300 pJ pulses into PCFs of different lengths and recorded the corresponding spectra in Figure 5.9. The results suggest three evolution stages corresponding to three fiber length scales: (i) CR within several millimeters, (ii) CR spectral broadening due to self-phase modulation within a few centimeters, and (iii) blueshift and splitting of CR's spectrum due to the decelerating Raman soliton, which normally occurs beyond several centimeters propagation distance.

The location of CR in the first stage is governed by the phase-matching condition [93]:

$$\sum_{n\geq 2} \frac{(\omega_{CR}-\omega_p)^n}{n!}\beta_n(\omega_p) = \frac{\gamma P_p}{2} \tag{5.14}$$

where ω_{CR} and ω_p are the central frequencies of CR and the input NIR pulse. βn represents the nth order derivative of the propagation constant taken at the frequency ω_p. γ and P_p denote the fiber nonlinear parameter and the pulse peak power, respectively. The diamond-marked blue curve in Figure 5.8 illustrates the calculated CR location as a function of the input pulse wavelength, assuming a 300 pJ input pulse of 10 fs length. As the input pulse centers at 800 nm, the curve predicts the CR to be located at 500 nm, in agreement with our experimental

observation [the curve labeled with 4 mm in Figure 5.9]. For comparison, the case neglecting nonlinear phase contribution (i.e., $P_p = 0$) is also plotted as the circle-marked green curve.

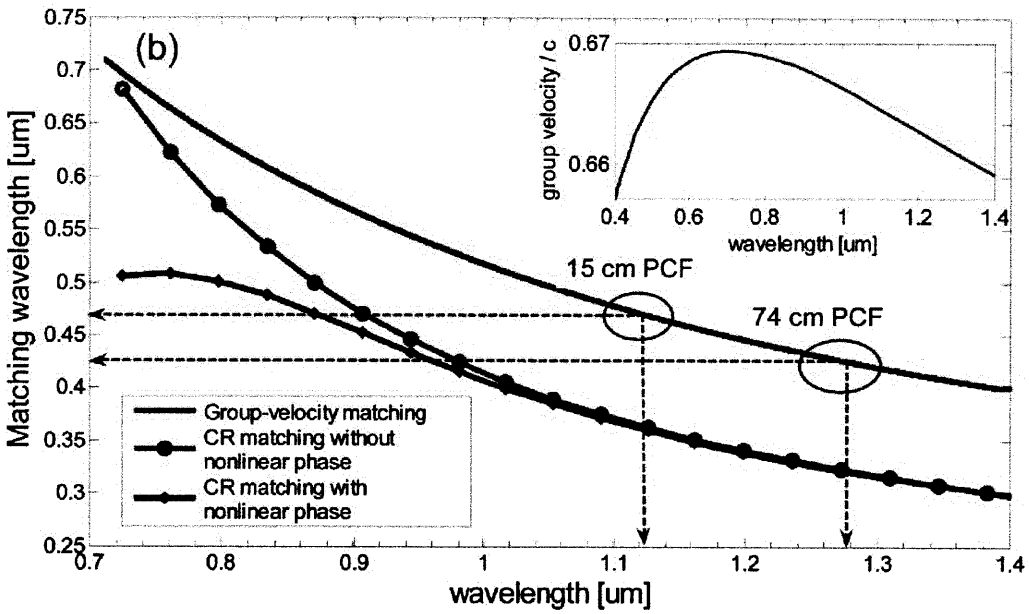

Figure 5.8 Phase-matching condition for CR and group-velocity matching. The matching points between the CR pulse and Raman soliton corresponding to 15 cm and 74 cm PCF are marked, respectively, to illustrate the trapping process. Inset shows the wavelength-dependent group-velocity normalized to the light speed in vacuum.

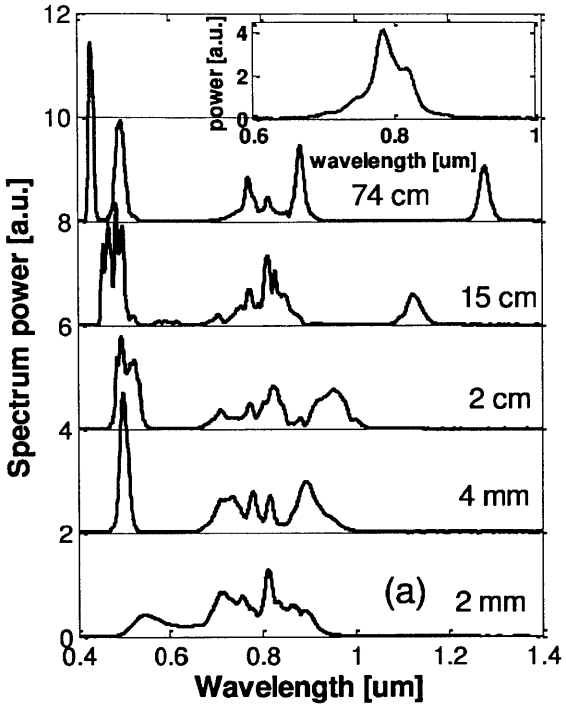

Figure 5.9 Evolution of FOCR spectrum with increased PCF length, labeled as 2 mm, 4 mm, 2 cm, 15cm, and 74 cm, respectively. The input pulse energy is fixed at 300 pJ. Inset shows the laser spectrum coupled into the fiber (i.e., the optical spectrum at the beginning of the PCF).

Figure 5.9 records the FOCR spectra generated by three PCFs with different lengths: 2 mm, 4 mm, 2 cm, 15 cm, and 74 cm; the input pulse energy coupled into these fibers is fixed at 300 pJ. While the coupled spectrum [inset in Figure 5.9] is not of hyperbolic shape, the experimental results well reproduce the main features of the three-stage evolution discussed before:

1) As expected for the case of a 2-mm PCF, a broadband continuum develops at the pump's short wavelength side—a signature for the first stage.

2) At the output of the 4-mm PCF, a narrowband (20-nm FWHM), isolated FOCR spectrum builds up; the resulting spectral recoil pushes the residual pump spectrum toward longer wavelength [see Fig. 1(d)]. The experimental FOCR spectrum is close to the theoretical prediction [inset (b) in Figure 5.5] in terms of FWHM bandwidth (20 nm vs. 23 nm) and spectral shape.

3) Emanating from the 2-cm PCF, the narrowband FOCR spectrum broadens to 50 nm due to its nonlinear propagation. SRS continuously red-shifts the residual pump spectrum, from which a Raman soliton gradually emerges. Before red-shifting to 1.05 μm, the Raman soliton travels faster than the FOCR pulse centered at 500 nm; no interaction exists due to the large temporal separation. The FOCR pulse carries ~40% of the input power.

4) With further propagation, the Raman soliton continues shifting towards longer wavelength and slows down. As the FOCR pulse eventually catches up with the decelerating Raman soliton, the evolution enters the fourth stage in which the Raman soliton traps part of the FOCR spectrum [the curve labeled with 15 cm in Figure 5.9]. Due to the continuous red-shifting of the Raman soliton, the group-velocity matching forces the captured FOCR spectrum to shift towards shorter wavelength accordingly. As a result, the FOCR spectrum splits into two well-separated parts [the curve labeled with 74 cm in Figure 5.9].

It is worth noting that the CR spectrum at the first several millimeters of the PCF manifests as a pulse about 15 fs long in the time domain. Self-phase

modulation experienced by such a short pulse during the second stage significantly broadens the CR spectrum and reshapes it into a rectangular shape [the curve labeled 2 cm in Figure 5.9] - a characteristic feature attributed to the interaction between self-phase modulation and normal dispersion. The large normal dispersion quickly stretches the pulse to ~1 ps long within several centimeters of propagation distance; self-phase modulation that is proportional to the pulse peak power becomes minimal. The spectrum bandwidth stays nearly constant until entering the next stage.

Also in the second stage, a Raman soliton forms at the long wavelength and redshifts, driven by stimulated Raman scattering. The interaction between the CR pulse and the Raman soliton relies on their group velocities [88], [94]. The inset of Figure 5.8 plots the wavelength dependent group velocity defined by the fiber dispersion. Such a quasi-parabolic curve permits two wavelengths matching the same group velocity. The non-marked, red curve in Figure 5.8 illustrates this group-velocity governed wavelength matching. Apparently, before red-shifting to 1:05 μm, the Raman soliton travels faster than the CR pulse centered at 500 nm; no interaction exists due to the large temporal separation. With further propagation, the Raman soliton continues shifting toward the longer wavelength and, therefore, slows down. As the CR pulse eventually catches up with the decelerating Raman soliton, the evolution enters the third stage, in which the Raman soliton traps part of the CR spectrum [the curve labeled with 15 cm in Figure 5.9]. Because of the continuous red-shifting of the Raman soliton, the group-velocity matching forces the captured CR spectrum to shift toward the shorter wavelength accordingly. As a

result, the CR spectrum splits into two well-separated parts [the curve labeled 74 cm in Figure 5.9]. The two circles on the group-velocity matching curve in Figure 5.8 denote the matched wavelengths for the Raman solitons generated in PCFs of 15 cm and 74 cm, respectively. These group velocity matched wavelengths are identified by the arrow pairs in Figure 5.9. The theoretical prediction and the experimental observation agree extremely well on the wavelength position of the trapped CR spectrum.

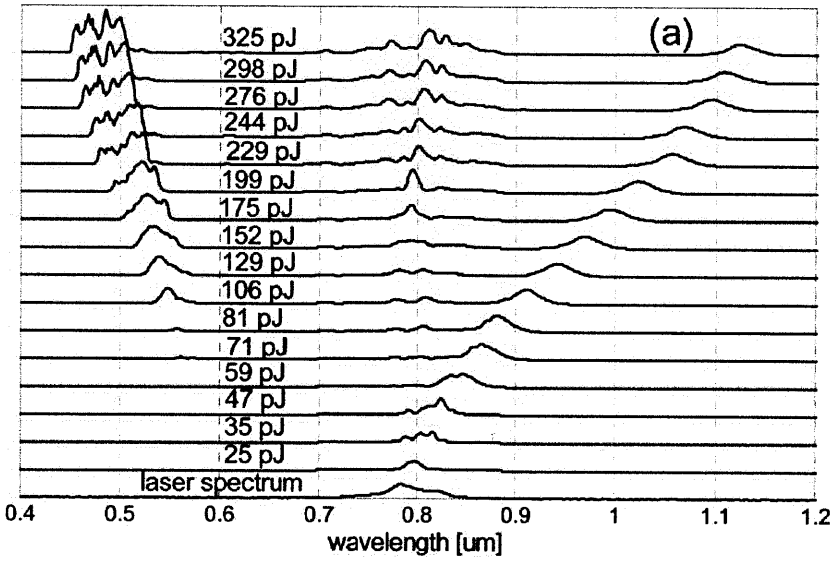

Figure 5.10 Evolution of CR and Raman solitonwith increased pulse energy for 15 cm PCF.

The phase-matching condition implies that the CR wavelength depends on the input pulse peak power (or input pulse energy when the pulse duration is fixed). Comparing the circle-marked green curve (phase-matching with nonlinear-phase contribution) with the diamond-marked blue curve (phase-matching neglecting nonlinear phase) in Figure 5.8 indicates that the CR locates at a shorter wavelength as we increase the input pulse energy. To verify this prediction, we adjusted input

pulse energies coupled into a 15 cm PCF and recorded the spectra as shown in Figure 5.10

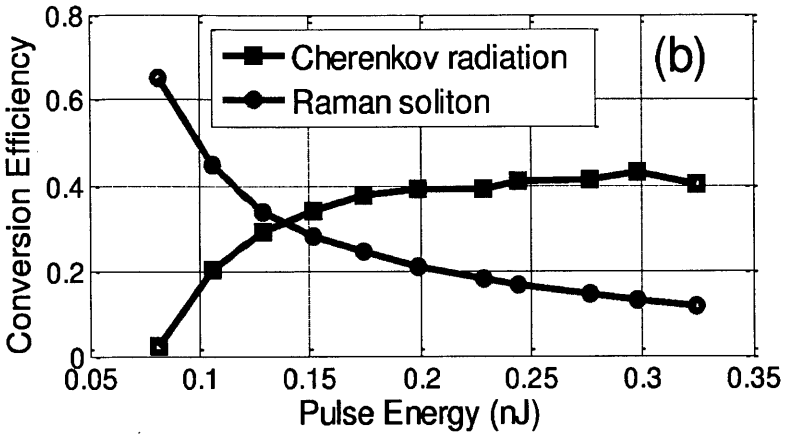

Figure 5.11 Conversion efficiency of CR and Raman soliton versus input pulse energy

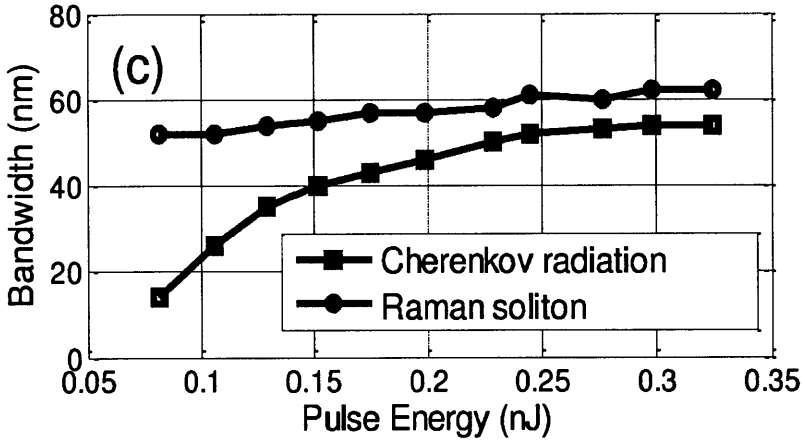

Figure 5.12 7 dB bandwidth of CR and Raman soliton versus input pulse energy.

As expected, the CR blueshifts with the increment of the input pulse energy. Figure 5.11 and Figure 5.12 summarize the conversion efficiency and 7 dB bandwidth of the CR pulse and Raman soliton. These data clearly revealed three distinct evolution regimes with respect to pulse energies: (i) below 70 pJ, no

distinguishable CR is observed, while a Raman soliton has developed; (ii) at 70–200 pJ, CR conversion efficiency and bandwidth grow dramatically with the spectrum approaching rectangular shape due to self-phase modulation and normal dispersion; and (iii) beyond 200 pJ, these two quantities (i.e., conversion efficiency and bandwidth) saturate and stay nearly constant. In this regime, a noticeable dip has developed in the middle of the CR spectrum and becomes deeper with increased input pulse energy—a signature indicating Raman soliton trapping. While its central wavelength undergoes steady redshift as the input pulse becomes stronger, the Raman soliton energy varies marginally, and, therefore, its conversion efficiency drops continuously, as shown in Figure 5.11. Additionally, the spectra in Figure 5.10 imply that the aforementioned "three fiber length scales" depend on input pulse energy.

Most importantly, the data of the above experiments have demonstrated that CR, when pumped with 10 fs pulses of more than 200 pJ pulse energy, exhibits high conversion efficiency (>40%), broad bandwidth (>50 nm), and low threshold (<100 pJ for pulse energy). These three merits allow achieving broadband visible-wavelength spectra from relatively low-energy ultrafast sources, which opens up new applications. For example, scaling up the repetition rate of a Ti:sapphire femtosecond oscillator beyond gigahertz is inevitably accompanied by low pulse energy (<1 nJ). A frequency comb based on such a gigahertz Ti:sapphire laser constitutes a crucial part (known as a "source comb") of an astro-comb that has recently emerged as a enabling tool for precision radial velocity observations [24]. The demonstrated low-threshold CR can efficiently convert such a NIR source

comb into its broadband counterpart at the visible-wavelength range. With a proper Fabry–Perot filtering cavity to increase the line spacing of the CR source comb, the resulting astro-comb of visible wavelength holds the promise to locate Earth-like extrasolar planets orbiting around stars similar to the Sun.

As the results in Figure 5.4 show, using few-cycle pulses to excite FOCR enhances its conversion efficiency, leading to a stronger FOCR pulse; the corresponding stronger nonlinearity eventually leads to a broader FOCR spectrum in the visible wavelength range. In other words, FOCR excited by few-cycle pulses allows achieving broadband visible-wavelength spectra from relatively low-energy ultrafast sources. For example, scaling up the repetition rate of a Ti:sapphire femtosecond oscillator beyond 1 GHz is inevitably accompanied by low pulse energy (<1 nJ). Such high repetition-rate sources are desired in many applications, such as frequency metrology, optical arbitrary waveform generation, and high speed A/D conversion, to name just a few. To demonstrate that FOCR in the few-cycle regime constitutes a powerful wavelength up-conversion tool to efficiently convert a NIR, GHz laser source into its broadband counterpart in the visible wavelength range, we switch to a home-built, 1 GHz Ti:sapphire oscillator as the pump source, centered at 0.83 μm with ~140 nm bandwidth and ~800 mW average power. Figure 5.13 presents the FOCR spectra generated by 10-cm PCFs with different ZDW, i.e., 710 nm, 735 nm, and 750 nm. The maximum powers coupled into these fibers are 210 mW, 250 mW, and 190 mW, respectively [see the figure legend that specifies each fiber's ZDW and coupled power]. The relatively low coupling efficiencies into these PCFs are due to chromatic dispersion caused by the

singlet coupling lenses. Higher coupled powers are expected if achromatic coupling lenses are employed. The FOCR spectrum, its center wavelength mainly determined by the phase-matching condition, shifts toward longer wavelength along with increasing the PCF's ZDW. Indeed, 10-cm length of PCF is enough to substantially slow down the Raman soliton (emerging from the residual pump) so that it has a considerable overlap with the FOCR pulse; the overlap-introduced XPM manifests as amplitude modulation onto the FOCR spectra shown in Figure 5.13. With 20-30% conversion efficiency, the resulting FOCR spectra, locating in the visible wavelength range, exhibit a bandwidth of 50-70 nm.

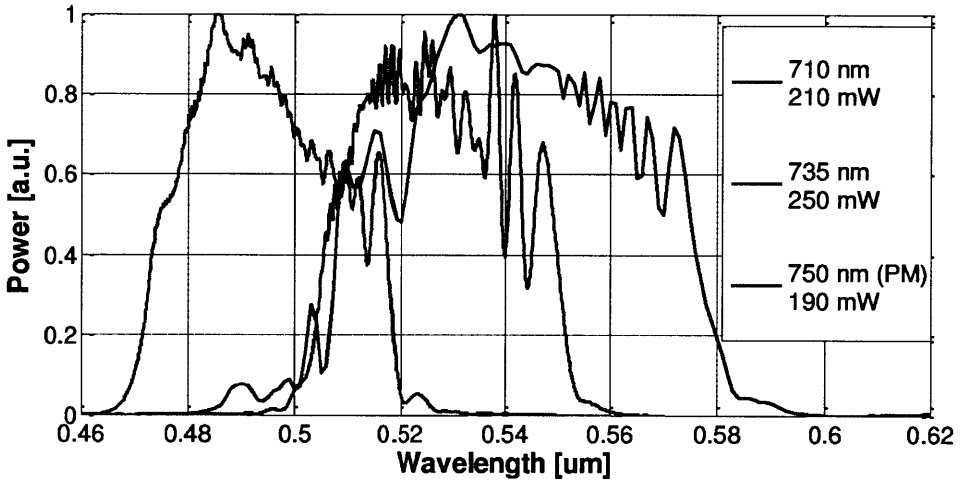

Figure 5.13 FOCR spectra generated by 10-cm PCFs with different ZDWs, i.e., 710 nm (red curve), 735 nm (green curve), and 750 nm (blue curve). The one with 750-nm ZDW is a polarization maintaining (PM) PCF.

Recent years have seen growing research interest in optimizing femtosecond-laser based frequency combs for astrophysical spectrograph calibration ("astro-combs") [24], [108–114]. Through precision radial velocity (PRV) observation, astro-combs hold the promise to enable the search for Earth-

like extra-solar planets (exoplanets), direct observation of cosmological deceleration, and the study of temporal variation of fundamental constants. Astro-combs in the visible wavelength range are of particular importance because, in this wavelength region (400-600 nm), emission from Sun-like stars provides the largest photon flux as well as high-quality spectral features most suited for PRV observation [115]. While astro-combs in the blue and green have been demonstrated via second harmonic generation of NIR source combs, they exhibit narrow bandwidth (2 nm for the green astro-comb and 15 nm for the blue [114]). In this scenario, the broadband, highly efficient, GHz FOCR in the few-cycle pulse regime emerges as a powerful wavelength up-conversion tool to implement a broadband astro-comb in the visible wavelength range. As a proof-of-concept, we have demonstrated a broadband green astro-comb using this method [116].

5.4. Discussion and conclusion

In this chapter, we have both theoretically and experimentally studied FOCR in the few-cycle regime, with a focus on its evolution before spectral splitting due to the decelerated Raman soliton. Although FOCR originates from $\chi^{(3)}$ nonlinear susceptibility of an optical fiber, its buildup and initial evolution resembles well-known $\chi^{(2)}$ nonlinear effects, such as second-harmonic generation, sum-frequency generation, difference-frequency generation, and optical rectification. A universal feature of these phenomena is that they all require phase-matching to achieve efficient power conversion. At the initial evolution stage of FOCR, its bandwidth is determined by phase-matching condition in a manner similar to $\chi^{(2)}$ nonlinear process; that is longer propagation leads to narrower bandwidth. Inspired by such a

resemblance, we have introduced the coherence length for continuum generation—a characteristic phenomenon only evident for FOCR in the few-cycle regime. Coherence length also elucidates the physical mechanism behind the formation of an isolated FOCR spectrum that builds up at the short wavelength side of the continuum and experiences spectral narrowing. Inside a $\chi^{(2)}$ medium, normally the effect of $\chi^{(3)}$ is negligible and spectral broadening due to SPM is absent. Therefore spectral bandwidth is nearly exclusively determined by the phase-matching condition. In contrast, after the spectral narrowing due to limited phase-matching bandwidth, FOCR is broadened as a consequence of nonlinear propagation. Such a nonlinear spectral broadening process is enabled by the high conversion efficiency achieved by exciting FOCR with few-cycle pulses.

In summary, we have demonstrated (both theoretically and experimentally) that FOCR in the few-cycle regime exhibits three unique features that are absent when pumped with often-used, long pulses: (1) continuum generation (may span one octave in connection with the pump spectrum), (2) high conversion efficiency (up to 40%), and (3) isolated FOCR spectra with broadband (70 nm experimentally obtained) coverage. Dependence of coherence length on fiber dispersion [see equation (5.8)] suggests that these three features can be engineered by tailoring the fiber's dispersion—a manufacturing flexibility readily provided by PCFs. For example, during the nonlinear propagation in which FOCR acquires more bandwidth, large normal dispersion quickly stretches the FOCR pulse up to hundreds of fs within a couple of centimeters, which dramatically reduces its peak power, weakens the nonlinear effects (e.g. SPM), and thus diminish the spectral

broadening. Apparently, such a pulse-stretching effect can be suppressed by reducing the amount of normal dispersion in the FOCR spectral region. Consequently, the strengthened nonlinear effects will enhance the spectral broadening process. Furthermore, a reduced normal dispersion increases the coherence length, implying that constructive addition between the existing FOCR and newly emitted radiation takes place within a longer propagation distance. As a result, more input energy transfers to the FOCR, giving rise to an even higher conversion efficiency, which in turn benefits FOCR's spectral broadening.

Chapter 6

Toward Higher Repetition Rates: Broadband Filtering Cavity

6.1. Motivations

Dielectric coatings with custom reflectivity and group-delay dispersion (GDD) over a desired spectral range are key components in ultrafast optics. With powerful computer-based optimization algorithms, one can explore a multi-dimensional design space (constructed by the choice of material and layer thickness) and create sophisticated coating designs for the manipulation of laser pulses of various durations or spectral coverage. For example, incorporation of broadband double-chirped mirrors (DCMs) [33–35] into mode-locked Ti:sapphire lasers for precise GDD compensation has been used for achieving octave-spanning spectra directly from a laser cavity [37], [42], [49], [68], [70], [71]. Compression of ultrabroadband laser pulses down to sub-two cycles using dispersion-compensating mirrors with a bandwidth spanning over 1.5 octaves has been recently demonstrated [117]. With both their pulse repetition rate and carrier-envelope phase stabilized, these lasers become frequency combs, whose spectra are composed of many narrow and

equally spaced optical lines. In addition to precision frequency metrology [118], frequency combs have found more applications via short pulse field enhancement or repetition-rate multiplication with the aid of high-finesse optical cavities. For short pulse field enhancement, the equally-spaced spectral lines of a frequency comb are coupled into a cavity with a free-spectral range (FSR) matched to the laser pulse repetition rate, which constructively enhances the resonant pulse circulating inside the cavity without the need of active amplification. This enhancement technique has been used in the facilitation of high harmonic generation driven by high repetition-rate (i.e. ~ 100 MHz) lasers, enabling the generation of EUV frequency combs [119]. If gaseous samples are introduced into the cavity, the effective interaction length between light and sample can be increased by many orders of magnitude, leading to an unprecedented high sensitivity in spectroscopy [120]. For repetition-rate multiplication, the cavity FSR is tuned to be an integer multiple of the source-comb spectral line spacing and the cavity acts as a filter that selectively suppresses unwanted lines and passes those aligned with the cavity's narrow transmission resonances. The resulting filtered comb can be spatially resolved by spectral dispersers so that individual spectral lines become accessible and controllable. Rarely achieved from fundamentally mode-locked solid-state lasers, such high repetition-rate sources are essential for many applications such as arbitrary optical waveform generation through line-by-line modulation [23] and precision wavelength calibration of astrophysical spectrographs for the detection of Earth-analogous extra-solar planets (the resulting filtered comb is often called an astro-comb) [24], [109], [110].

One crucial requirement of the optical cavity is to have wavelength independent FSR, or equivalently wavelength independent round trip optical length over a broad bandwidth to ensure that the frequencies of the transmission resonances are aligned with equally-spaced frequency comb lines, which can be achieved by designing a broadband zero-dispersion cavity. For short pulse field enhancement, the cavity bandwidth limits the transform-limited pulse duration as well as the peak intensity of the circulating pulses. In the astrophysical spectrograph calibration, the cavity bandwidth limits the available wavelength coverage and thus compromises the calibration accuracy. Currently, most of the enhancement or filter cavities are constructed from dielectric mirrors that are individually designed to have negligible dispersion or compensate the GDD of intracavity materials at a certain wavelength range. In this paper, we demonstrate a novel design for an optical cavity that consists of a set of dielectric mirrors with zero GDD in reflection, which allows optimization of many mirrors simultaneously to extend cavity bandwidth. The design concept, optimization algorithm, and tolerance to manufacturing errors for such zero-GDD mirror sets are also discussed. As an example, we present our design and experimental demonstration of the first zero-GDD mirror pair with 100-nm bandwidth (480-580 nm) and ~99.2% reflectivity using Nb_2O_5/SiO_2 layer pairs. This mirror pair is designed for construction of a Fabry-Perot (FP) filter cavity with 40 GHz FSR, a pivotal device for implementing a broadband astro-comb in the visible wavelength range. The demonstrated cavity, for the first time, has successfully transformed a 1 GHz green comb into an astro-comb spanning over 100nm bandwidth.

6.2. Zero-GDD Mirror Set: Design Concepts

As a linear closed-loop system, a passive optical cavity can be modeled in a lumped way with its loop transfer function $H(\omega)$ determined by all cavity mirrors and intracavity materials per round-trip. The magnitude $|H(\omega)|$ is the accumulated amplitude decay ratio and the phase shift $\varphi(\omega)=\angle H(\omega)$. Assuming that an input field is coupled into the cavity and propagating to a certain reference plane, the power spectrum of the circulating pulse at that plane is scaled by the following closed-loop transfer function:

$$\left|\frac{1}{1-|H(\omega)|e^{j\varphi(\omega)}}\right|^2 \tag{6.1}$$

For a passive high-finesse cavity, $|H(\omega)|$ is close to but less than one. Inside the cavity, resonant frequencies, corresponding to $\varphi(\omega)$ being a multiple of 2π, are significantly enhanced. From a simple physical viewpoint, this phase shift originates from the required round-trip time for the light at a certain wavelength. When the round-trip time is wavelength-independent, $\varphi(\omega)$ becomes simply a linear function of ω. Therefore, the resulting resonances are equally spaced in the frequency domain. By careful adjustment of the cavity length and eventually also the carrier-envelope offset frequency of the laser, these resonant frequencies can be tuned to align with frequency comb lines. However, due to the cavity dispersion, the non constant mode spacing causes a mismatched cavity. The tolerance against residual dispersion depends on the cavity finesse. As $|H(\omega)|$ approaches a high finesse cavity, i.e. $|H(\omega)|\rightarrow 1$, the closed loop transfer function is more sensitive to the phase, and the resulting tolerance to dispersion-induced deviations in mode

spacing caused by phase deviations becomes smaller. In other words, even a small phase deviation from a multiple of 2π can lead to a dramatic decrease in the cavity's transmission for frequencies around resonances. One can derive a simple criterion for estimating this phase tolerance by solving for the phase corresponding to half of the maximum of (6.1) and find:

$$\varphi(\omega) < \frac{1-|H(\omega)|}{\sqrt{|H(\omega)|}} \approx 1-|H(\omega)| \text{ , for } |H(\omega)| \approx 1 \tag{6.2}$$

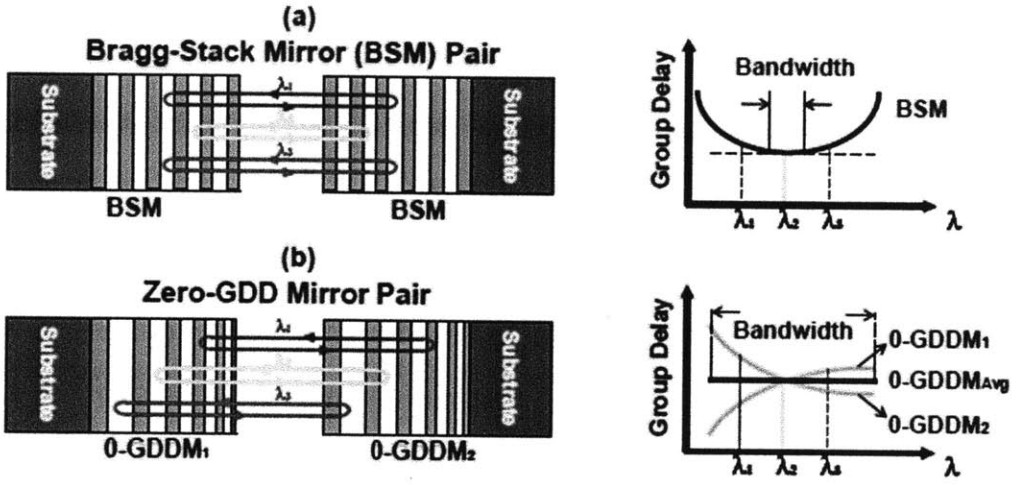

Figure 6.1 Schematic of the two-mirror dispersion-free cavity based on (a) Bragg-stack mirror pair and (b) zero-GDD mirror pair. The curves on the right show the individual and average group delay on the cavity mirrors as a function of wavelength.

For example, to design a dispersion-free Fabry-Perot cavity consisting of two identical mirrors with a reflectivity of 99%, one needs to ensure the dispersion-induced phase deviation is less than 0.01 radian within the desired wavelength range. For applications demanding less distortion on the filtered comb lines, this value could be even smaller.

In the traditional cavity designs, low-dispersion mirrors based on Bragg-stack mirrors (BSMs) are commonly used, as shown in Figure 6.1. Although BSMs are typically high reflectors with a moderate bandwidth, different wavelengths reflects from different depths inside the structure. Consequently, only a narrow spectral range near the center of the high-reflectivity region experiences negligible dispersion, imposing limitations on effective cavity bandwidth. In practice, slight optimization is usually required to broaden the usable bandwidth of such BSM-based, low-dispersion mirrors, but the possible improvement is very limited. In addition, any uncompensated dispersion from intracavity materials causes further bandwidth narrowing. As a result, it is often necessary to put the cavity in vacuum to avoid air dispersion. In this sense, any individual component with non-zero dispersion is limiting the cavity bandwidth. However, the real bottleneck, as discussed earlier, is the cavity round-trip time. A constant round-trip time for the wavelengths of interest does not imply that they have to travel at the same speed. Instead, as we will show in the following sections, allowing some dispersion on the mirror coating provides additional degrees of freedom to design cavity mirror sets for broadband cavities. This idea is illustrated in Figure 6.1 (b) with a simple mirror pair shown as an example. Note that the concept can be easily generalized to a mirror set including even more mirrors. As plotted in the figure, the layer thicknesses of the mirror pair are chirped to create a complementary, wavelength-dependent penetration depth in both mirror coatings. With the total dispersion minimized, such a mirror pair constitutes a dispersion-free building block for optical cavities. Compared to individually-optimized BSM cavities, this approach

excels because chirped-mirrors intrinsically have larger bandwidth and more flexibility for dispersion customization, which creates a larger parameter space for extending the bandwidth of dispersion-free cavities. Another advantage of optimizing a mirror set instead of individual mirrors is that the intracavity material dispersion can be easily taken into account in the design process. For a complicated multi-mirror cavity, mirror sets can even be designed to provide additional features such as transmission windows at specific wavelengths to meet the application requirements. Eventually, the cavity can use one or more zero-GDD mirror sets with all the necessary features without significant bandwidth reduction. In short, zero-GDD mirror sets are a set of mirrors jointly optimized to provide custom reflectivity and negligible dispersion over a large bandwidth. Also, depending on the application, additional characteristics can be implemented during the design process.

6.3. Optimization Algorithm and Design Issues

The design of a zero-GDD mirror set is based on the efficient group-delay (GD) computation approach developed in Ref. [78]. The optimum layer thicknesses are found by minimizing the merit function that evaluates the weighted deviation of the computed dispersion and reflectivity from our design goal. The wavelength range of interest is discretized into k points, denoted as λ_k. The employed merit function is simply determined by the summation of the weighted deviation from the targeted reflectivity and GD values corresponding to the thicknesses of the layer set x:

$$f(x)=\sum_k \left\{\omega_R(\lambda_k)\left[R(\lambda_k;x)-R_{goal}(\lambda_k)\right]^4+\omega_d(\lambda_k)\left[\tau_g(\lambda_k;x)-\tau_{g,goal}(\lambda_k)+\tau_{g0}(x)\right]\right. \quad (6.3)$$

where R is the reflectivity, τ_g the group delay, and $\omega_{R,d}$ the weighting function for the reflectivity and GD goals. The term τ_{g0} is used to exclude the irrelevant offset between the computed and ideal GD, which minimizes f(x) for a given layer set x. To find good initial structures to start with, we first optimize all mirrors separately using smooth GD functions split from a GD goal that is complementary to the dispersion of the materials. This ensures that the remaining errors are mostly from higher-order dispersion. In the second step the residual dispersion is minimized with an iterative optimization procedure in which all the mirrors are optimized in turns. The requirement of a constant round-trip time is implemented in this step by updating the GD goal of the mirror to be optimized with the computed GD of all other mirrors and the materials:

$$\tau_{g,goal}^{k}(\lambda_k) = -\sum_{i \neq k} \tau_g^i(\lambda_k; x^i) - \tau_g^{material}(\lambda_k) \tag{6.4}$$

The iteration continues until the target specification is reached. Theoretically, an ultrabroadband (e.g., 650-1100nm) zero-GDD mirror set can be produced using this algorithm by designing a complementary double-chirped mirror pair, with one mirror having the opposite average dispersion of the other one. In practice, broadband highly dispersive mirror designs demand higher precision in fabrication, a requirement ultimately limited by the capability of current coating technology. The increased sensitivity stems simply from the increased penetration depth of the light into the mirror giving rise to spurious reflections. The deeper the penetration the more opportunity there is for such reflections to occur. As a result, it is always necessary to confirm the robustness of a practical design by adding

random thickness perturbations to each layer, imitating manufacturing errors; and to estimate the resulting phase errors for worst-case scenarios.

6.4. Design Examples: Two-mirror Zero-GDD Mirror Pair for a Green (480-580 nm) Filtering Cavity

To demonstrate the idea, we have designed a zero-GDD mirror set consisting of a complementary mirror pair supporting a dispersion-free region from 480-580 nm. This zero-GDD pair is aimed for a moderate-finesse (>250) FP filtering cavity, as used in a green astro-comb. Astro-combs that cover spectral bands in the green (480 nm – 580 nm) are of particular interest in high accuracy astronomical spectroscopy because this wavelength region provides the largest photon flux from sun-like stars and is rich in spectral features of high quality. Charge-coupled devices (CCDs) used in astrophysical spectrograph also have better response in this wavelength region. Recently, we have demonstrated a blue astro-comb (410 nm – 425 nm) [114] based on a frequency-doubled 1 GHz Ti:sapphire frequency comb filtered by a FP cavity. Limited by the bandwidth of the phase matching of the frequency doubling process in a 1 mm thick beta-barium borate (BBO) crystal, the blue astro-comb has a bandwidth of only 15 nm, which is slight narrower than the transmission bandwidth of the FP cavity (20nm) made with two identical, individually-optimized low-dispersion mirrors. In order to design more powerful astro-combs that span much larger bandwidths using our recently-developed broadband visible source [101], [121], we constructed a broadband dispersion-free cavity using a zero-GDD mirror pair. Figure 6.2 shows the calculated reflectivity

and group delay of the zero-GDD mirror pair designed for a ~40 GHz FSR cavity.

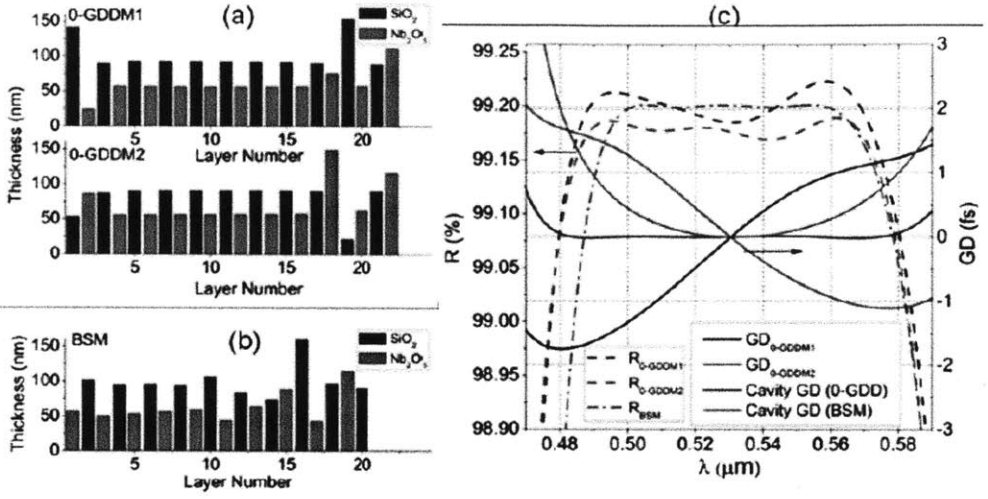

Figure 6.2 Structure of a two-mirror zero-GDD mirror set designed for a 40GHz FSR, 100 nm bandwidth (480-580 nm) cavity using Nb2O5/SiO2 layer pairs. (b) Structure of a low-dispersion BSM mirror that is individually optimized for the same goal. (c) Calculated reflectivity (dotted curves) and group delay (solid curves) of the zero-GDD mirror pair. The total cavity group delay using the zero-GDD mirror pair (blue) is calculated by taking the dispersion of both mirrors and 7.5 mm of air into account. As a comparison, the total GD (solid) and reflectivity (dashed) of a cavity in vacuum based on two individually-optimized, low-dispersion BSMs is shown in green.

The dispersion caused by 7.5 mm of intracavity air (~0.24 fs^2 for 1 atmosphere at 300 K) is taken into account during the optimization. With an initial structure of 22 layers of Nb2O5/SiO2 quarter-wave layer pairs, both mirrors are optimized to have a reflectivity of ~99.2% and complementary dispersion over the desired range (Figure 6.2 (a)), which supports a FP filtering cavity with a finesse of ~390. For comparison, we also designed a similar low-dispersion mirror centered at 530 nm based on the traditional approach, i.e. individually-optimized BSMs (Figure 6.2 (b)). In Figure 6.2 (c), we compare the calculated total GD of the FP cavities built with both designs and find a three-fold bandwidth improvement with the new zero-GDD mirror set design even when the traditional design is evaluated for a

cavity in vacuum. Such improvement is due to the simultaneous optimization of the mirrors of the zero-GDD set.

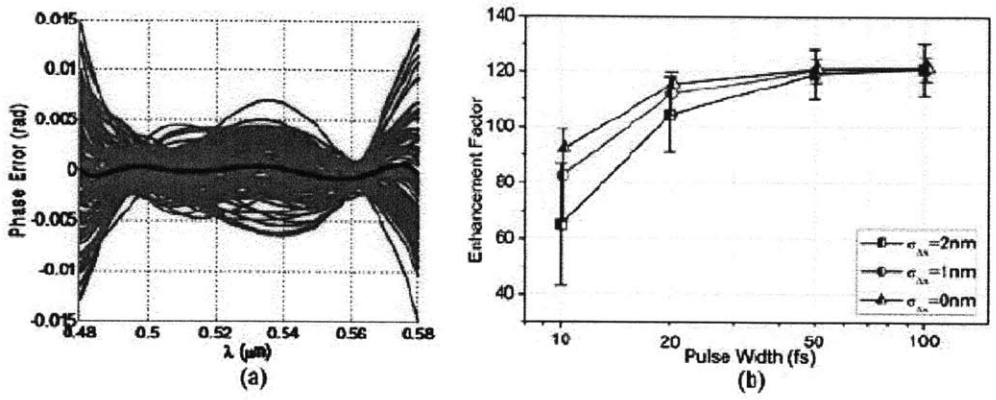

Figure 6.3 Simulated phase deviation from a dispersion-free cavity using one zero-GDD mirror pair. The deviation of the ideal zero-GDD mirror pair design is shown in black and the spread of possible phase errors with 100 tests assuming a random manufacturing error of ± 0.5 nm for the mirror layer thicknesses is shown in red. (b) Estimated enhancement factors for 100, 50, 20 and 10 fs Gaussian pulses considering normally-distributed manufacturing errors with a standard deviation σ_x of = 0 (blue), 1 (red), and 2 nm (black). Each marker indicates shows the average value and the error bar show the standard deviation of enhancement factor for 1000 tests.

As mentioned in the previous section, the bandwidth can be even larger if the structures are more chirped. However, this will inevitably degrade the manufacturability of the mirrors and causes uncertainty for astro-comb applications that demand extremely low phase error. As a result, we used quarter-wave layer pairs, identical to the traditional design, as the initial structure for optimizing the zero-GDD mirror set, a conservative design that improves robustness to manufacturing errors. Figure 6.3 (a) illustrates the simulated phase deviation from a zero-dispersion cavity using the zero-GDD mirror pair shown in Figure 6.2 (a) with manufacturing thickness errors taken into account. The analysis is performed with 100 tests assuming random layer thickness fluctuations of ± 0.5 nm on each layer of

both mirrors. The spread of possible round-trip phase errors confirms that the criterion (2) is fulfilled in the presence of reasonable manufacturing tolerances.

We also performed another analysis on our zero-GDD mirror pair to show that it can also be applied to broadband pulse enhancement in the few-cycle pulse regime. We simulated the enhancement factor for 100, 50, 20 and 10 fs Gaussian pulses with the central wavelength matched to the cavity. Normally-distributed random thickness errors with a standard deviation σ_x of 0, 1, and 2 nm were added to each layer. The enhancement factor was obtained by calculating the peak intensity of the steady-state intracavity pulse normalized to the input pulse. With 1000 tests on each combination of pulse duration and manufacturing tolerances, we obtained the average enhancement factor and its standard deviation (Figure 6.3 (b)). The result clearly indicates that the enhancement factor approaches the theoretical limit even for relatively low accuracy in fabrication (σ_x = 2 nm); an average enhancement factor of ~100 can be achieved for transform-limited pulses as short as 20 fs. For applications requiring ultra-high peak intensity from cavity-enhanced femtosecond lasers, laser-induced damage threshold (LIDT) is a critical issue. However, in the subpicosecond regime LIDT does not scale linearly with the pulse duration τ but proportional to τ_x, where $x < 0.5$ [122]. For extremely high intensity experiments, however, special cavity designs [123], [124] and high damage threshold coating materials are necessary.

6.5. Proof-of-concept Experiment: 45 GHz Filtering Cavity

As a proof-of-concept experiment, we first constructed a tunable light source in the visible wavelength range using Cherenkov radiation from a photonic crystal fiber (PCF). When pumped by ultrashort pulses (~10 fs), this mechanism becomes a low-threshold nonlinear process for broadband, highly efficient optical frequency up-conversion [12]. Figure 6.4 (a) shows the experimental setup. An octave-spanning Ti:sapphire laser operating at 1 GHz repetition rate pumped a PCF with a zero-dispersion wavelength at 710 nm (NL-1.8-710). An achromatic half-wave plate and several bounces from broadband dispersion compensating mirrors were employed to optimize the polarization and duration of the input pulses. With ~200 pJ of coupled pulse energy, the PCF emits in the visible wavelength range covered by the designed mirror bandwidth. Figure 6.4 (b) shows the spectra before and after a ~40 GHz dispersion-free filtering cavity, measured with a low-resolution spectrometer. The filtering FP cavity consisted of the zero-GDD mirror coatings on slightly wedged flat substrates for avoiding etaloning effects. The measured laser spectrum is nearly undistorted after passing through the cavity, demonstrating successful filtering over the entire bandwidth of the zero-GDD mirror pair. The detailed spectrum (see inset plot), acquired with an optical spectrum analyzer (OSA) further confirms that the individual comb lines become resolvable after filtering. The measured linewidth of the resolved comb lines was limited by the OSA, which has a resolution of ~20 GHz.

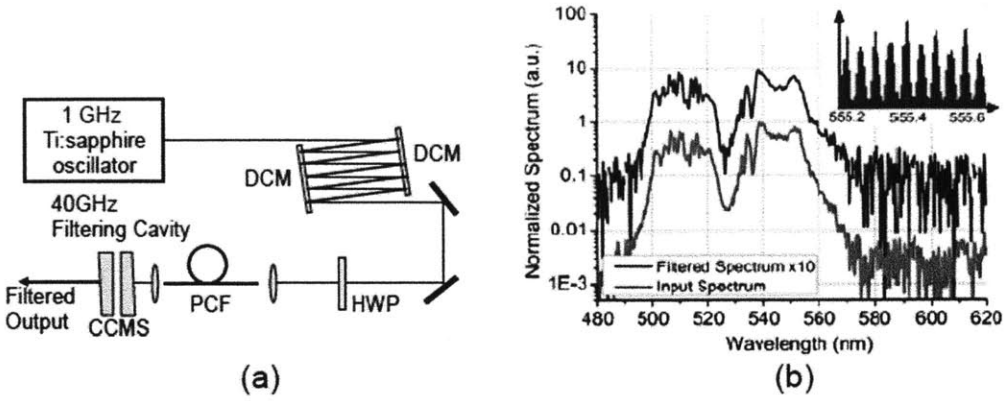

Figure 6.4 Experimental setup for generating a 40 GHz green astro-comb for astronomical spectrograph calibration. DCM: doubled-chirped mirrors for dispersion compensation; HWP: half-wave plate; PCF: photonic crystal fiber. (b) Input (black) and output (red) spectra before and after the 40 GHz FP filter cavity based on a zero-GDD mirror pair; inset shows detailed output spectrum near 555.4 nm obtained with a high resolution (~20 GHz) optical spectrum analyzer.

6.6. Summary

In conclusion, we have proposed and demonstrated a new approach for broadband dispersion-free optical cavities using a zero-GDD mirror set; e.g., to enable laser frequency combs for pulse repetition-rate multiplication and pulse enhancement. With a first zero-GDD mirror pair design, the construction of a ~40 GHz filtering cavity with 100 nm bandwidth for a green astro-comb (480-580 nm) was demonstrated. By proper structure scaling and re-optmization, the spectral coverage of the zero-GDD mirror set can be easily shifted to other wavelength. Further performance improvement can also be achieved by using better manufacturing techniques or materials with higher refractive index contrast since the intrinsic bandwidth of dielectric mirrors is proportional to $(n_{HL}\text{-}1)/(n_{HL}\text{+}1)$, where n_{HL} is the ratio of higher refractive index to lower index of the dielectric materials. We

believe this technique can also enable many other frequency-comb-based applications that demand large comb spacing or high peak intensity.

Chapter 7

Future Work

This dissertation presents a series of studies on soft-aperture KLM Ti:sapphire lasers operated in the few-cycle regime where complicated spatiotemporal mode-locking dynamics occurs. The principles of the laser design regarding spatial arrangement of laser components, dispersion management in the laser cavity, and choice of operating points have been addressed in details. Based on these guidelines, octave-spanning Ti:sapphire lasers operated at various repetition rates have been demonstrated. With the numerical model developed in this dissertation, many unique features that were only observed from the experiments can now be successfully simulated for the first time. This model should not only be used for studying the intracavity pulse dynamics but also as a tool incorporated during the laser design procedure for engineering the spectral features of the output pulse needed by different applications. Today, few-cycle lasers are still considered as sophisticated laboratory tools that need frequent maintenance by people with extensive laser knowledge. In order to make these lasers more user-friendly for researchers from different fields, several practical issues related to the construction

of an easy-to-operate, long-term stable few-cycle Ti:sapphire laser will be discussed to conclude this dissertation.

7.1. Laser Spectrum and Spatial Mode Engineering

The performance of few-cycle lasers is highly sensitive to the dispersion and loss properties of the optics used in the cavity. In the past, the focus of laser optimization was mainly on designing laser optics for achieving least residual phase caused by the cavity dispersion over a large bandwidth. As a result, ultrabroadband DCMs and output couplers are often used in few-cycle lasers. However, as shown from the simulation, dispersion-free cavities are not always ideal for generating broadest spectra. Since the Ti:sapphire crystals only provides a finite gain bandwidth, obtaining spectral power at the wavelengths far away from the gain peak through the amplification process is not efficient. In order to enhance the power at the desired spectral wings, using phase-matching techniques as described in section 3.5.6 turns out to be a better solution. The ideal phase-matching condition is met when the nonlinear phase is equal to the linear phase contributed by the dispersion per round-trip, which confines the enhancement in the fundamental transverse mode of the cavity. In practice, one can incorporate such conditions into the laser coating design by optimizing the phase instead of group delay or group delay dispersion provided by the coating for creating a phase difference corresponding to the nonlinear phase per round-trip between the laser central wavelength and the desired wavelengths. This additional feature can be provided by one or many laser mirrors dedicated to different applications.

7.2. Hands-off Operation

Even though few-cycle lasers are powerful scientific tools in the laboratory, they are currently too immature to be reliable industrial products. In order to let people without extensive experiences use these lasers, they must be constructed in a robust way and allow long-term hands-off operation. To achieve this goal, stable mechanical design must be implemented with excellent rejection to environmental disturbances such as vibrations or temperature fluctuation since few-cycle laser are more vulnerable to cavity misalignment comparing to long-pulse mode-locked lasers. Moreover, the cavity needs to be assembled and sealed in a clean environment to avoid contamination. The position of critical components such as gain crystal, pump lens, and curved mirrors should be adjusted with encoded translation stage to keep track of the operating point of the laser. When operating the laser, the performance should be continuously monitored in order to prevent fatal failures. The goal of these protection and monitoring approaches is to minimize the chance for the laser to drift away from a working operating point.

7.3. Crystal Damage Issue

It has been found that the crystal damage is a serious issue in building long-term stable few-cycle lasers. This problem becomes more severe when the laser is closer to the octave-spanning operation. For octave-spanning lasers operated at low repetition rate (<100 MHz), noticeable performance degradation is usually observed within a few hours to one day of continuous operation. Such degradation often comes with increasing pump beam scattering from the crystal surface. If the crystal surface is immediately cleaned when the laser output power starts to

degrade, the laser might be able to regain its original performance. However, if the laser keeps running without cleaning, the damage might become permanent and eventually the user might not be able to recover the laser performance without changing the active spot on the crystal surface. Figure 7.1 (a)-(c) show the microscope image of the active zone on the crystal surface with different level of damage. In Figure 7.1(a), the crystal surface is coated with certain contaminants with a small burn spot in the middle. In Figure 7.1(b), a large portion of surface contaminants is burned. In Figure 7.1 (c), the burned area is turned into permanent surface damage that cannot be removed with cleaning. Right now, it is not yet clear what kind of material is in the contaminated area. A reasonable guess for the sources of contamination are floating dust particles in free-space or from outgassing of materials used on the mechanical components. These contaminants are carried, eventually also decomposed and coated onto the crystal surface by the strong laser beam that functions like an optical tweezer. Once the crystal is coated with the contaminants to a high degree, the contaminants are burned into the surface by the laser beam and permanent damage is created. The accumulation rate of contaminants is usually slow which agrees with experimental observations. As shown in Figure 7.2, these contaminants can be removed with careful cleaning before critical damage occurs. Right now, only little attention has been paid on tracing the sources of contamination and means to keep them away from the laser cavity. However, this must be done if one wants to turn such laser systems into a reliable tool. In addition to the failure mode described above, there is another mode of crystal damage that occurs on a shorter time-scale in few-cycle lasers. It is found

that the crystal damage might happen when the mode-locking is initiated. In this failure mode, a different damage pattern showing a huge hole surrounded by microcracks on the crystal is produced. As shown in Figure 7.2 (d), the diameter of the damaged spot is about 10 times larger than the contaminated area in the other three pictures and can even be seen with the naked eye. The physics behind this damage process is not clear yet. It might be induced by the high-intensity transients during the mode-locking process. To confirm these hypotheses, further study needs to be done in the future.

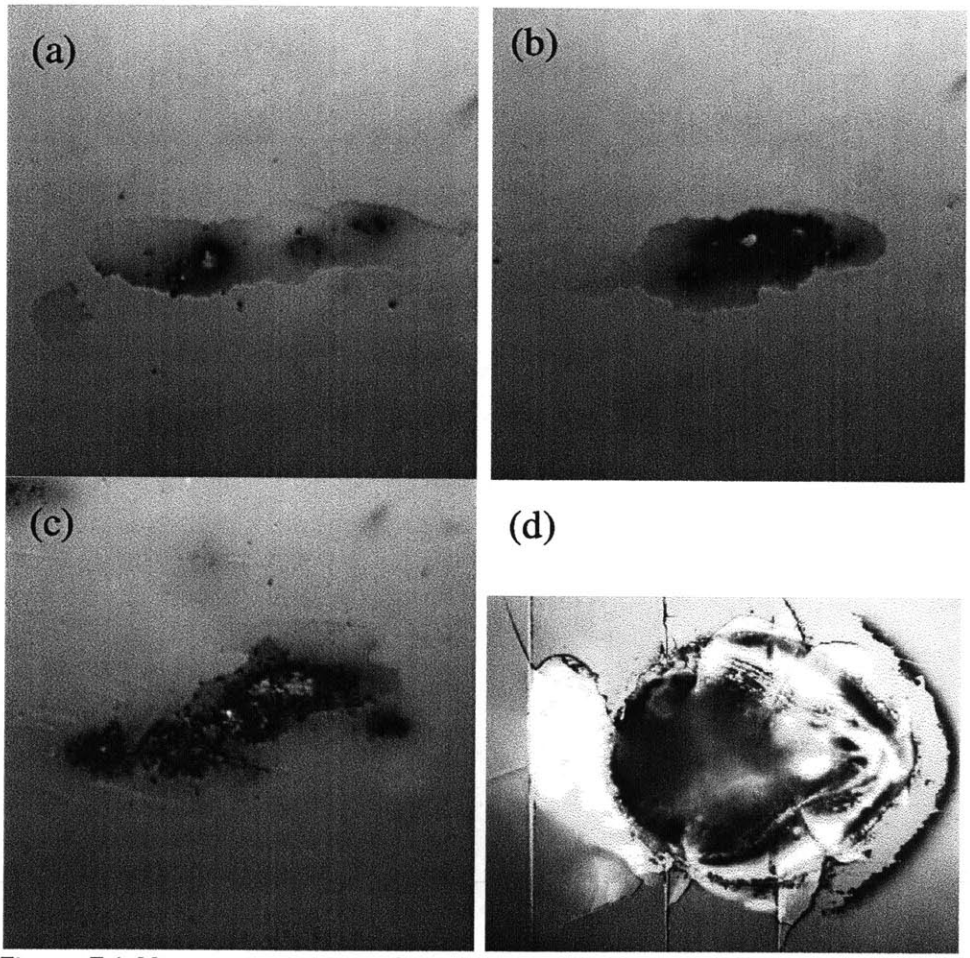

Figure 7.1 Microscope images of Ti:sapphire crystal surface showing different level of crystal damage. (a) crystal surface is coated with contaminates with a small burn spot in the middle. (b) a large portion of surface contaminates is

burned. (c) The burned area is turned into permanent surface damage that cannot be removed with cleaning. (d) A severe damage showing a large hole surrounded by many microcracks on the crystal surface. (Note: the diameter of damaged spot is about 10 times larger than the contaminated area in the other three pictures. The microcracks can be seen with the naked eye.)

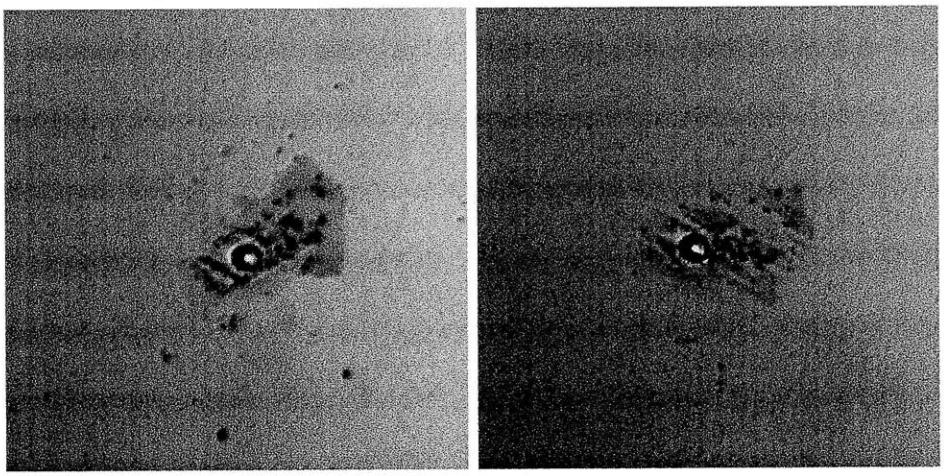

Figure 7.2 Microscope image around a damaged spot on the crystal (left) before cleaning and (right) after cleaning.

Bibliography

[1] L. E. Hargrove, R. L. Fork, and M. A. Pollack, "LOCKING OF He-Ne LASER MODES INDUCED BY SYNCHRONOUS INTRACAVITY MODULATION," *Applied Physics Letters*, vol. 5, p. 4, 1964.

[2] A. Yariv, "Internal Modulation in Multimode Laser Oscillators," *Journal of Applied Physics*, vol. 36, no. 2, pp. 388-391, Feb. 1965.

[3] G. R. Huggett, "MODE-LOCKING OF CW LASERS BY REGENERATIVE RF FEEDBACK," *Applied Physics Letters*, vol. 13, p. 186, 1968.

[4] D. Kuizenga and A. Siegman, "FM and AM mode locking of the homogeneous laser--Part I: Theory," *IEEE Journal of Quantum Electronics*, vol. 6, no. 11, pp. 694-708, Nov. 1970.

[5] D. Kuizenga and A. Siegman, "FM and AM mode locking of the homogeneous laser--Part II: Experimental results in a Nd:YAG laser with internal FM modulation," *IEEE Journal of Quantum Electronics*, vol. 6, no. 11, pp. 709- 715, Nov. 1970.

[6] M. Crowell, "Characteristics of mode-coupled lasers," *IEEE Journal of Quantum Electronics*, vol. 1, no. 1, pp. 12- 20, Apr. 1965.

[7] H. W. Mocker and R. J. Collins, "MODE COMPETITION AND SELF-LOCKING EFFECTS IN A Q-SWITCHED RUBY LASER," *Applied Physics Letters*, vol. 7, p. 270, 1965.

[8] E. P. Ippen, C. V. Shank, and A. Dienes, "Passive mode locking of the cw dye laser," *Applied Physics Letters*, vol. 21, no. 8, pp. 348-350, Oct. 1972.

[9] A. J. DeMaria, "SELF MODE-LOCKING OF LASERS WITH SATURABLE ABSORBERS," *Applied Physics Letters*, vol. 8, p. 174, 1966.

[10] H. A. Haus, "Theory of mode locking with a fast saturable absorber," *Journal of Applied Physics*, vol. 46, p. 3049, 1975.

[11] K. Sala, M. Richardson, and N. Isenor, "Passive mode locking of lasers with the optical Kerr effect modulator," *IEEE Journal of Quantum Electronics*, vol. 13, no. 11, pp. 915- 924, Nov. 1977.

[12] H. A. Haus, J. G. Fujimoto, and E. P. Ippen, "Structures for additive pulse mode locking," *Journal of the Optical Society of America B*, vol. 8, no. 10, pp. 2068-2076, Oct. 1991.

[13] E. P. Ippen, "Principles of passive mode locking," *Applied Physics B Laser and Optics*, vol. 58, pp. 159-170, Mar. 1994.

[14] R. L. Fork, "Generation of optical pulses shorter than 0.1 psec by colliding pulse mode locking," *Applied Physics Letters*, vol. 38, p. 671, 1981.

[15] W. Dietel, E. Döpel, D. Kühlke, and B. Wilhelmi, "Pulses in the femtosecond range from a cw dye ring laser in the colliding pulse mode-locking (CPM) regime with down-chirp," *Optics Communications*, vol. 43, no. 6, pp. 433-436, Nov. 1982.

[16] D. E. Spence, P. N. Kean, and W. Sibbett, "60-fsec pulse generation from a self-mode-locked Ti:sapphire laser," *Optics Letters*, vol. 16, no. 1, pp. 42-44, Jan. 1991.

[17] Y. Chen et al., "Dispersion-managed mode locking," *Journal of the Optical Society of America B*, vol. 16, no. 11, pp. 1999-2004, 1999.

[18] T. Kobayashi, J. Zhang, and Z. Wang, "Non-Condon vibronic coupling of coherent molecular vibration in MEH-PPV induced by a visible few-cycle pulse laser," *New Journal of Physics*, vol. 11, p. 013048, Jan. 2009.

[19] J. Du, K. Nakata, Y. Jiang, E. Tokunaga, and T. Kobayashi, "Spectral modulation observed in Chl-a by ultrafast laser spectroscopy," *Optics Express*, vol. 19, no. 23, pp. 22480-22485, Nov. 2011.

[20] J. Du, T. Teramoto, K. Nakata, E. Tokunaga, and T. Kobayashi, "Real-Time Vibrational Dynamics in Chlorophyll a Studied with a Few-Cycle Pulse Laser," *Biophysical Journal*, vol. 101, no. 4, pp. 995-1003, Aug. 2011.

[21] J. Livet et al., "Transgenic strategies for combinatorial expression of fluorescent proteins in the nervous system," *Nature*, vol. 450, no. 7166, pp. 56-62, Nov. 2007.

[22] T. Udem, R. Holzwarth, and T. W. Hansch, "Optical frequency metrology," *Nature*, vol. 416, no. 6877, pp. 233-237, Mar. 2002.

[23] Z. Jiang, D. E. Leaird, and A. M. Weiner, "Line-by-line pulse shaping control for optical arbitrary waveform generation," *Optics Express*, vol. 13, no. 25, pp. 10431-10439, 2005.

[24] C.-H. Li et al., "A laser frequency comb that enables radial velocity measurements with a precision of 1[thinsp]cm[thinsp]s-1," *Nature*, vol. 452, no. 7187, pp. 610-612, 2008.

[25] V. P. Kalosha, M. Müller, J. Herrmann, and S. Gatz, "Spatiotemporal model of femtosecond pulse generation in Kerr-lens mode-locked solid-state lasers," *Journal of the Optical Society of America B*, vol. 15, no. 2, pp. 535-550, 1998.

[26] S. T. Cundiff, W. H. Knox, E. P. Ippen, and H. A. Haus, "Frequency-dependent mode size in broadband Kerr-lens mode locking," *Optics Letters*, vol. 21, no. 9, pp. 662-664, May 1996.

[27] M. Abramowitz and I. A. Stegun, *Handbook of Mathematical Functions: with Formulas, Graphs, and Mathematical Tables*. Dover Publications, 1965.

[28] D. Hanna, "Astigmatic Gaussian beams produced by axially asymmetric laser cavities," *IEEE Journal of Quantum Electronics*, vol. 5, no. 10, pp. 483- 488, Oct. 1969.

[29] H. Kogelnik, E. Ippen, A. Dienes, and C. Shank, "Astigmatically compensated cavities for CW dye lasers," *IEEE Journal of Quantum Electronics*, vol. 8, no. 3, pp. 373- 379, Mar. 1972.

[30] A. Penzkofer, M. Wittmann, M. Lorenz, E. Siegert, and S. Macnamara, "Kerr lens effects in a folded-cavity four-mirror linear resonator," *Optical and Quantum Electronics*, vol. 28, no. 4, pp. 423-442, 1996.

[31] V. Magni, G. Cerullo, S. D. Silvestri, and A. Monguzzi, "Astigmatism in Gaussian-beam self-focusing and in resonators for Kerr-lens mode locking," *Journal of the Optical Society of America B*, vol. 12, no. 3, pp. 476-485, 1995.

[32] M. A. Bandres and J. Gutiérrez-Vega, "Ince Gaussian beams," *Optics Letters*, vol. 29, no. 2, pp. 144-146, Jan. 2004.

[33] F. X. Kärtner et al., "Ultrabroadband double-chirped mirror pairs for generation of octave spectra," *Journal of the Optical Society of America B*, vol. 18, no. 6, pp. 882-885, 2001.

[34] F. X. Kärtner et al., "Design and fabrication of double-chirped mirrors," *Optics Letters*, vol. 22, no. 11, pp. 831-833, 1997.

[35] N. Matuschek, F. X. Kärtner, and U. Keller, "Theory of double-chirped mirrors," *IEEE Journal of selected topics in quantum electronics*, vol. 4, no. 2, pp. 197–208, 1998.

[36] H. M. Crespo, J. R. Birge, M. Y. Sander, E. L. Falcão-Filho, A. Benedick, and F. X. Kärtner, "Phase stabilization of sub-two-cycle pulses from prismless octave-spanning Ti:sapphire lasers," *Journal of the Optical Society of America B*, vol. 25, no. 7, p. B147-B154, 2008.

[37] H. M. Crespo, J. R. Birge, E. L. Falcão-Filho, M. Y. Sander, A. Benedick, and F. X. Kärtner, "Nonintrusive phase stabilization of sub-two-cycle pulses from a prismless octave-spanning Ti:sapphire laser," *Optics Letters*, vol. 33, no. 8, pp. 833-835, 2008.

[38] A. Bartels, T. Dekorsy, and H. Kurz, "Femtosecond Ti:sapphire ring laser with a 2-GHz repetition rate and its application in time-resolved spectroscopy," *Optics Letters*, vol. 24, no. 14, pp. 996-998, 1999.

[39] A. Bartels and H. Kurz, "Generation of a broadband continuum by a Ti:sapphire femtosecond oscillator with a 1-GHz repetition rate," *Optics Letters*, vol. 27, no. 20, pp. 1839-1841, 2002.

[40] T. M. Fortier, A. Bartels, and S. A. Diddams, "Octave-spanning Ti:sapphire laser with a repetition rate >1 GHz for optical frequency measurements and comparisons," *Optics Letters*, vol. 31, no. 7, pp. 1011-1013, 2006.

[41] A. Bartels, R. Gebs, M. S. Kirchner, and S. A. Diddams, "Spectrally resolved optical frequency comb from a self-referenced 5 GHz femtosecond laser," *Optics Letters*, vol. 32, no. 17, pp. 2553-2555, 2007.

[42] A. Benedick, D. Tyurikov, M. Gubin, R. Shewmon, I. Chuang, and F. X. Kärtner, "Compact, Ti:sapphire-based, methane-stabilized optical molecular frequency comb and clock," *Optics Letters*, vol. 34, no. 14, pp. 2168-2170, Jul. 2009.

[43] G. T. Nogueira, B. Xu, Y. Coello, M. Dantus, and F. C. Cruz, "Broadband 2.12 GHz Ti:sapphire laser compressed to 5.9 femtoseconds using MIIPS," *Optics Express*, vol. 16, no. 14, pp. 10033-10038, 2008.

[44] A. Bartels, D. Heinecke, and S. A. Diddams, "Passively mode-locked 10 GHz femtosecond Ti:sapphire laser," *Optics Letters*, vol. 33, no. 16, pp. 1905-1907, 2008.

[45] M. Y. Sander, J. Birge, A. Benedick, H. M. Crespo, and F. X. Kärtner, "Dynamics of dispersion managed octave-spanning titanium:sapphire lasers," *Journal of the Optical Society of America B*, vol. 26, no. 4, pp. 743-749, Apr. 2009.

[46] D. Z. Anderson, "Alignment of resonant optical cavities," *Applied Optics*, vol. 23, no. 17, pp. 2944-2949, 1984.

[47] Li-Jin Chen, A. J. Benedick, J. R. Birge, M. Y. Sander, and F. X. Kärtner, "2GHz octave-spanning Ti:sapphire Laser with non-intrusive carrier-envelope phase stabilization," in *IEEE Lasers and Electro-Optics Society, 2008. LEOS 2008. 21st Annual Meeting of the*, 2008, pp. 624-625.

[48] M. Y. Sander, H. M. Crespo, J. R. Birge, and F. X. Kärtner, "Modeling of Octave-Spanning Sub-Two-Cycle Titanium:Sapphire Lasers: Simulation and Experiment," in *Ultrafast Phenomena XVI*, vol. 92, P. Corkum, S. Silvestri, K. A. Nelson, E. Riedle, and R. W. Schoenlein, Eds. Berlin, Heidelberg: Springer Berlin Heidelberg, 2009, pp. 774-776.

[49] O. Mücke et al., "Self-Referenced 200 MHz Octave-Spanning Ti:Sapphire Laser with 50 Attosecond Carrier-Envelope Phase Jitter," *Optics Express*, vol. 13, no. 13, pp. 5163-5169, 2005.

[50] L. Matos, O. D. Mücke, J. Chen, and F. X. Kärtner, "Carrier-envelope phase dynamics and noise analysis in octave-spanning Ti:sapphire lasers," *Optics Express*, vol. 14, no. 6, pp. 2497-2511, 2006.

[51] T. Fuji et al., "Monolithic carrier-envelope phase-stabilization scheme," *Optics Letters*, vol. 30, no. 3, pp. 332-334, Feb. 2005.

[52] J. Herrmann, "Theory of Kerr-lens mode locking: role of self-focusing and radially varying gain," *Journal of the Optical Society of America B*, vol. 11, no. 3, pp. 498-512, 1994.

[53] I. P. Christov, H. C. Kapteyn, M. M. Murnane, C.-P. Huang, and J. Zhou, "Space-time focusing of femtosecond pulses in a Ti:sapphire laser," *Optics Letters*, vol. 20, no. 3, pp. 309-311, Feb. 1995.

[54] I. P. Christov, V. D. Stoev, M. M. Murnane, and H. C. Kapteyn, "Mode locking with a compensated space-time astigmatism," *Optics Letters*, vol. 20, no. 20, pp. 2111-2113, Oct. 1995.

[55] I. P. Christov, V. D. Stoev, M. M. Murnane, and H. C. Kapteyn, "Sub-10-fs operation of Kerr-lens mode-locked lasers," *Optics Letters*, vol. 21, no. 18, pp. 1493-1495, 1996.

[56] I. P. Christov and V. D. Stoev, "Kerr-lens mode-locked laser model: role of space time effects," *Journal of the Optical Society of America B*, vol. 15, no. 7, pp. 1960-1966, 1998.

[57] I. P. Christov, V. D. Stoev, M. M. Murnane, and H. C. Kapteyn, "Absorber-assisted Kerr-lens mode locking," *Journal of the Optical Society of America B*, vol. 15, no. 10, pp. 2631-2633, Oct. 1998.

[58] T. Brabec and F. Krausz, "Nonlinear Optical Pulse Propagation in the Single-Cycle Regime," *Physical Review Letters*, vol. 78, no. 17, pp. 3282-3285, Apr. 1997.

[59] J. Philip, C. D'Amico, G. Chériaux, A. Couairon, B. Prade, and A. Mysyrowicz, "Amplification of Femtosecond Laser Filaments in Ti:Sapphire," *Physical Review Letters*, vol. 95, no. 16, p. 163901, Oct. 2005.

[60] S. Tzortzakis et al., "Self-Guided Propagation of Ultrashort IR Laser Pulses in Fused Silica," *Physical Review Letters*, vol. 87, no. 21, p. 213902, Nov. 2001.

[61] A. Couairon and A. Mysyrowicz, "Self-focusing and Filamentation of Femtosecond Pulses in Air and Condensed Matter: Simulations and Experiments," in *Self-focusing: Past and Present*, 2009, pp. 297-322.

[62] Z. Zhang, L. Chen, and X. Bao, "A fourth-order Runge-Kutta in the interaction picture method for numerically solving the coupled nonlinear Schrodinger equation," *Optics Express*, vol. 18, no. 8, pp. 8261-8276, Apr. 2010.

[63] J. Hult, "A Fourth-Order Runge?Kutta in the Interaction Picture Method for Simulating Supercontinuum Generation in Optical Fibers," *Journal of Lightwave Technology*, vol. 25, no. 12, pp. 3770-3775, Dec. 2007.

[64] M. Guizar-Sicairos and J. C. Gutiérrez-Vega, "Computation of quasi-discrete Hankel transforms of integer order for propagating optical wave fields," *Journal of the Optical Society of America A*, vol. 21, no. 1, pp. 53-58, Jan. 2004.

[65] G. Agrawal, "Nonlinear fiber optics," *Nonlinear Science at the Dawn of the 21st Century*, pp. 195–211, 2000.

[66] K. J. Blow and D. Wood, "Theoretical description of transient stimulated Raman scattering inoptical fibers," *IEEE Journal of Quantum Electronics*, vol. 25, no. 12, pp. 2665-2673, Dec. 1989.

[67] A. Heidt, "Efficient Adaptive Step Size Method for the Simulation of Supercontinuum Generation in Optical Fibers," *Journal of Lightwave Technology*, vol. 27, no. 18, pp. 3984-3991, 2009.

[68] L.-J. Chen, A. J. Benedick, J. R. Birge, M. Y. Sander, and F. Kärtner, "Octave-spanning, dual-output 2.166 GHz Ti:sapphire laser," *Optics Express*, vol. 16, no. 25, pp. 20699-20705, 2008.

[69] U. Keller et al., "Semiconductor saturable absorber mirrors (SESAM's) for femtosecond to nanosecond pulse generation in solid-state lasers," *Selected Topics in Quantum Electronics, IEEE Journal of*, vol. 2, no. 3, pp. 453, 435, 1996.

[70] R. Ell et al., "Generation of 5-fs pulses and octave-spanning spectra directly from a Ti:sapphire laser," *Optics Letters*, vol. 26, no. 6, pp. 373-375, 2001.

[71] L. Matos et al., "Direct frequency comb generation from an octave-spanning, prismlessTi:sapphire laser," *Optics Letters*, vol. 29, no. 14, pp. 1683-1685, 2004.

[72] S. Chen and J. Wang, "Self-starting issues of passive self-focusing mode locking," *Optics Letters*, vol. 16, no. 21, pp. 1689-1691, Nov. 1991.

[73] G. Cerullo, S. D. Silvestri, and V. Magni, "Self-starting Kerr-lens mode locking of a Ti:sapphire laser," *Optics Letters*, vol. 19, no. 14, pp. 1040-1042, Jul. 1994.

[74] G. Cerullo, S. De Silvestri, V. Magni, and L. Pallaro, "Resonators for Kerr-lens mode-locked femtosecond Ti:sapphire lasers," *Optics Letters*, vol. 19, no. 11, pp. 807-809, 1994.

[75] E. J. Grace, A. Ritsataki, P. M. W. French, and G. H. C. New, "New optimization criteria for slit-apertured and gain-apertured KLM all-solid-state lasers," *Optics Communications*, vol. 183, no. 1-4, pp. 249-264, 2000.

[76] C. P. J. Barty et al., "Regenerative pulse shaping and amplification of ultrabroadband optical pulses," *Optics Letters*, vol. 21, no. 3, pp. 219-221, 1996.

[77] P. F. Moulton, "Spectroscopic and laser characteristics of Ti:Al2O3," *Journal of the Optical Society of America B*, vol. 3, no. 1, pp. 125-133, Jan. 1986.

[78] J. R. Birge and F. X. Kärtner, "Efficient optimization of multilayer coatings for ultrafast optics using analytic gradients of dispersion," *Applied Optics*, vol. 46, no. 14, pp. 2656-2662, May 2007.

[79] P. K. A. Wai, C. R. Menyuk, Y. C. Lee, and H. H. Chen, "Nonlinear pulse propagation in the neighborhood of the zero-dispersion wavelength of monomode optical fibers," *Optics Letters*, vol. 11, no. 7, pp. 464-466, Jul. 1986.

[80] N. Akhmediev and M. Karlsson, "Cherenkov radiation emitted by solitons in optical fibers," *Physical Review A*, vol. 51, no. 3, p. 2602, Mar. 1995.

[81] P. K. A. Wai, H. H. Chen, and Y. C. Lee, "Radiations by "'solitons"' at the zero group-dispersion wavelength of single-mode optical fibers," *Physical Review A*, vol. 41, no. 1, p. 426, Jan. 1990.

[82] V. I. Karpman, "Radiation by solitons due to higher-order dispersion," *Physical Review E*, vol. 47, no. 3, p. 2073, Mar. 1993.

[83] J. N. Elgin, T. Brabec, and S. M. J. Kelly, "A perturbative theory of soliton propagation in the presence of third order dispersion," *Optics Communications*, vol. 114, no. 3-4, pp. 321-328, Feb. 1995.

[84] L. Tartara, I. Cristiani, and V. Degiorgio, "Blue light and infrared continuum generation by soliton fission in a microstructured fiber," *Applied Physics B: Lasers and Optics*, vol. 77, pp. 307-311, Sep. 2003.

[85] G. Genty, M. Lehtonen, and H. Ludvigsen, "Effect of cross-phase modulation on supercontinuum generated in microstructured fibers with sub-30 fs pulses," *Optics Express*, vol. 12, no. 19, pp. 4614-4624, 2004.

[86] A. V. Mitrofanov et al., "Highly birefringent silicate glass photonic-crystal fiber with polarization-controlled frequency-shifted output: A promising fiber light source fornonlinear Raman microspectroscopy," *Optics Express*, vol. 14, no. 22, pp. 10645-10651, Oct. 2006.

[87] H. Tu and S. A. Boppart, "Optical frequency up-conversion by supercontinuum-free widely-tunable fiber-optic Cherenkov radiation," *Optics Express*, vol. 17, no. 12, pp. 9858-9872, 2009.

[88] S. Hill, C. E. Kuklewicz, U. Leonhardt, and F. König, "Evolution of light trapped by a soliton in a microstructured fiber," *Optics Express*, vol. 17, no. 16, pp. 13588-13600, 2009.

[89] K. Saitoh, M. Koshiba, T. Hasegawa, and E. Sasaoka, "Chromatic dispersion control in photonic crystal fibers: application to ultra-flattened dispersion," *Optics Express*, vol. 11, no. 8, pp. 843-852, Apr. 2003.

[90] D. V. Skryabin, F. Luan, J. C. Knight, and P. S. J. Russell, "Soliton Self-Frequency Shift Cancellation in Photonic Crystal Fibers," *Science*, vol. 301, no. 5640, pp. 1705-1708, 2003.

[91] S. P. Stark, F. Biancalana, A. Podlipensky, and P. St. J.Russell, "Nonlinear wavelength conversion in photonic crystal fibers with three zero-dispersion points," *Physical Review A*, vol. 83, no. 2, p. 023808, Feb. 2011.

[92] D. V. Skryabin and A. V. Yulin, "Theory of generation of new frequencies by mixing of solitons and dispersive waves in optical fibers," *Physical Review E*, vol. 72, no. 1, p. 016619, Jul. 2005.

[93] A. V. Husakou and J. Herrmann, "Supercontinuum generation, four-wave mixing, and fission of higher-order solitons in photonic-crystal fibers," *Journal of the Optical Society of America B*, vol. 19, no. 9, pp. 2171-2182, 2002.

[94] GorbachA. V. and SkryabinD. V., "Light trapping in gravity-like potentials and expansion of supercontinuum spectra in photonic-crystal fibres," *Nat Photon*, vol. 1, no. 11, pp. 653-657, Nov. 2007.

[95] D. R. Austin, C. M. de Sterke, B. J. Eggleton, and T. G. Brown, "Dispersive wave blue-shift in supercontinuum generation," *Optics Express*, vol. 14, no. 25, pp. 11997-12007, Dec. 2006.

[96] S. P. Stark, A. Podlipensky, N. Y. Joly, and P. S. J. Russell, "Ultraviolet-enhanced supercontinuum generation in tapered photonic crystal fiber," *Journal of the Optical Society of America B*, vol. 27, no. 3, pp. 592-598, Mar. 2010.

[97] J. M. Dudley, G. Genty, and S. Coen, "Supercontinuum generation in photonic crystal fiber," *Reviews of Modern Physics*, vol. 78, no. 4, p. 1135, Oct. 2006.

[98] S. Roy, S. K. Bhadra, and G. P. Agrawal, "Effects of higher-order dispersion on resonant dispersive waves emitted by solitons," *Optics Letters*, vol. 34, no. 13, pp. 2072-2074, Jul. 2009.

[99] A. A. Amorim, "Study of non-solitonic blue-green radiation generated in mm-long photonic crystal fibers," 2006, vol. 6187, pp. 618717-618717-9.

[100] H. Tu and S. A. Boppart, "Ultraviolet-visible non-supercontinuum ultrafast source enabled by switching single silicon strand-like photonic crystal fibers," *Optics Express*, vol. 17, no. 20, pp. 17983-17988, 2009.

[101] G. Chang, L.-J. Chen, and F. X. Kärtner, "Highly efficient Cherenkov radiation in photonic crystal fibers for broadband visible wavelength generation," *Optics Letters*, vol. 35, no. 14, pp. 2361-2363, Jul. 2010.

[102] F. X. Kärtner, *Few-cycle laser pulse generation and its applications*. Springer, 2004.

[103] G. Krauss et al., "Synthesis of a single cycle of light with compact erbium-doped fibre technology," *Nat Photon*, vol. 4, no. 1, pp. 33-36, Jan. 2010.

[104] G. P. Agrawal, *Nonlinear fiber optics*. Academic Press, 2001.

[105] Q. Lin and G. P. Agrawal, "Raman response function for silica fibers," *Optics Letters*, vol. 31, no. 21, pp. 3086-3088, Nov. 2006.

[106] A. Nahata, A. S. Weling, and T. F. Heinz, "A wideband coherent terahertz spectroscopy system using optical rectification and electro-optic sampling," *Applied Physics Letters*, vol. 69, p. 2321, 1996.

[107] Y. Kodama and A. Hasegawa, "Nonlinear pulse propagation in a monomode dielectric guide," *IEEE Journal of Quantum Electronics*, vol. 23, no. 5, pp. 510- 524, May 1987.

[108] M. T. Murphy et al., "High-precision wavelength calibration of astronomical spectrographs with laser frequency combs," *arXiv:astro-ph/0703622*, Mar. 2007.

[109] T. Steinmetz et al., "Laser Frequency Combs for Astronomical Observations," *Science*, vol. 321, no. 5894, pp. 1335 -1337, 2008.

[110] D. A. Braje, M. S. Kirchner, S. Osterman, T. Fortier, and S. A. Diddams, "Astronomical spectrograph calibration with broad-spectrum frequency combs," *The European Physical Journal D*, vol. 48, pp. 57-66, May 2008.

[111] G. Chang, C.-H. Li, D. F. Phillips, R. L. Walsworth, and F. X. Kärtner, "Toward a broadband astro-comb: effects of nonlinear spectral broadening in optical fibers," *Optics Express*, vol. 18, no. 12, pp. 12736-12747, Jun. 2010.

[112] C.-H. Li et al., "In-situ determination of astro-comb calibrator lines to better than 10 cm s-1," *Optics Express*, vol. 18, no. 12, pp. 13239-13249, Jun. 2010.

[113] F. Quinlan, G. Ycas, S. Osterman, and S. A. Diddams, "A 12.5 GHz-spaced optical frequency comb spanning >400 nm for near-infrared astronomical spectrograph calibration," *Review of Scientific Instruments*, vol. 81, p. 063105, 2010.

[114] A. J. Benedick et al., "Visible wavelength astro-comb," *Optics Express*, vol. 18, no. 18, pp. 19175-19184, 2010.

[115] F. Bouchy, F. Pepe, and D. Queloz, "Fundamental photon noise limit to radial velocity measurements," *Astronomy and Astrophysics*, vol. 374, pp. 733-739, Aug. 2001.

[116] C. H. Li, G. Chang, L. J. Chen, D. F. Phillips, F. Kärtner, and R. L. Walsworth, "Laboratory Demonstration and Characterization of a Green Astro-comb," in *Advanced Solid-State Photonics*, 2011.

[117] V. Pervak, A. V. Tikhonravov, M. K. Trubetskov, S. Naumov, F. Krausz, and A. Apolonski, "1.5-octave chirped mirror for pulse compression down to sub-3 fs," *Applied Physics B: Lasers and Optics*, vol. 87, no. 1, pp. 5-12, 2007.

[118] A. Bartels, D. Heinecke, and S. A. Diddams, "10-GHz Self-Referenced Optical Frequency Comb," *Science*, vol. 326, no. 5953, p. 681, 2009.

[119] C. Gohle et al., "A frequency comb in the extreme ultraviolet," *Nature*, vol. 436, no. 7048, pp. 234-237, Jul. 2005.

[120] M. J. Thorpe, K. D. Moll, R. J. Jones, B. Safdi, and J. Ye, "Broadband Cavity Ringdown Spectroscopy for Sensitive and Rapid Molecular Detection," *Science*, vol. 311, no. 5767, pp. 1595-1599, Mar. 2006.

[121] G. Chang, L.-J. Chen, and F. X. Kärtner, "Fiber-optic Cherenkov radiation in the few-cycle regime," *Optics Express*, vol. 19, no. 7, pp. 6635-6647, Mar. 2011.

[122] A.-C. Tien, S. Backus, H. Kapteyn, M. Murnane, and G. Mourou, "Short-Pulse Laser Damage in Transparent Materials as a Function of Pulse Duration," *Physical Review Letters*, vol. 82, no. 19, p. 3883, May 1999.

[123] F. Gori, G. Guattari, and C. Padovani, "Bessel-Gauss beams," *Optics Communications*, vol. 64, no. 6, pp. 491-495, Dec. 1987.

[124] W. P. Putnam, G. Abram, E. L. Falcão-Filho, J. R. Birge, and F. X. Kärtner, "High-intensity Bessel-Gauss beam enhancement cavities," in *Conference on Lasers and Electro-Optics*, 2010.